Biophysical determinants for Adenovirus uncoating & infectivity

A Thesis submitted in partial fulfillment of the requirements for the degree of Doctor of Philosophy

Alvaro Ortega-Esteban

FACULTAD DE CIENCIAS
UNIVERSIDAD AUTÓNOMA DE MADRID

Departamento de Física de la Materia Condensada
Universidad Autónoma de Madrid, Madrid, Spain

Thesis supervisors:
Pedro José de Pablo Gómez
Carmen San Martín Pastrana

December 2015

Publications

1. **A. Ortega-Esteban**, I. Horcas, M. Hernando-Pérez, P. Ares, A. J. Pérez-Berná, C. San Martín, J. L. Carrascosa, P. J. de Pablo, J. Gómez-Herrero. "Minimizing tip-sample forces in jumping mode atomic force microscopy in liquid.", *Ultramicroscopy*, **114**, pp. 56-61, (2012).

2. A. J. Pérez-Berná, **A. Ortega-Esteban**, R. Menéndez-Conejero, D. C. Winkler, M. Menéndez, A. C. Steven, S. J. Flint, P. J. de Pablo, C. San Martín. "The role of capsid maturation on adenovirus priming for sequential uncoating.", *Journal of Biological Chemistry*, **287**- 37, pp. 31582-31595, (2012).

3. **A. Ortega-Esteban**, A. J. Pérez-Berná, R. Menéndez-Conejero, S. J. Flint, C. San Martín, P. J. de Pablo. "Monitoring dynamics of human adenovirus disassembly induced by mechanical fatigue.", *Scientific Reports*, **3**, 1434, (2013).

4. R. Menéndez-Conejero, A. J. Pérez-Berná, G. Condezo, **A. Ortega-Esteban**, M. Alamo, P. J. Pablo, C. San Martín. "Biophysical methods to monitor structural aspects of the adenovirus infectious cycle.", *Methods in Molecular Biology*, **1089**,pp. 1 - 24, (2014).

5. **A. Ortega-Esteban***, K. Bodensiek*, C. San Martín, M. Suomalainen, U. F. Greber, P. J. de Pablo, I. A T. Schaap. "Fluorescence tracking of genome release during the mechanical unpacking of single viruses.", *ACS Nano*, DOI: 10.1021/acsnano.5b03020, (2015). *Authors contributed equally

6. **A. Ortega-Esteban**, C. Condezo, A. J. Pérez-Berná, M. Chillón, S. J. Flint, D. Reguera, C. San Martín, P. J. de Pablo. "Mechanics of viral chromatin reveals the pressurization of human adenovirus.", *ACS Nano*, accepted, (2015).

A mi familia,
mi piedra angular.

Agradecimientos

Dicen que la personalidad de uno se va adaptando a las necesidades, situaciones y personas de las que nos rodeamos. Por lo que va cambiando con el paso del tiempo, y me digo yo que esto debe influir de una forma u otra en nuestro trabajo. Por lo tanto, el trabajo realizado a lo largo de todos estos años corresponde a la unión de todas esas personas que de alguna manera, tanto dentro como fuera del laboratorio han influido en mi persona. Me gustaría dedicarles unas palabras de agradecimiento y alabanza. Perdonad mi memoria perecedera pero seguro, segurísimo, que se me escurre alguien entre las líneas y no lo cite en ellas, pero no quiere decir que no le tenga agradecido su presencia.

Quiero comenzar agradeciendo a las dos personas que han hecho posible este proyecto y que me han ayudado mucho: Pedro y Carmen. Pedro, te agradezco tu infinita paciencia desde el principio de esta andadura. Tu perseverante pasión, el carbón que ha combustionado y ha echado a andar esta máquina, es una fuente inagotable de energía que ha dado el movimiento a ideas en mi cabeza. Me has introducido y he absorbido de ti conocimiento y criterio para interpretar la mecánica de los virus. Carmen, te tengo muy agradecido que me hayas anclado al adenovirus en todo este periodo. Ha sido apasionante ir descubriendo la complejidad que encierra algo tan pequeño y aparentemente sencillo. Has estado en primera fila en todo momento y accesible para discusiones y aprendizaje. A los dos, os agradezco de corazón que hayáis confiado en mí a pesar de mi propio, intrínseco y antagónico escepticismo. Mil gracias por haberme brindado la oportunidad de trabajar junto a vosotros y haberme instruido para ser un científico. Seguido, Julio, has estado siempre en el fondo, tal apuntador del conocimiento. He aprendido mucho de ti, tu curiosidad y cercanía. Constantemente accesible para hablar y echar una mano a esta disipada cabeza que tengo encima de los hombros. Has significado mucho para mí.

Mercedes, me convertí en tu sombra adaptándome a los movimientos de tus manos de los que he aprendido el delicado manejo de la fina punta del AFM sobre los virus. En estos años he descubierto, vivido y compartido mucho junto a ti, siendo la semilla de mi pasión por el surf. Todo lo guardo con mucho cariño en mi corazón. Aida, has traído e impregnado el laboratorio de tu sensatez dejando parte de ese poso en mí. Los razonamientos

y discusiones contigo han sido catalizador de mi madurez como científico. Ambas habéis sido la esencia de mi tesis. Gracias.

Marina y Natalia, con vuestra ingenua y pacífica alma, habéis cerrado el broche de mi paso por este laboratorio con alegría. Junto con Manuel, os deseo mucha suerte a todos en vuestros caminos, y a los que os quedáis por aquí, estáis en muy buenas manos.

En mi grupo paralelo, Gabriela, tu dulce personalidad se ha hecho notar en todo lo que has tocado, siempre trabajadora y eficaz, has sido uno de los pilares del proyecto que hemos presentado. Rosa, lo dice todo tu nombre, una persona muy hermosa y con mucha valía, un ejemplo a seguir para mí. Me has inspirado mucho. Ana, el otro pilar, has guiado mis primeros pasos por los tortuosos recovecos de la estructura del adenovirus. María, Marta, Mariam y Diego, ha sido un placer cruzarme con vosotros por el camino.

De vuelta a la gran familia de microscopistas de proximidad, comenzando con las fuerzas, Cristina, mis ojos te han visto siempre como un alma libre y con tesón, loo tu trabajo y me gusta tu forma de ironizar. Guillermo, Irene, Francisco. Chicos, grandes donde los haya. Por otro lado, Pablo, una persona muy sólida que siempre me ha transmitido seguridad. Miriam Moreno, que nos hemos vuelto a encontrar por el camino, me gusta tu orden y proceder. Miriam Jaafar, eres un sol, que me ha echado una cálida mano en ciencia y docencia, y me ha transmitido mucha calma. Y David, siempre muy sabio. Pasando al ultra alto vacío, a fuerza, vienen: Chema, Nicoleta y Bruno. Bruno, gran compañía en la agridulce escritura, a quien deseo mucha suerte junto con Cecilia. A través del túnel, veo a Iván (directo y seguro, gracias por tus útiles consejos y discusiones), Ana (dura como las piedras), Héctor (vacilante), Miguel (a quien veo como un Feynman), Antonio (un buen amigo y maquinador), Alba y Antonela que habéis amenizado la tesis.

Elsa, Luisa, Santiago, José María y José Luis, engranaje y piezas clave para el funcionamiento del departamento de física de la materia condensada, que me han sacado más de una vez de un apuro. A Macarena, siempre tan agradable manteniendo todo el departamento ordenado. Aunque no sé dar nombres, a los miembros de Segainvex que nos han sacado a mis compañeras y a mí de algún apuro poniendo ojos a nuestros AFMs a contracorriente. Agradezco a la brigada que me activan con sus cafés cada mañana.

En mi experiencia docente, he tenido el placer de encontrarme con gente comprometida con sus alumnos: José Emilio, Félix, Juan José, Miriam Jaafar, Miguel Ángel y Manuel. Habéis enseñado tanto a vuestros alumnos, como a mí para ser profesor.

Quiero mencionar a los vecinos de enfrente, compañeros acuáticos, Isidoro, Antonio y Juan Pedro, a quien además le agradezco mucho haberme iniciado en LaTeX y prestado la plantilla de tesis, y haberme aguantado junto con Jonathan mi intrusión en un hueco del despacho. Isadora (mon amour), Cristina (compañera de master y tesis), Lorena, Gonzalo, Virginia, Rodrigo, han dado ese toque de alquimia a los primeros años con quienes he disfrutado mucho. A los antiguos miembros de Nanotec que han sido básicos en estos años y han contribuido a que todo funcionase: Adriana (portadora de paz), Nacho y Alejandro (ambos pacientes como nadie), Jaime, Luis, Edu, Rafa, y de nuevo Pablo y Miriam.

Por otro lado, quiero agradecer también a Mauricio, un gran científico y a quien admiro mucho, a la gente de su grupo, en especial a Mila, Rebeca, Pablo, Alejandro. Por otro lado a Carolina, antigua estudiante de Pedro, a sus excompañeros de grupo Maru y Benjamin. Fernando ha sabido reunir a muy buena gente. Agradezco el trabajo de científicos que admiro en Barcelona, David Reguera y las grandes personas que han estado bajo su mando en este periodo: Toni y María. Admirables los tres.

I am glad that I could work in the group of Iwan Schaap, respectful and very nice person. Kai, whom I shared hours of shade and light in the lab. Mitja, Kalina, Miquel, Paula that make the life easier in Göttingen. Trudi and Matteo, my home, sweet home. I want to thank also to Urs Greber and his team for the "bright" viruses they provided to perform the experiments in Germany.

En el ámbito personal, cabe mencionar a muchas personas que me han liberado consciente o inconscientemente a mi mente y la han dejado volar salvajemente. Salpicado por las aguas autónomas, he conocido a gente muy interesante, comenzando con Uamterpolo y todos los waterpolistas: Manu, Intz, Adriana, Maria, Juan Carlos, José Ángel, Javi, Victor... y con algunos de ellos he disfrutado nuestro paso por el Master-Brains. Gente que te cruzas por las calles como Miguel Manso, Curro, Hugo (también en la cresta de las olas) que ayudan a que los metros acuáticos parezcan menos densos.

Mis malasañeros que llevo en mi corazón de cartón que os encontrasteis gris y lo habéis llenado de color: Oscar, Vicen, Alvar, Marta, Cris, Fati, Javi, Rubén. Recuerdo todo lo que hemos vivido juntos y lo que se nos habrá quedado en el tintero. Thanks Chad, a huge and hopeful dalmatian heart that marked my life. Y con derivas y corrientes he acabado compartiendo noches de apoyo doctoral con Pedro Luis y cia, con su exquisito castellano, a quien deseo lo mejor. Austin, a good friend. El peculiar Joanin y sus interesantes conversaciones. Hijo de Lut, a buenas horas. Nada más que decir: "y aquí tú y yo, solo quedamos los buenos, nadie nos enseña donde parar". No os olvido.

Caballeros galopantes de ondas de gran amplitud en el agua, surfistas que han dejado una gran estela en mi vida con los que he ido aprendiendo y creciendo: Monti, Jorge, Javitron, Josema, Costa, André, Luiyi, Alex, Cherro, More y un largo etcétera de gente. Con quienes he compartido además tardes liberando tensiones en Crissfit con Cris y toda la gente a su alrededor. Todos me habéis ayudado mucho y lo tengo muy agradecido.

Agradezco conservar a mi enfermera del corazón, María, y mi confianza personificada, Laura Elena. Venís más allá del inicio de esta etapa, y vamos a continuar más allá. Y también a mis amigos de toda la vida: Rubi, Jorge, Javi, Bea... y muchos más. Me siento agradecido al vacío piso de Fernández de los Ríos y sus no habitantes: Mery, Rafa, Alvarodo, Aitor y Luis. Además en el ecuador, viendo kiwis con Laura, David y Jaime, me dio fuerza antípoda para continuar. Gracias.

Gracias a Oscar López por buscar dentro e intentar ordenar mis prismas que distorsionan mi visión del mundo. Y también a Sara por dar forma a mi cabeza.

Para finalizar, he decidido dejar los agradecimientos a las personas más importantes en mi vida. Mi familia. Mi hermana, Paloma, mi bichito, una gran persona con un gran alma y corazón. Oscar, un buen chico. Mis primos Pablo (rodeado de cucos), Jorge y José Carlos. Mis tíos y tías, la loca Paloma, Pili, Pepino y Pepe. Mis abuelos y abuelas, Pablo y Julia, os echo mucho de menos; Pili y Demetrio, con mucho corazón. Mis padres, Carmen y Juan Carlos, me habéis dado la vida y apoyado en todo momento, y eso no tiene precio. Gracias a todos.

Gracias por todo

Contents

List of Figures

List of Tables

List of Tables

Resumen

La presente tesis se centra en la caracterización de las propiedades mecánicas de adenovirus humano mediante microscopía de fuerzas atómicas en medio líquido. El adenovirus es un virus común formado de una cápside proteica en forma de icosaedro sin envuelta lipídica de unos 95 nm de diámetro, que presenta una leve patología en individuos sanos pero un gran potencial en el campo de la biomedicina, bio y nanotecnología. En particular, se han estudiado los cambios en la morfología, elasticidad, fragilidad y estabilidad mecánica que se producen en las cápsides víricas durante el ciclo viral. Se ha demostrado que el proceso de maduración del virus influye en sus propiedades mecánicas intentando entender los factores físicos que juegan un papel en la infectividad del virus por comparación de la cepa salvaje madura del virus con su inocuo estadio inmaduro.

La memoria se organiza en 6 capítulos. El capítulo 1 introduce brevemente el adenovirus humano haciendo hincapié en su estructura, y en su peculiar minicromosoma, así como al proceso de maduración del virus que da claves para comprender su infectividad. El capítulo termina con una breve motivación de la tesis. En el capítulo 2 se hace una breve descripción de conceptos básicos de la técnica principal usada a lo largo de la tesis, la microscopía de fuerzas atómicas (AFM, siglas en inglés). El capítulo 3 muestra los primeros pasos en la caracterización por AFM de adenovirus mostrando la optimización

de las condiciones de adsorción, escaneo y obtención de propiedades mecánicas. Los resultados muestran que la partícula madura es más rígida que la inmadura. En el capítulo 4 se hace un estudio del comportamiento frente a un estrés mecánico continuo, homólogo a los experimentos de fatiga macroscópicos de ciencia de materiales, de los estadios maduro e inmaduro de adenovirus. Ambas partículas víricas muestran diferente propensión a la pérdida de pentones y diferentes modos de desensamblaje de la cápside proteica exponiendo finalmente su genoma al medio. Además se hace un breve estudio de fatiga mecánica a diferentes fuerzas mostrando un comportamiento similar a las curvas S-N de fatiga descritas en ciencia de materiales. Los resultados previos del aumento de la rigidez de las partículas víricas maduras dieron lugar a una pregunta sobre la posible presurización durante la maduración, que se aborda en el capítulo 5. La recuperación del fenotipo inmaduro por parte del virus maduro en presencia de agentes condensadores de ADN junto con medidas de la rigidez del minicromosoma y modelos teóricos demuestran dicha presurización, y su origen debido a la distensión del cromosoma en la maduración. El capítulo 6 muestra los resultados obtenidos sobre la exposición del minicromosoma al exterior al inducir el desensamblaje de la cápside proteica mediante la combinación de microscopía de fuerzas y fluorescencia. Por último, se exponen las conclusiones generales de la tesis presentada.

Abstract

This thesis focuses on characterizing the mechanical properties of human adenovirus by atomic force microscopy in liquid medium. Adenovirus is a common non-enveloped virus formed by a proteic icosahedral capsid of about 95 nm diameter. It presents a mild pathogeny in healthy individuals but also a great potential in the fields of biomedicine, bio- and nanotechnology. In particular, we have studied the changes in morphology, elasticity, brittleness and mechanical stability that occur in viral capsids during the viral cycle. Here it is shown that the process of maturation of the virus affects its mechanical properties and we tried to understand the physical factors that play a role in virus infectivity by comparing mature wild-type virus with its harmless immature stage.

The manuscript is organized in six chapters. Chapter 1 briefly introduces human adenovirus, emphasizing its structure and its peculiar minichromosome, as well as the maturation of the virus that gives clues to understand its infectivity. In chapter 2, we present a brief description of basic concepts of the main technique used throughout the thesis, atomic force microscopy (AFM). Chapter 3 shows the first steps in the characterization of adenovirus by AFM, optimization of experimental conditions and the first measurements of its mechanical properties. The mature particle is stiffer than the immature one. In chapter 4, we study the behavior of adenovirus mature and imma-

ture particles under continuous mechanical stress experiments, similar to the macroscopic fatigue assays of materials science. Both viral particles exhibit different propensity to lose pentons and disassembly pathways of the capsid, finally exposing their genomes to the medium. Furthermore, a brief study shows that by applying different forces in mechanical fatigue assays, a behavior describable by S-N curves similar to those in materials science is observed. Chapter 5 addresses the question about the possible pressurization during the maturation by an increase in stiffness in the virus particles. The recovery of immature phenotype for the mature virus in presence of DNA-condensing agents together with core stiffness measurements and theoretical models demonstrate such pressurization, that arises from the loosening of the chromosome in the maturation. Chapter 6 describes the results obtained on the exposition of the minichromosome induced by the mechanical disassembly of the protein capsid by combining force and fluorescence microscopy. Finally, the general conclusions of the thesis are presented.

Chapter 1

Introduction

Biophysics is a cross-disciplinary science that uses foundations from Physical Science to understand biological systems. Although this name was first used in 1892 by Karl Pearson in his book *"The Grammar of Science"*,[1] the biophysics can be tracked back to antiquity, when Heraclitus in the fifth century B.C. speculated on mechanistic theories of processes and dynamics of life; or in the Renaissance, when Leonardo da Vinci investigated the biomechanical description of bird flight for engineering his models.[2] But it was not until the 20th century, when biophysics underwent a strong growth accompanied with technological and theory developments. At present, biophysics is a wide range science that encompasses from biomolecular problems at the sub-nanoscale to environmental issues at the mesoscale.

Viruses (from Latin toxin or poison) are bioparticles in the nano to micrometer range[3,4] within the biophysics scope, with a simple structure of proteins and nucleic acids that reproduce at the expense of hijacking metabolic machinery from cells. The Tobacco Mosaic Virus (TMV), first named as *filterable agent of the tobacco mosaic disease*, was the first described pathogen of this type, by Dimitri Ivanovsky at the end of the nineteenth century.[5] From that moment on, and with the development of new techniques such as electron microscopy

(EM) or X-ray crystallography, numerous viruses of different size and morphology have been discovered. It is speculated nowadays that millions of different virus types exist,[6] making them the most abundant entities on the planet and second in biomass after prokaryotes.[7]

Essentially, viruses infect host cells, replicate, package their genome and exit to find new target cells. Viruses have evolved to face and withstand different extreme environments along this cycle, forcing them to have a versatile structure to protect their inner cargo and successfully release it at the appropriate time and place. Their metastable structure and its dynamics make them interesting not only for their role as infectious pathogens but also as molecular containers with potential applications in materials science and medicine.[8] A better comprehension of their physical properties (stiffness, surface charge density), structure (protein units, genome organization) and functionality (assembly, infection pathway) are essential for the development of these new strategies.

The increasing interest in virus applications in biomedicine, bio and nanotechnology, together with the development of physics-based techniques such as cryo-electron microscopy (cryo-EM), X-ray crystallography, optical tweezers and atomic force microscopy (AFM), have given rise to physics-oriented studies known as *Physical Virology*. Physical virology not only encompasses experimental approaches, but also theoretical models to understand the physical basis that govern virus structure and dynamics. This basic science is one of the milestones on the road leading the fight against viral disease and the development of functional viral nanoparticles for their use in nanotechnology and medicine.[9,10]

It is important to bear in mind that viruses are subjected to internal and external forces along their cycle.[11] Forces may act as an environmental selective factor for evolution, selecting the viruses that withstand stress factors encountered along their way to a new target, and are able to release their genetic material in the host cell. This thesis tries to do its bit in physical virology for understanding the influence of the minichromosome organization in the mechanical proper-

ties and disassembly of human adenovirus in physiological conditions that permit its successful functionality.

1.1 Adenovirus

Adenoviruses (AdVs) form the *Adenoviridae* family. They were first isolated in 1953 from adenoid human tissue.[12] They are present in most vertebrates and are classified in different genera:[13]

- *Mastadenovirus* is the largest genus; it contains the human adenoviruses (HAdVs).
- *Atadenovirus* with a broad range of host (ruminant, avian, marsupial and reptilian).
- *Siadenovirus*, isolated from birds and a frog.
- *Aviadenovirus*, infecting birds.
- *Ichtadenovirus*, with only one confirmed member found in fish.

Most common serotypes of human adenovirus produce eye, gut and respiratory infections which are not clinically relevant for healthy individuals but can be severe for immunocompromised patients.[14] Therefore the development of anti-adenoviral drugs is necessary at least for the susceptible human population. On the other hand, adenovirus is a potential candidate vector for gene therapy, although at the moment with very low success.[15]

1.1.1 Adenovirus structure

Viruses present different shapes, there are viruses enveloped by a lipid bilayer as Influenza virus, also containing a conical capsid as the human immunodeficiency virus (HIV), tubular protean structures as the

TMV, prolated head with tail as the bacteriophage ϕ29 or icosahedral shape as adenovirus, among a wide variety of conformation features. Adenovirus main structure is its icosahedral protein shell with fibers projecting from the vertices which encloses a minichromosome that does not follow the icosahedral symmetry.[16] They are non-enveloped (without a lipid bilayer) double-stranded DNA viruses with an icosahedral complex protein capsid of a large size (∼95 nm from vertex to vertex) and triangulation number *pseudo*T=25.[17–19] The most characterize adenovirus are the infectious HAdV type 2 and 5 (HAdV-C2 and HAdV-C5, respectively).[18] These particles have a mass of approximately of $150 \cdot 10^6$ Daltons. The particular viral genome is associated with proteins, all together denominated core.

At the moment, adenovirus is the largest complex resolved at high resolution (∼ 3.5 Å) by two different techniques: cryo-EM and X-ray crystallography.[20,21]

1.1.1.1 Major coat proteins

Adenovirus presents a complex protein composition compared to smaller and simpler viruses such as the Minute Virus of Mice (MVM) or Cowpea Chlorotic Mottle Virus (CCMV). The capsid is made of building blocks termed capsomers. These capsomers, depending on their situation in the capsid, are denominated pentons (at the vertexes) and hexons (for the rest), which are surrounded by 5 or 6 neighboring capsomers, respectively. In the special case of adenovirus, these subunits are not chemically identical, but they are composed by the major coat proteins (figure 1.1 (a)).[19]

Adenovirus proteins are named with roman numbers in order of decreasing molecular weight. The hexon, the main building block of the capsid, is composed by trimers, and not hexamers, of polypeptide II. It is a trimeric capsomer with very clear three towers at the outer part of the capsid, and a pseudo 6-fold hexagonal base.[22] There are 12 hexon trimers at each of the 20 facets of the icosahedral structure, totaling 240 hexon trimers in the capsid (total 720 monomers).

Pentons are situated at the 12 vertices of the icosahedral structure, and are composed by the penton base and the protruding fibers. The penton base is formed of five copies of polypeptide III.[23] Three copies of the fiber protein IV are assembled forming the ∼37 nm long fiber.[24] The trimeric N-terminal tail of the fiber attaches non-covalently to the pentameric penton base. The rest of the architecture of the fiber is a flexible shaft and the C-terminal a globular knob, responsible of target cell recognition.

Upon mild dissociation conditions, stable structures of 9 hexons tiles are generated.[25] They are termed groups of nine (GONs) and are composed of the hexons of the central plate of the facet. The 5 peripentonal hexons (hexons surrounding the penton) together with the penton, form the group of six (GOS).[20,26]

1.1.1.2 Minor coat proteins

The location of minor coat proteins is still a subject of debate. In general, their functionality is as cementing proteins, stabilizing the capsid structure (figure 1.1 (a), right panel). On the outer part of the capsid, polypeptide IX is forming a mesh reinforcing interactions between hexons. They are present within hexons of the GON, thereby stabilizing the observed tile.[19,20]

Polypeptides situated in the inner side of the capsid are IIIa, VI and VIII. There are five monomers of IIIa arranged in a ring underneath each vertex. IIIa is the responsible for gluing the GOS tile, connecting the penton and peripentonal hexons. Polypeptide VIII is the less characterized minor coat protein. It appears interacting with IIIa and the hexon base at the periphery of the GOS, binding the GOS and the surrounding GONs. VIII is also located at the GONs helping their stabilization together with IX. Polypeptide VI is a multifunctional protein that plays an important role in virus entry, transporting hexons for new particles assembly and acting as cofactor of the adenoviral protease for maturation. This protein is located in the inner cavity of hexons and also underneath pentons.[19–21,27]

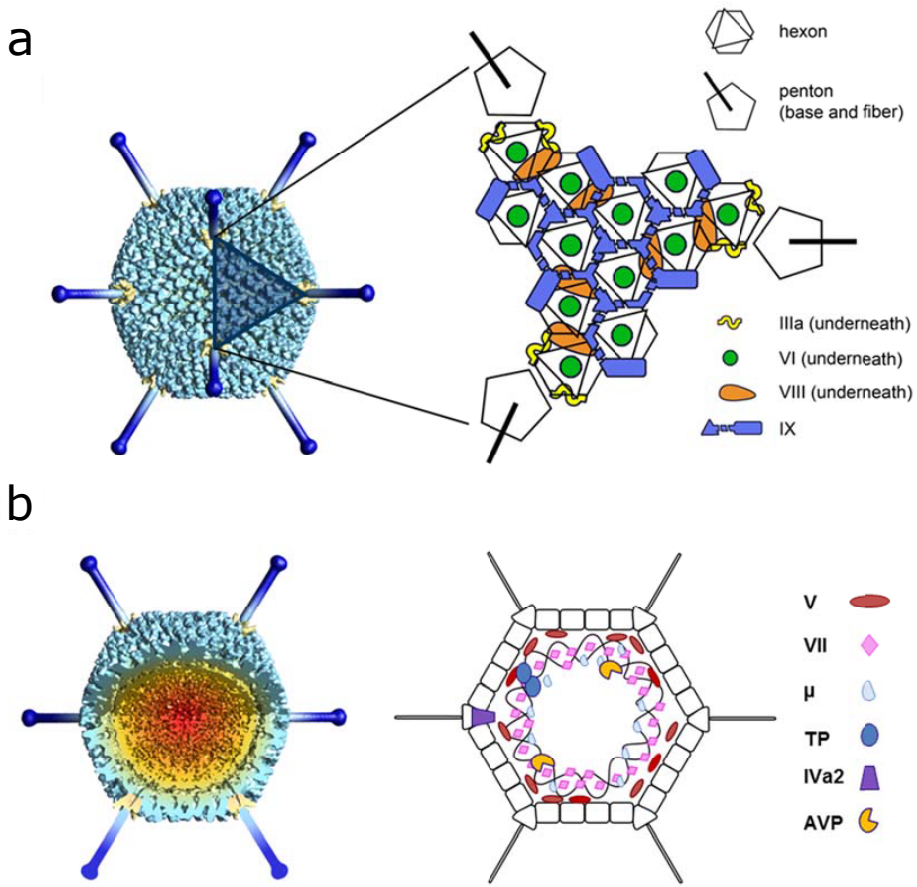

Figure 1.1: Overall adenovirus structure and components. (a) Icosahedral model built form a low resolution cryo-EM map, with penton base and fibers (modeled from crystal structures) highlighted in yellow and blue, respectively (left panel). The shaded triangle indicates one facet. The schematics show the distribution of capsid proteins according to the cryo-EM high resolution structure.[20] (b) Non-icosahedral components. A segment has been removed from the cryo-EM map to show the inner capsid contents. The schematics on the right hand side indicate tentative positions, as little is known about the structure and organization in the virion of the genome and accompanying proteins. Adapted from review San Martín, 2012.[19]

1.1.1.3 Core

The adenovirus genome is a linear double-strand DNA molecule of ∼35 kilobase pairs (for HAdV type 5) that is tightly packed inside the capsid. A peculiarity of adenovirus is that the viral genome is wrapped and condensed by viral proteins (figure 1.1 (b)).[28] The core proteins are V, VII and X (also known as μ). Two copies of the terminal proteins (TP) and a few of the viral protease (AVP) are also bound to the genome. Little is known about core organization within the particle since it does not follow icosahedral symmetry and it can not be reconstructed from cryo-EM or X-ray crystallography. The set of ∼500-800, ∼150 and ∼100-300 copies of polypeptides VII, V and μ, respectively, contributes in 25 MDa to the total 150 MDa virus mass.[29–31] AVP is the only core protein that has been solved by X-ray crystallography.[18]

Polypeptide VII is a histone-like protein, rich in arginine amino acid that confers positive charge. VII is responsible for wrapping and condensing the viral DNA.[32] The association of VII with the viral genome generates a complex similar to the nucleosomes of cells, termed *adenosome*, with a 10 nm beaded-like structure.[28,31,33] It is thought that polypeptide V bridges the genome and the capsid by interacting with IIIa and VI, but it does not contribute to genome condensation. On the other hand, polypeptide μ is a small protein that may also play a condensation role.[28,33]

The naked adenovirus genome is ∼11.9 μm in length, while associated to the condensing protein VII it reduces to ∼2 μm, ∼6 times smaller.[32] The adenosomes are not equally spaced, presenting distances between 10-130 nm.[33] They behave as soft repulsive particles within the crowded space of the packaged core.[31] Not many viruses with proteins associated to DNA are known. For example, the Simian Virus 40 (SV40) genome is condensed by histones of the host cell nucleus.[34]

Other genome bound polypeptides that do not play a condensing role are protein IVa2, found only at one vertex,[35] and several copies of

L1 52/55k[36] that together may trigger and guide genome packaging. L1 52/55k is removed from the particle by proteolysis.[37]

1.1.2 Adenovirus infection pathway

Unlike bacteriophages or herpesvirus, adenovirus does not eject its genome into the target cell nucleus leaving the intact capsid behind. Adenovirus is internalized in the cell and undergoes a stepwise disassembly for infection (figure 1.2).[38] Successful genome uncoating is as significant as genome protection during transmission between host cells. Viruses have optimized their structure to accomplish these two antagonist functions of the viral shell: protection and releasing. Evolution has precisely programmed a complex protein shell that dismantles with accuracy at the exact moment triggered by specific external signals.

Adenovirus uncoating starts at the plasma membrane of the target cell. The virus binds with its fiber knob to mobile receptor molecules (CAR – coxsackievirus and adenovirus receptor).[40,41] As the fiber is flexible, it allows the RGD motif (arginine-glycine-asparagine) of penton base to interact with integrins ($\alpha v\beta 5$) and inducing a conformational change.[42,43] The combined mechanical interactions result in fiber shedding, and presumably also penton release.[40] The internal viral protein VI is exposed, forming small pores in the plasma membrane that trigger a membrane repair process which leads to the uptake of the virus in endosomes.[44] The virus is engulfed by the membrane and internalized in endosomes. The membrane lytic function of protein VI induces rupture of the endosomal membrane allowing the virus escape, independently of pH decrease (acid).[44–47]

The partially disrupted virus particle is transported along microtubules by motor-proteins to the nuclear pore complex where it docks (figure 1.2).[38,48,49] At the nuclear pore complex, the genome is released by mechanical forces arising from the antagonistic action of kinesin motor-proteins against the holding force of the nuclear pore complex where the virus is attached.[50] The genome is inserted in the

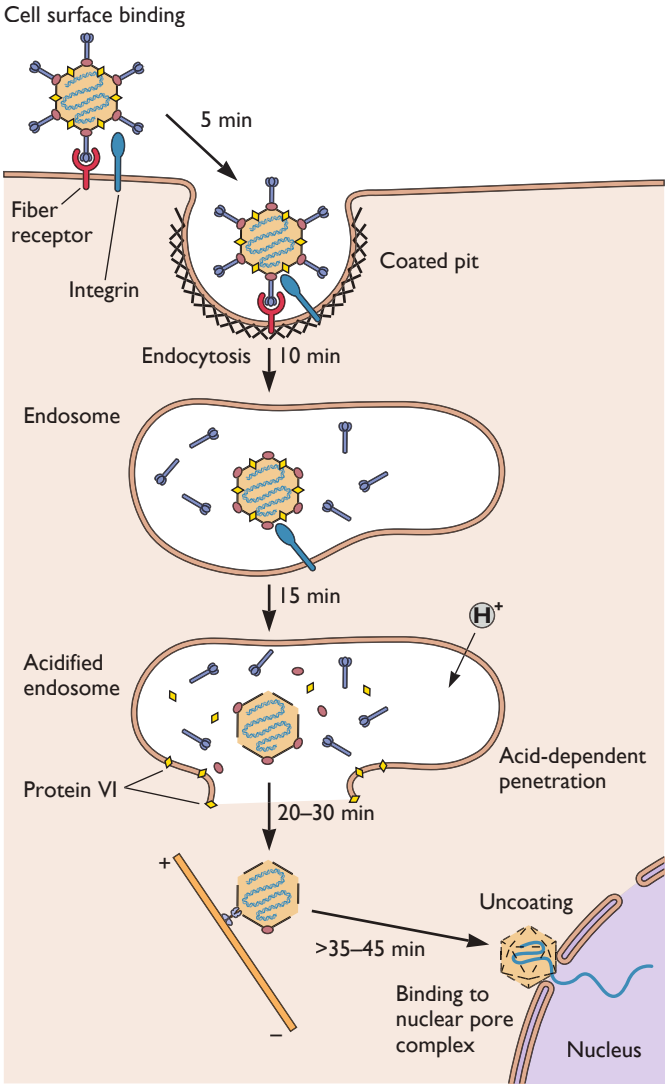

Figure 1.2: Adenovirus infection pathway. Adenovirus binds the cell receptor via the fiber protein. Interaction of the penton base with an integrin receptor leads to internalization by endocytosis. Thanks to protein VI exposition, the virus is able to escape form the endosome. The capsid is transported in the cytoplasm along microtubules and docks onto the nuclear pore complex where the genome is translocated into the nucleus. Scheme adapted from the book *"Principles of Virology"*.[39]

nucleus, replicated and transcribed. New viral proteins are produced in the cytoplasm and transported to the nucleus where new particles assemble.[39] The last step in AdV assembly consists in a proteolytic processing of some of the proteins forming the capsid and core by the viral protease.[51]

1.1.3 Adenovirus maturation

Double stranded DNA viruses, such as herpesvirus and bacteriophages, undergo expansion and drastic structural changes induced by a viral protease accompanied by genome packaging, preparing them to be actively infectious.[52,53] Adenovirus also suffers a maturation that primes it to be an infective particle.[18]

Adenovirus does not experience massive conformational rearrangements during maturation[26,54]. The viral protease cleaves precursors of the internal minor coat and some of the core proteins: IIIa, VI, VII, VIII, μ, L1 52/55k and the terminal protein.[18] The precursor proteins are termed with a "p" in front of the polypeptide name, *i. e.* the precursor of VI is pVI, and so on for the rest. A HAdV-C2 mutant called *ts1* does not undergo the proteolytic cleavages and is stalled at the immature state. Structural cryo-EM analyses comparing the *wild-type* mature virus and the immature *ts1*, showed differences concerning the inner side of the capsid, and in the viral core.[26,54]

One of the inner side capsid changes is an extra interaction between pIIIa and pVIII located between peripentonal hexons and those in the central plate of the icosahedral structure. This interaction may help to stabilize the peripentonal hexons.[26] The other reported change corresponds to a more uniform occupancy or ordering of pVI within the hexon cavity that may hinder its release during entry.[26,54] The most striking difference observed was related to the core. The Adenovirus core looses upon maturation, indicating that pVII and pμ have a stronger dsDNA condensing activity than their mature versions.

Maturation is essential to produce a metastable particle that pro-

tects the genome from aggressive conditions while permitting its correct delivery in new host cells. It has been proved that the *ts1* mutant is not able to infect the cells. This defect in infectivity is linked to a defect in uncoating. Immature *ts1* attaches to the host cell and follows the same internalization process as the *wild-type* (*wt*) virus but is not able to escape the endosome and is recycled or degraded in lysosomes.[55,56] The loss of infectivity might be related to the deficiency of penton release, or the incorrect deployment of polypeptide VI, or also to the excessive compaction of the genome.[26,27,57] Bulk techniques have proved that the immature *ts1* adenovirus is chemical and thermally more stable than the *wt* particle.[26,57]

1.2 Thesis motivation

Human adenovirus is a widely studied candidate for nanotechnology development in medicine and materials fields. One of its most powerful purposes is its potential as a vector for gene therapy.[15] Viruses have evolved reaching a very accurate and complex design to perpetuate their existence. Small changes in their encoding or configuration would lead to extinction or to more virulent particles. For example, a single amino acid mutation in a protein of the capsid structure,[58] or changes in DNA length in phages or adenovirus,[59,60] affect their structural stability, functionality and infectivity. A better comprehension of their composition, structure and dynamics, is a pillar for future studies in biotechnology engineering.

Bulk techniques are crucial in understanding virus behavior. From the last quarter of the last century, new techniques have been successful to study small samples such as viruses at single particle or molecule level, contributing to enlarge this knowledge. Some of these single particle techniques are made possible by the use of the family of scanning probe microscopes. This field started with the first images of a metal coated ϕ29 capsid taken with a scanning tunneling microscope in 1985.[61] Much has happened since then: nowadays viruses can

be manipulated with high precision in physiological conditions with atomic force microscopy (AFM), unveiling properties of viruses which allow to determine different physical factors that may affect in their functionality.

In particular, AFM studies have shown that the viral genome may affect the stability of the capsid. The presence of DNA inside of the capsid of MVM reinforces anisotropically the icosahedral structure.[62] Protein engineering experiments have shown that this reinforcement is mediated by DNA-protein interactions.[58,63] The packed genome inside the λ bacteriophage capsid doubles its rigidity.[64] It has been proved that this effect emerges due to an electrostatic repulsion between DNA strands in the case of ϕ29.[65] On the contrary, the herpes virus capsid does not seem to be affected by genome presence.[66] At the beginning of this thesis there were no physical studies on viruses with a genome associated with condensing proteins, such as adenovirus.

The thesis presented here arises as a collaboration between the group of Dr. Pedro José de Pablo of *Universidad Autónoma de Madrid* and Dr. Carmen San Martín of *Centro Nacional de Biotecnología* to determine the modulation of the mechanical properties of human adenovirus along the assembly/maturation and its relation with the infectivity. To fulfill this purpose, three different particles have been studied: mature HAdV-C5 *wild-type* virus (infectious), immature HAdV-C2 *ts1* (non-infectious, provided by Dr. S. Jane Flint of *Princeton University*), and empty capsids *FC31-L3*.[36] We proceeded by characterizing them with different methodologies based on AFM: probing the mechanical properties of capsids and confined cores, inducing a controlled mechanical fatigue disassembly, and detecting mechanically induced genome release with fluorescence microscopy.

Chapter 2

Basic Atomic Force Microscopy methodology

Microscopy is a technical field that uses instruments denominated microscopes to resolve small specimens that cannot be seen with naked eye. A probe is necessary to detect the specimen. For example, optical microscopy and electron microscopy use photons and electrons to solve the samples, respectively. Scanning probe microscopy (SPM) uses a sharp physical stylus as probe that scans closely the surface of the sample. The first microscope of this kind was the scanning tunneling microscope (STM)[67] that caused the award of the Nobel Prize for Physics to Binnig and Rohrer, along Ruska (EM inventor) in 1986. This microscope works by exchanging electrons by tunneling between a sharp metallic tip and a conductive sample.[68] The STM marked a new era in microscopy that resulted in the broad SPM family.

2.1 Atomic Force Microscopy

Based on the STM principles, Binnig, Quate and Gerber invented the atomic force microscope (AFM) in 1986.[69] In AFM, a sharp tip

situated at the end of a cantilever acts as a probe. By approaching the tip and scanning the sample surface, which in the setup we used is placed on a piezoelectric tube, the cantilever deflects depending on the attractive or repulsive interactions between the tip and the sample. A feedback algorithm acts on the piezoelectric and controls the tip-surface distance. Thus, a topography map of the sample is obtained from the surface scan.

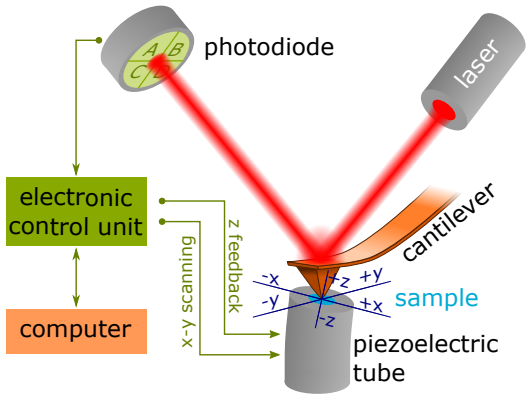

Figure 2.1: Main components of the AFM. The computer controls the piezoelectric tube deformation through the electronic control unit to adjust the tip-sample distance by measuring the deflection of the cantilever with the photodiode.

One of the most common methodologies to detect the deflection of the cantilever is the beam deflection (figure 2.1).[70] A laser beam is focused on the reflective back side of the free end of the cantilever, that mirrors the beam to a photodiode. The sectioned photodiode translates the reflected laser spot into a normal (F_n=A+B−(C+D)) and a lateral (F_l=A+C−(B+D)) force signals that correspond to the bending and the torsion of the lever, respectively. An electronic control unit receives these analogical signals that are sent to a digital signal processor (DSP) that translate them into digital data. The DSP manages the data and computes new parameters according to the set point introduced by the user through a computer. Analogical data are sent back to the electronic control unit, to modify the piezoelectric tube voltages and adjust tip-sample distance and lateral position. These voltage corrections computed by the DSP construct the topographical image. In this thesis, we have used a *Nanotec Electónica S.L.* microscope which is controlled by WSxM software.[71]

2.1.1 Cantilevers

Cantilevers are an important tool in AFM. The material and the shape determine the rigidity of cantilevers.[72] Usually, cantilevers are made of silicon or silicon nitride and have a metal coating on the back side for reflection. Cantilevers present different shapes (rectangular or V-shaped) and sizes that range between tens to hundreds of micrometers in length, tens of microns in width and from tenths to a few micrometers in thickness. Depending on the sample and the imaging mode, we will choose a cantilever with a specific shape and stiffness. For example, Dynamic Modes usually require stiff cantilevers, while a soft one is generally used for biological samples.

In general, manufacturers provide a nominal spring constant k_c (stiffness) for each cantilever but it is recommended to calibrate them. Among the available methods for calibrating cantilevers,[73] we used the one proposed by Sader *et al.*[74] This method obtains the stiffness of the cantilever k_c from its dimensions (L and b, the length and width of the cantilever, respectively), its fundamental resonance frequency ω_0, the quality factor Q, the fluid density ρ and the imaginary component of the hydrodynamic function Γ_i:[74]

$$k_c = 0.1906 \cdot \rho \cdot b^2 \cdot L \cdot Q \cdot \Gamma_i(\omega_0) \cdot \omega_0^2 \tag{2.1}$$

For the experiments presented in this thesis, we have used RC800PSA cantilevers (*Olympus*, Tokyo, Japan) that are rectangular silicon nitride cantilevers with nominal spring constant 0.05 N/m for chapters 3, 4 and 5, and 0.39 N/m for chapter 6.

The force (F) applied to deform a cantilever a distance Δz follows Hooke's law $F = k_c \cdot \Delta z$. This elastic response allows converting the voltage detected by the photodiode to force units (nN) as follows:

$$F(nN) = k_c \left(\frac{nN}{nm}\right) \cdot deflection(V) \cdot sensitivity \left(\frac{nm}{V}\right) \tag{2.2}$$

with *sensitivity*, the photodiode response (V) to the deformation of the cantilever induced by the movement Δz (nm) of the piezoelectric tube, previously calibrated with a grid sample of known dimensions.

2.1.2 Interactions between the tip and the surface

Atomic force microscopes are very versatile, since they can operate in vacuum, ambient or liquid conditions. The interactions between the AFM tip and the sample surface depend on the working medium, and the tip and sample nature. All the experiments in this thesis were conducted in liquids.[75,76] Generally, the tip-sample interaction can be described with an inter-molecular Lennard-Jones potential (figure 2.2)[77]

$$w(r) = 4\varepsilon \left[\left(\frac{\sigma}{r} \right)^{12} - \left(\frac{\sigma}{r} \right)^{6} \right] \tag{2.3}$$

with ε the potential well, σ the distance at which the inter-particle potential is zero and r the distance between the particles. This potential is the result of attractive and repulsive interactions.[78] Repulsive forces prevail below the equilibrium distance r_{eq}, where the net force is null; for distances above r_{eq}, attractive forces become predominant.

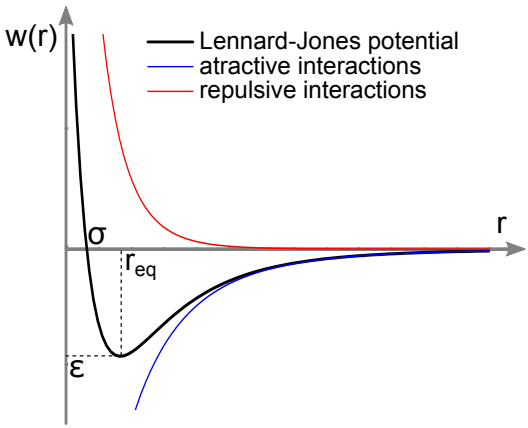

Figure 2.2: Lennard-Jones interaction potential. Inter-molecular interaction potential *w(r)* (equation 2.3) as a function of distance r (black line), that is an addition of attractive (blue line) and repulsive interactions (red line). The tip and the sample enter in contact at the equilibrium distance r_{eq}, where the force is null.

The forces measured in AFM are ultimately of electromagnetic and quantum-mechanical origins. In the absence of external fields, the main forces at the nano-scale level for different mediums are:[77,79]

- **Vacuum conditions.**
  - *van der Waals force.* It is a long-range attractive force, with a range of 10 to 15 nm. This force is present in all

mediums and varies with the chemical composition of the tip and sample. van der Waals force arises from interactions between permanent or induced dipoles of atoms and molecules. Its contribution can be minimized by using very sharp tips to sense forces affecting a few frontmost atoms of the tip.[80]

- *Coulomb electrostatic force.* These attractive or repulsive long-range forces are cause by the presence of electrostatic charges in the tip and/or sample.
- *Chemical interaction force.* These short-range (subnanometer) forces are responsible for molecular and atomic bonding.
- *Contact force.* They are short-range repulsive forces between atoms and molecules that arise from Pauli exclusion principle and ionic repulsion. These contact forces deform particles by displacing their atoms and molecules. There are models that describe these deformations, *e. g.*, Hertz model.

- **Ambient condition.** In this media, all the forces described for the vacuum condition are present, but an extra attractive force arises in AFM:
  - *Capillary force.* In ambient conditions, a thin film of water condensates on hydrophilic surfaces. A meniscus forms when the tip is brought close to the surface, increasing the tip-sample adhesion.

- **Liquid condition.** In this medium, the capillary force disappears because the tip is totally surrounded by water molecules, but the chemical and the contact forces remain the same. The van der Waals attraction range is screened by one order of magnitude (1-2 nm),[77,80] and the electrostatic force range depends on the nature and concentration of electrolytes in solution. These two forces are described by the DLVO theory. Moreover, an ex-

tra force arises when working at the nanoscale level in aqueous medium due to water molecules themselves.

- *Hydration force.* Solvation or structural forces (when the medium is water – hydration forces) are short-ranged repulsive ($\sim$ 0.07 nN) interactions that decay exponentially with a range of 2-5 nm. Usually, the repulsion is attributed to the removal of ordered water molecules from the surfaces.[81–83]
- *DLVO force.* It is a theory termed after Boris Derjaguin and Lev Landau, Evert Verwey and Theodoor Overbeek. It describes the forces between charged surfaces interacting in liquid, combining the screened van der Waals attraction and the electrostatic double Debye layer contribution (EDDL). The EDDL contribution describes the interaction between two charged surfaces surrounded by the electric double layer, which is formed by counterions and coions of the electrolyte solution. The double layer screens the surface charges and decays exponentially in a range set by the *Debye screening length* λ_D. This length depends only on the charge z_i and concentrations c_i of the electrolyte specimens (i):[77,82]

$$\lambda_D = \left(\frac{\varepsilon_0 \varepsilon K_B T}{e^2 N_A}\right)^{1/2} \cdot \left(\frac{1}{\sum_i c_i z_i^2}\right)^{1/2} \tag{2.4}$$

with ε_0 the vacuum permittivity ($8.85 \cdot 10^{-12}$ F/m), ε the dimensionless permittivity of the medium (for water $\sim$80), K_B the Boltzmann constant ($1.38 \cdot 10^{-23}$ J/K), T the absolute temperature (in Kelvin – K), e the electron charge ($1.60 \cdot 10^{-19}$ C) and N_A the Avogadro constant ($6.022 \cdot 10^{23}$ mol^{-1}). Generally, when the surfaces are brought together, their double layers overlap and a repulsive interaction appears.[84]

2.1.3 Resolution in AFM imaging

All microscopy techniques aim to attain their resolution limit. In conventional optical microscopy, diffraction limits resolution to the level of few a tenths of microns, as stipulated by Ernst Abbe. However in 2014, Eric Betzig, William Moerner and Stefan Hell were awarded the Nobel Prize in Chemistry *"for the development of super-resolved fluorescence microscopy"*, that it is based on the combination of *stimulated emission depletion* (STED) microscopy and single-molecule microscopy, reaching the nanometer level of resolution. On the other hand, electron microscopy and scanning probe techniques feature the highest spatial resolution, approaching the molecular and atomic levels.

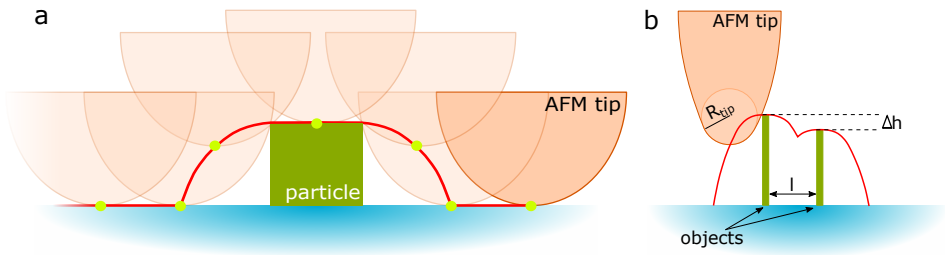

Figure 2.3: Tip dilation and AFM lateral resolution. (a) Illustration of object dilation with an AFM tip. The lateral size of objects appears larger due to the AFM tip physical dimensions. The red line represents the AFM acquired data. (b) Scheme of AFM resolution of two point particles. Lateral resolution is strongly conditioned by the tip size. Adapted from the thesis of Dr. Fuentes-Pérez and the work of Martínez *et al.*[85,86]

In AFM the resolution, apart from the instrumental factors, is mainly limited by the cantilever and its tip. The physical size of the tip limits the spatial resolution.[72] Lateral resolution l between two sharp features imaged by a parabolic tip with end radius R_{tip} is (figure 2.3 (b))[86]

$$l = \sqrt{2R_{tip}}\left(\sqrt{\delta z} + \sqrt{\delta z + \Delta h}\right) \tag{2.5}$$

where δz is the vertical resolution and Δh is the height difference

existing between the adjacent features. Thus, the lateral resolution in AFM improves with sharp tips.

Moreover, objects probed by the AFM appear dilated, *i. e.* objects show an apparent lateral expansion (figure 2.3 (a)). There are algorithms that correct this dilation,[87] although it would be necessary to know exactly the tip radius and shape, which may vary along the measurement due to tip contamination creating artifacts in the topographical data. This effect does not affect lateral resolution.

On the other hand, AFM reaches very high vertical resolution. It is conditioned by the noise of the system detection $\delta z_{detection}$ and the thermal noise of the cantilever $\delta z_{thermal}$:[85]

$$\delta z = \sqrt{\delta z_{detection}^2 + \delta z_{thermal}^2} \tag{2.6}$$

Thermal noise greatly affects the vertical resolution, and depends on the cantilever properties.[72] The amplitude of oscillation of a cantilever due to thermal noise depends on its spring constant k_c:[88]

$$\delta z_{thermal} = \sqrt{\frac{4k_B T}{3k_c}} \tag{2.7}$$

with k_B the Boltzmann constant and T the absolute temperature. Vertical resolution depends also on the cantilever rigidity. Most of the cantilevers used in this thesis, the Olympus RC800PSA with nominal spring constant of 0.05 N/m, reach a vertical spatial resolution at room temperature of $\sim$0.3 nm.

It is worth mentioning that the medium may also contribute to the resolution, although with lower influence than thermal noise. For example, the *Debye screening length* (equation 2.4) can be modulated by tuning electrolyte concentration in liquid conditions, diminishing the repulsive electrostatic forces for samples with surface charge density,[77,81] and improving slightly the topographical resolution.[89]

2.1.4 Imaging modes in AFM

Atomic force microscopes measure with high accuracy the deflection of the cantilever due to interactions between the tip and the sample. The ability to measure these interactions open a wide range of possibilities to operate the AFM, not only visualizing the topography of the sample surface but also allowing to study the interaction tip-sample interaction. In this section, we report a brief description of a few AFM operation modes, emphasizing the mode most used in this thesis: Jumping Mode Plus.[90,91]

2.1.4.1 Contact Mode (CM)

It is the most basic and first developed AFM mode.[69] In CM, the AFM operates at a constant tip-sample distance[80] or most commonly, at constant normal force.[69] In this mode, the AFM tip is brought into contact with the surface until the photodiode registers a pre-set normal force for the cantilever, that can be approximated to the Hooke's law $F_n = k_c \cdot \Delta z$. Then, the tip scans the substrate to obtain a topographic map (figure 2.4). The feedback algorithm compares the photodiode signal F_n with a set point reference to adjust the vertical position of the sample to fulfill the constant force condition. The Z voltage that sets the piezoelectric position at each point corresponds to a topographic point. Since the piezoelectric tube is previously calibrated with a grid sample of known dimensions, the voltages are converted into lengths and the topographic map is obtained.

CM can be operated at any interaction regime, but it is common to operate at the short repulsive force range where the tip and sample are in total contact. When the AFM tip is in contact, it does not only exert normal forces on the sample, but also lateral forces due to the torsion of the cantilever during scanning.[92] Then, samples suffer high and uncontrolled lateral forces, up to tens of nN.[93,94] Soft samples may deform irreversibly while scanning in CM, making this mode the less convenient for probing biological samples and especially iso-

lated viruses. Nevertheless, 2D crystals of biological material in aqueous solutions, such as purple membrane or ϕ29 head-tail connector, were imaged at high resolution with CM,[95–97] because these specimens do not present abrupt topographical changes and are surrounded by neighboring particles that protect them form being swept away.

2.1.4.2 Dynamic Modes

The Dynamic AFM operation Modes arose to minimize the uncontrolled lateral forces induced by CM[98] in addition to the blunting of the tip. In this operation mode, the cantilever is oscillated close to or at its resonance frequency (figure 2.4).[79] The oscillating amplitude decreases when the tip is approached to the sample, because the resonance frequency changes with the tip-sample interaction force and dissipation F_{ts}. The complex movement that the cantilever describes, can be simplified by the motion equation of the "point mass spring" model, where the cantilever-tip is described as a point-mass spring that moves in only one direction (z) and behaves as a driven and damped harmonic oscillator.[99,100] The nonlinear, second-order differential equation that describes the oscillation is:

$$m\frac{d^2z}{dt^2} + \gamma\frac{dz}{dt} + k_c z = F_{ts} + F_0 cos(\omega t)$$

The first and third elements of the left-hand side of the equation describe the harmonic oscillator of mass m and the force constant k_c. The second element of the left-hand side corresponds to the damping where γ is the damping coefficient that depends on the fluid viscosity. The first element of the right-hand side of the equation represents the interaction forces between the tip and the sample F_{ts}, and the second is the driven oscillation with a external excitation force F_0 and frequency ω.

Amplitude Modulation (AM) and the Frequency Modulation (FM) are the most common dynamic modes. AM is the most basic Dynamic Mode, in which the cantilever is excited at its isolated resonance frequency. Changes in the oscillating amplitude determine the

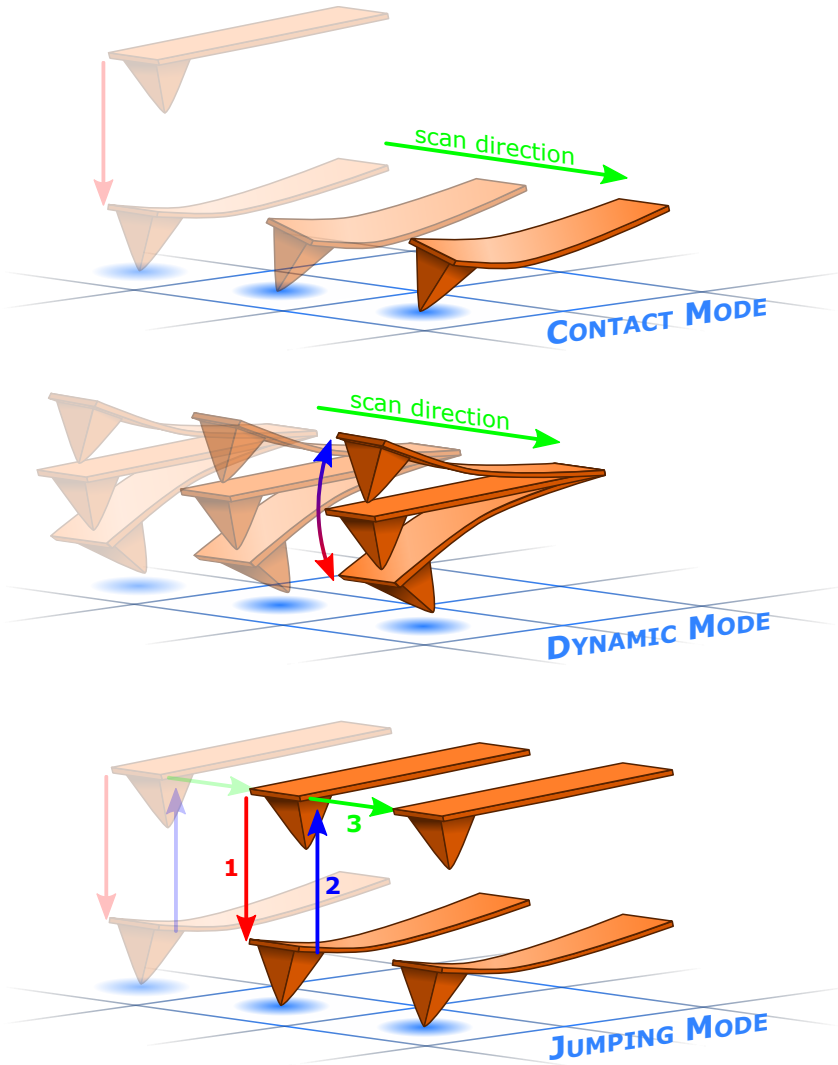

Figure 2.4: Schematics illustrating the different AFM imaging modes. In Contact Mode (CM), the tip sweeps the surface without loosing contact, applying a constant force. In the Dynamic Modes, the cantilever oscillates at or near to resonance. In Jumping Mode (JM), the tip periodically jumps on the surface, approaching the surface (1) until reaches a maximum force. Then it withdraws (2) and at the farthest point from the surface moves sideways (3) to the next point. Jumping Mode is the most used imaging mode in this thesis.

tip-sample distance. The feedback algorithm compares the photodiode signal with the set point reference to adjust the vertical position of the sample, so that the constant amplitude condition is fulfilled. This process yields to topographic maps. On the other hand, in Frequency Modulation (FM), the oscillating amplitude is kept constant and the topographic maps are obtained from the variations in the resonance frequency.[79] AM has been used to study adenovirus disruption with AFM in combination with fluorescence microscopy in chapter 6.

2.1.4.3 Jumping Mode (JM)

Jumping Mode (JM)[101] combines features of Contact and Dynamic Modes, and is similar to pulsed force microscopy.[102] This mode works by performing a quick (tens of ms) force *vs.* distance curve (FZ) at each point of the scanned area, moving the tip laterally while at the farthest tip-sample distance, when it is out of contact, avoiding most of the lateral forces (figure 2.4). To reduce piezoelectric resonances, the FZ is performed using a sinusoidal voltage signal that is applied to the Z piezoelectric. In addition to the topography image, JM provides relevant information about other magnitudes such as adhesion[103,104] and stiffness of the sample at the nanometer scale. JM is particularly suitable for scanning in liquids, where the low adhesion forces allow using small Z displacements at each point.

Interpretation of the topography images taken in JM is simpler than in the case of Dynamic Modes. In this mode the feedback parameter is the cantilever deflection, as in the case of Contact Mode. An important additional advantage with respect to CM is that the zero force level can be reset at each image point to the value at the maximum tip-sample distance, thus preventing the typical normal force drift observed in Contact Mode experiments.

Jumping Mode operation encompasses the following steps (figure 2.5 (a)): at time t_1 the cantilever tip is at position x_1, z_1 moving to the right. The sequence describes a conventional jumping cycle on the s type region (uphill): in figure 2.5 (a,i), the tip is lifted (1), and

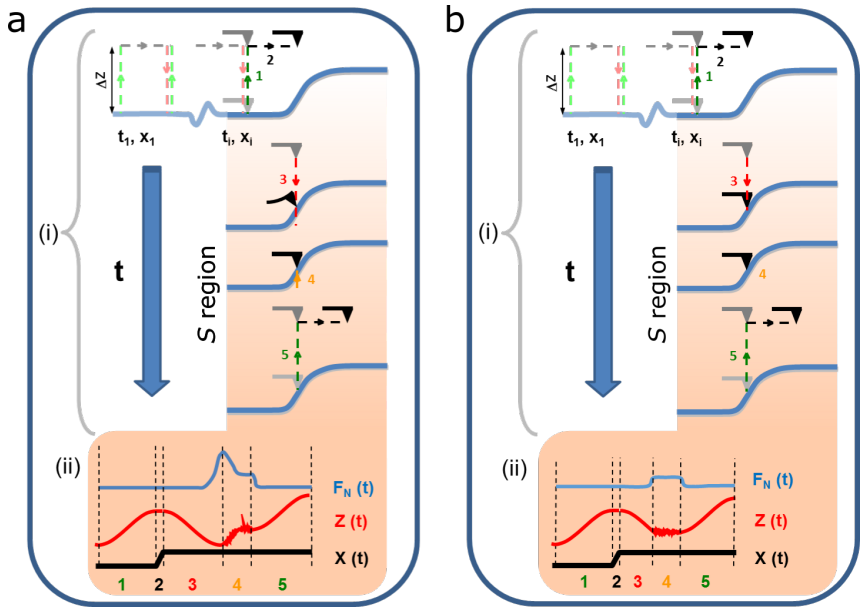

Figure 2.5: Jumping Mode (JM) and Jumping Mode Plus (JM+). (a) Scheme of standard JM. In uphill topographies (S region), the tip indents (i,3) exerting an extra force (ii,3) that may damage samples, but a feedback loop corrects the tip position (i and ii,4). (b) JM+ solves this problem by checking the force throughout the jump cycle.

then moves parallel to the sample surface (2). Afterwards (3), the tip approaches the sample by the same distance it had been lifted in (1). The feedback is switched on (4), adjusting the tip height to accomplish the set point force and acquiring the topography data. The tip is detached from the surface (5) and a new cycle begins. Figure 2.5 (a,ii) depicts the tip-sample lateral (lower) and vertical (middle) positions as a function of the time of the steps explained above. The upper line represents the cantilever deflection (F_N). At the end of tip movement (3), a clear peak in cantilever deflection (force) is produced as a consequence of the Z piezo approach in the uphill S region.

These peaks or residual forces in JM can be very harmful when scanning samples which present a steep uphill, such as viruses. The

tip vertical excursion is overestimated and the sample is over-indented, resulting in an additional force that can damage delicate samples. In fact, when we proceeded to characterize human adenovirus with AFM, we observed that viral particles were disrupted in few scans (section 3.2.3.2).

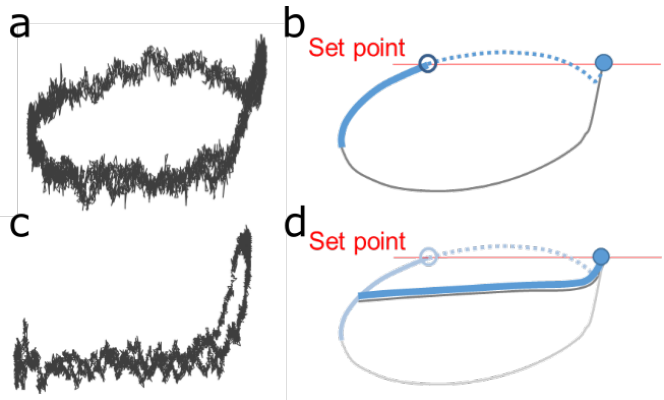

Figure 2.6: Cycle of Jumping Mode (JM) and Jumping Mode Plus (JM+). (a) JM cycle in liquids where the dragging force effect is clearly observed. (b) Cartoon of the JM cycle shows the set point level (thin horizontal line) and the feedback point (filled circle). The empty circle marks the Z turning point if the dragging force is not removed. (c) JM cycle with the new algorithm filters in normal force. (d) When the dragging force is removed, there is no intermediate Z turning point until the feedback point.

2.1.4.4 Jumping Mode Plus (JM+)

During my thesis we collaborated with *Nanotec Electronica S.L.* that introduced new developments in JM algorithms which improved its performance to identify conveniently the tip-sample contact at each image point and minimize the maximum forces applied during scanning.[105] Instead of moving the tip a previously set distance Z for the forward and backward cycles, the cantilever deflection is checked as it is approached to the surface, and it stops if the deflection is greater than the set point (movement (3) in (i) and (ii) in figure 2.5 (b)).

This option had already been implemented in JM operation, but was seldom used when working in liquid because its functionality was limited by the viscous dragging of water on the cantilever: as the cantilever approaches the surface the dragging force produces a spurious deflection that hides the tip-sample contact point (figure 2.6 (a)). If the dragging deflection equals the feedback set point force, then the Z piezo retracts before tip-sample contact (figure 2.6 (b)). This problem required performing JM force curves slowly enough to reduce the dragging as much as needed, decreasing the imaging speed below acceptable values.

The Reynolds number $Re = \rho v D/\mu$ for a cantilever of size $D \sim 0.1$ mm moving with velocity $v \sim 1 - 10\mu$ m/s in a solution of water (density $\rho \sim 1000$ kg·m^{-3} and dynamic viscosity $\mu \sim 10^{-3}$ Pa·s), is lower than 1. Then, the new algorithm assumes a viscous resistance under a laminar flow expression for the dragging force $F_d = -bv$, where b is a constant that depends on both the viscosity of the liquid and the geometry of the cantilever, and v is the velocity of the cantilever. The algorithm filters the normal force in real time during data acquisition by subtracting this dragging contribution from the raw normal force signal that hinders the determination of the contact point (figure 2.6 (c) and (d)).

This version of Jumping Mode operation (JM+) removes the dragging force, accurately detecting the tip-sample contact. This improvement in JM+ was essential for the development of the work described in chapters 3, 4 and 5 of this thesis.

2.1.5 Force curve and indentation

AFM not only can image samples, but it can interact closely with them obtaining physical properties. Generally, AFM is operated to obtain mechanical properties although depending on the operation mode nother physical features can be derived, such as magnetic or electric properties. In the work done in this thesis, we focused exclusively in the mechanical properties of adenovirus by probing the

sample with force *vs.* distance curves (force curve−FZ).

A force curve consists in the displacement of the piezoelectric in the Z direction registering the cantilever deflection with the photodiode. Assuming that the tip of the cantilever and that the substrate are too stiff to deform, we could consider that the deflection pertains only to the linear elastic deformation of the lever. When a FZ is performed on the sample, by indenting the tip in the surface of the specimen, we can derive some mechanical properties similarly to the macroscopic stressâĂŞstrain curve of materials science.[106] Using equation 2.2, we can present the force curve in nanoNewtons *vs.* nanometers enabling to obtain physical parameters such as the stiffness (N/m).

The samples may present a plastic or an elastic response. In this thesis, we probe the mechanical properties of viruses which generally deform linear and elastically.[10,107] Then, when we push on viral particles with the AFM tip, the signal recorded by the photodiode correspond to a linear deformation of the cantilever and the virus. This problem can be simplified to a system of two springs in series:

$$\frac{1}{k_{sys}} = \frac{1}{k_s} + \frac{1}{k_c} \tag{2.8}$$

With the rigidity of the cantilever k_c and the slope of the FZ k_{sys}, we can compute the stiffness of the sample k_s.

The FZ encloses the deformation of the cantilever and the sample, but a curve that represents the force *vs.* the indentation (or deformation) of the sample is easy to compute by just subtracting the deflection of the cantilever to the Z movement of the piezoelectric:

$$indentation = Z - deflection \tag{2.9}$$

The rigidity of the sample k_s can be obtained directly from the linear slope of this curve. A MATLAB code was implemented to ease the calculation of this curve from raw data of the microscope and to obtain the mechanical properties of the sample (appendix A.1). Along the manuscript, we refer to force *vs.* the indentation curve as indentation or nanoindentation.

Chapter 3

Characterization of human adenovirus with AFM

3.1 Introduction

Structural virology is one of the fundamental branches of virology that focuses on resolving virus structure at molecular or even atomic resolution. Structural virology has always advanced hand in hand with technological progress, starting in the first half of the 20th century with the visualization of first virus structures by electron microscopy (EM).[108] By mid-century, X-ray crystallography resolved molecular structures of biological samples such as DNA.[109] From that moment on, these techniques played an important role in viral structure comprehension by resolving viral capsid proteins and whole viruses.[108]

In the last decade, atomic force microscopy (AFM) has gained little by little a place in structural virology. AFM can reach high resolution imaging for viral particles.[110] The resolution obtained depends not only on the AFM tip radius (chapter 2), but also on the imaging mode, the sample support and the medium. AFM does not intend to compete with EM and X-ray as an imaging tool since nowa-

days these techniques resolve atom positions in virus structures.[17,72,111] Even though AFM does not reach sub-nanometer imaging resolution, it allows to manipulate and interact nanometer sized viruses at single particle level in close to physiological conditions.[10,62,107] As in materials science, from the AFM manipulation experiments, one can derive physical properties such as the stiffness and the fracture point (breaking force) of viruses, among others.

The first description of adenovirus with AFM consisted in the characterization of the state of the viral capsid in the initial step of capsid disassembly in air conditions.[110] Imaging in liquids allows probing viruses ambient conditions close to these that they may face in nature. Taking advantage of AFM, we manipulate adenovirus obtaining further information to understand its architecture. Along this chapter, we present our experience on imaging adenovirus with AFM in physiological conditions at high resolution, as well as the first characterization of the mechanical properties of adenovirus particles in different assembly states.

3.2 Optimization of the experimental setup for adenovirus

AFM belongs to the scanning probe microscopy family. Since this kind of microscopes scan a surface,[112] the object under study (virus particle) must be attached on a substrate. There is a wide range of possibilities to adsorb molecules on surfaces, but we are not interested in modifying their structure by covalent bounds (chemisorption). Thus, a requirement to adsorb viruses on surfaces is to find conditions that facilitate a strong physisorption without structural modification. Electrostatic and van der Waals forces play an important role in virus attachment. Depending on the polar, non-polar and charge density patches at the surface of the specimen, we have to play with the environmental conditions where specimens are embedded to promote physisorption to the substrate. Generally, the outer side of the protein

capsid of some non-enveloped viruses,[113] and in particular of adenovirus, is negatively charged (figure 3.1).

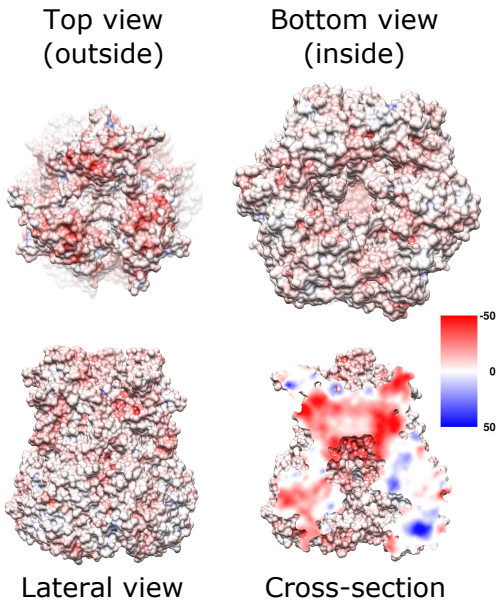

Figure 3.1: Hexon electrostatic potential. The hexon, adenovirus major coat protein, plays an important role in virus attachment. The surface electrostatic potential shows that its is predominantly electronegative (red). Blue depicts positive surface charge density, and white neutral charge in $k_B T/e$ units, where e is the electron charge, k_B the Boltzmann constant and T=298.15 K. Courtesy of Dr. San Martín.

3.2.1 Surfaces

It is important to know the properties of each surface and which interactions may govern the adsorption of samples. Here, we present a brief description of the common surfaces used for biological samples in AFM.[114]

3.2.1.1 Highly Ordered Pyrolytic Graphite (HOPG)

HOPG is a high purity carbon non-polar surface.[115] HOPG presents a layered structure from which a few graphite layers can be removed by pressing with a piece of tape and pulling off, resulting in a freshly cleaved surface. The higher the HOPG quality, the larger flat areas are obtained with lower number of steps, that correspond to a few layers

of graphite (a monolayer height is ∼0.34 nm). The first image of figure 3.2 shows the AFM topography of HOPG presenting the characteristic terraces.

The non-polar character of the HOPG surface results in a hydrophobic behavior that excludes polar and charged molecules resulting in an apparent hydrophobic interaction. The hydrophobic patches of the biological sample may govern the adsorption to this surface.

3.2.1.2 Glass coverslips

Glass is an amorphous inorganic material composed of silicates, that presents a good optical transparency with a large use in window panes. A coverslip is a thin flat piece of glass with a broad use in optical microscopy. Generally, glass requires a tedious preparation for its use as an AFM sample substrate. Coverslips may be covered with organic contaminants which should be removed by washing in a KOH solution in water and ethanol, followed by ultrasonication in water. Glass by itself is hydrophilic because it contains many oxygen and hydrogen atoms on the surface that form hydrogen bonds with water. For this thesis, glass was modified with silane molecules (Hexamethyldisilazane - HMDS) conferring a hydrophobic behavior due to their methyl radicals CH_3 (the $2{\equiv}SiOH$ groups of glass react with the NH of the HDMS ($HN(Si(CH_3)_3)_2$) giving $2{\equiv}SiOSi(CH_3)_3$).[116]

Similarly to HOPG, the hydrophobic character of HMDS-coated glass may govern the adsorption of the biological sample to the substrate. Since glass is an amorphous material, its surface presents larger roughness but very flat areas (no terraces) compared to HOPG. The second image of the first row in figure 3.2 shows an AFM topography presenting the characteristic pores of the glass.

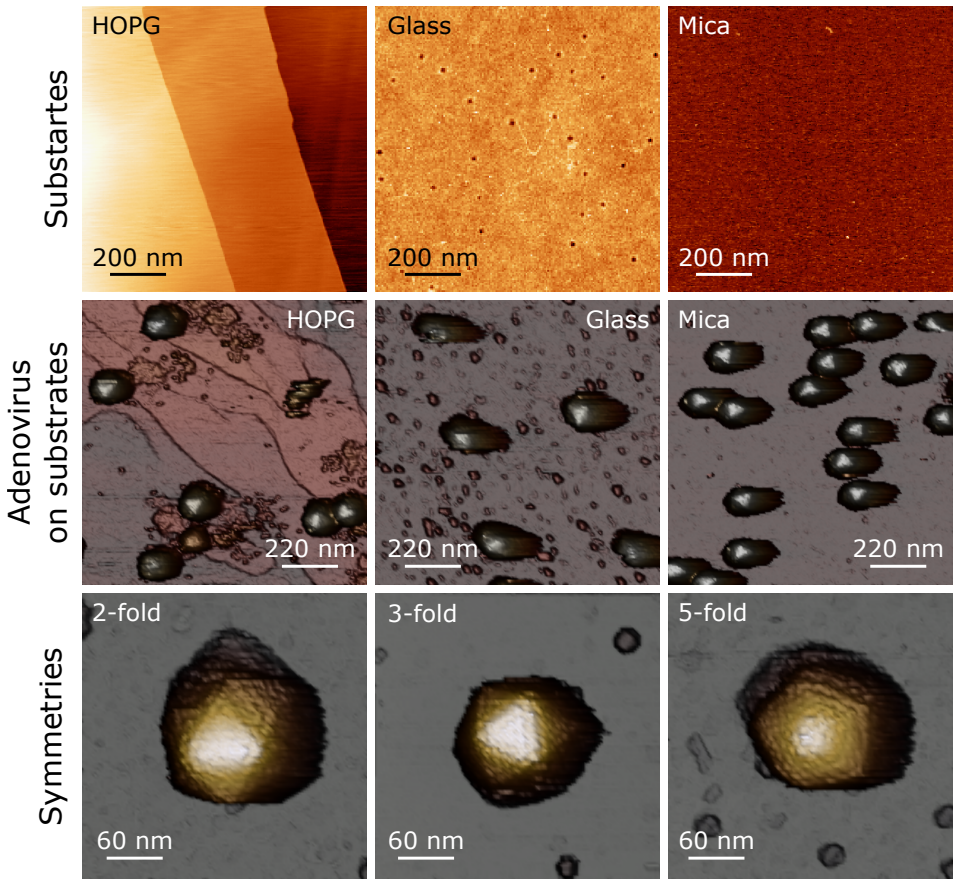

Figure 3.2: Adenovirus on substrates. The first row shows the AFM topographies of the substrates imaged in liquids with Jumping Mode. The images on the second row show adenovirus particles attached on the different substrates. Depending on the interactions between the surfaces and the particles, the virus tends to attach in different orientations with respect to the different symmetries of the icosahedron. The third row shows these symmetries. The 2-fold and the 5-fold symmetry orientation images correspond to adenovirus adsorbed on silane coated glass, and the 3-fold symmetry to adenovirus on mica in the presence of divalent cations.

3.2.1.3 Slice of mica

In this thesis we used muscovite mica ($KAl_2(OH)_2AlSi_3O_{10}$) which is a phyllosilicate mineral of aluminium and potassium.[117,118] The crystalline structure of mica forms layers that can be split or delaminated into thin sheets. Mica is easy to cleave with a piece of tape, similarly to HOPG. Freshly cleaved mica presents atomically flat surfaces with a very low roughness compared to glass (middle and right images of the first row in figure 3.2). In a water solution, some K^+ ions dissociate from the mica resulting in a negative surface. Playing with the electrolytes in the specimen solution and their concentration, the interaction forces between sample and surface can be modulated. The force interaction can be described by the DLVO theory,[77] that takes into account the van der Waals and electrostatic contributions (section 2.1.2). As opposed to HOPG and HDMS coated glass, mica presents a hydrophilic behavior. Figure 3.2 (image on the right of the first row) shows the AFM topography of mica, the flattest surface described in this thesis.

3.2.2 Adenovirus on surfaces

To characterize a new virus with AFM it is necessary to find the conditions that best adsorb the individual particles to the substrate. In this section, a description for the behavior of *wild-type* adenovirus in HBS buffer (composed by 20 mM Hepes and 150 mM NaCl at pH 7.8) on the above described surfaces is presented.

3.2.2.1 Adenovirus on HOPG

Adenovirus particles presented all the symmetries (last row in figure 3.2) in this surface with a slight dominance of adsorption on the three fold symmetry of the icosahedral structure (figure 3.3 (a) and table 3.1 at the end of the chapter). Particles adsorbed on the 5-fold symmetry showed the largest heights (figure 3.3 (b) and table 3.1). However, we

found that most of the adenovirus particles appeared disassembled on HOPG (middle row of figure 3.2). The disadvantage of HOPG is that it is very hydrophobic, meaning that it may denature proteins.[119,120] In the outer surface of the adenovirus capsid, there is a network of protein IX that lashes the GON hexons together.[20] In some nodes of the network, four of these proteins interact through their C-terminal helix by hydrophobicity. This helix bundle may have a higher affinity for HOPG when virus particles come close to the surface. It has been reported that hydrophobic surfaces destabilize α helices in proteins,[121] suggesting that HOPG may untie these bundles and destabilize some viral particles.

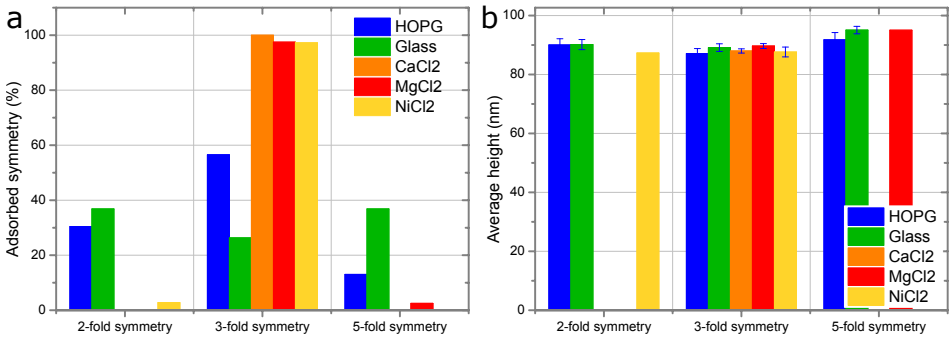

Figure 3.3: Adenovirus adsorption on different substrates. The graph in (a) shows the percentage of observed symmetry orientations for each substrate. In (b), the graph depicts the heights of the particles for all the symmetries on each substrate. Height is preserved for all of them, which means that the interaction with substrates is not large enough to deform the icosahedral structure. In both graph legends, $CaCl_2$, $MgCl_2$ and $NiCl_2$ refer to the cases of mica in the presence of these salts.

3.2.2.2 Adenovirus on silane coated glass

As in HOPG, adenovirus particles attached to silane coated glass in the three icosahedral symmetries (figure 3.3 (a) and table 3.1), but the 3-fold orientation was the least frequent. This is at difference with Snijder *et al.*,[122] who probed with AFM the three symmetries of

adenovirus on this surface, and found that the 3-fold orientation was the most abundant (45% of all the probed particles). This difference could be due to the short fiber protein mutant particle used in the cited work.[21] The short fiber ($\sim$ 9 nm) is less flexible than the natural Ad5 fibers used in this thesis ($\sim$ 37 nm),[21,24,123] hampering virus attachment in less stable symmetries.

Particles oriented along the 5-fold symmetry axis had the largest height, indicating that the surface does not affect the structure (figure 3.3 (b) and table 3.1). Glass is a convenient surface to probe the different symmetries of adenovirus (middle row on figure 3.2).

3.2.2.3 Adenovirus on mica

We tested a variety of electrolytes in the solution and their concentration (tens of mM), to attach adenovirus on mica. Three different electrolytes that, when entering in solution, present 2+ cations ($MgCl_2$, $CaCl_2$ and $NiCl_2$) were chosen for the tests.[117] Adenovirus attached to mica and presented a good stability on the surface for 10 mM $MgCl_2$ or $CaCl_2$, as well as for 5 mM $NiCl_2$.[124] For these concentrations with the buffer salts (150 mM of NaCl) the *Debye screening length* is small enough (up to $\sim$0.75 nm, equation 2.4) that it may enhance the van der Waals role in the attachment ($\sim$1-2 nm of range in liquids).[81,125] Figure 3.2 shows that adenovirus has a higher affinity to attach on mica showing up the triangular facet (3-fold orientation), conferring a high stability (figure 3.3 and table 3.1).

For the development of this thesis it was important that viral particles were firmly attached on the substrate. Mica in the presence of 5 mM of $NiCl_2$ was the surface and conditions that best fulfill the requirements to carry out the fatigue and viral core probing experiments that will be described in chapters 4 and 5, respectively. Although mica does not apparently affect viral structure, it was important to check if the divalent cations could affect it. Dr. Pérez-Berná analyzed the genome exposure of adenovirus for different concentrations of nickel chloride using fluorescence spectrometry, to see how the salt may af-

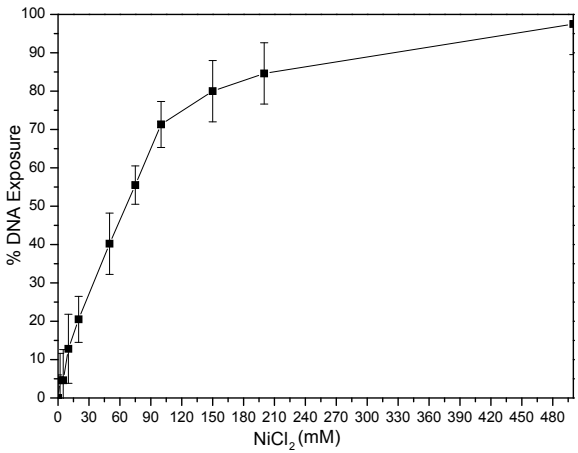

Figure 3.4: Exposure of adenovirus genome in the presence of different concentrations of $NiCl_2$. In this thesis, the experiments have been carried out using a concentration of 5 mM of $NiCl_2$, where genome exposure is negligible, which means that nickel does not affect viral structure. Courtesy of Dr. Pérez-Berná.

fect the virus structure (figure 3.4). For the range of 5-20 mM of $NiCl_2$, DNA exposure was almost negligible, enabling us to conduct AFM experiments on mica.

3.2.3 Probing adenovirus with AFM

Once we found the conditions to attach adenovirus to a substrate, we proceeded to characterize it topographically to identify the different characteristics of its icosahedral structure.

3.2.3.1 AFM sample preparation

Another challenge that we faced in the course of this thesis was sample storage. We realized that adenovirus samples suffer a loss of structural integrity if kept at 4 °C for over a week. Therefore, we stored virus preparations at -20 °C in HBS buffer in single-use aliquots of 5 μL. Generally for AFM imaging adenovirus in this thesis, virus samples were diluted in a solution of $NiCl_2$ in HBS to obtain a final solution of 5 mM of Ni^{2+} and virus concentrations between $1.5 - 2 \cdot 10^{12}$ viral particles per ml. A drop of 20 μL of virus solution was deposited

on freshly cleaved mica and incubated for 30 minutes at 4 °C before washing with 5 mM $NiCl_2$ in HBS. The AFM tip was pre-wetted, and the mica was placed on a holder and immersed in 500 μL of the same buffer. The virus is therefore maintained in a hydrated, close to physiological state throughout the experiments.

3.2.3.2 Imaging adenovirus with AFM

Adenovirus particles are large objects, presenting large orographic changes for the AFM tip, in particular a very steep uphill topography in the scan direction for the operation conditions of the imaging modes. When using small jump heights in JM, these sharp changes translate to uncontrolled peak forces that the sample has to withstand, as described in section 2.1.4.3. When imaging adenovirus with standard JM, most viral particles did not last more than a few images (figure 3.5). Moreover, a signal that viruses break due to the harmful AFM scan is that particles disrupted from the incoming scan direction.

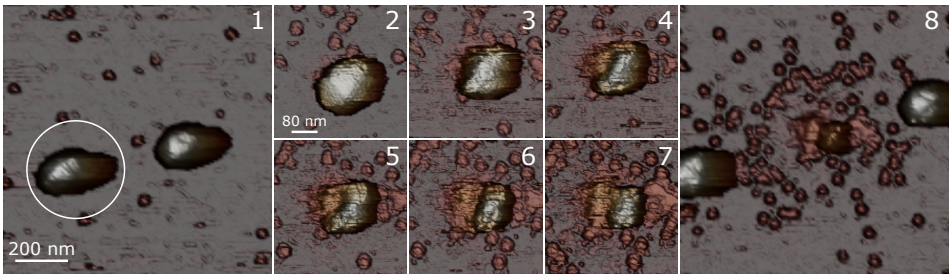

Figure 3.5: Adenovirus disruption due to AFM scan. This example shows how an adenovirus particle does not last more than 6 consecutive scans due to the extra peak forces of the standard JM. The particle disrupts following the scan direction, from left to right, meaning that it undergoes a scan-conditioned disassembly.

Thanks to the new algorithm developed by *Nanotec Electronica S.L.* for JM+ (section 2.1.4.4), adenovirus particles withstand a large number of scans before showing a total disruption (chapter 4). This

improvement allowed imaging human adenovirus at high resolution in physiological conditions without fixation agents such as glutaraldehyde to provide additional mechanical strengthening.[126] Figure 3.6 (a) shows that in these conditions, AFM not only solves capsomers but also their internal structure, distinguishing the monomers of the pentons (in yellow) and hexons (in blue) (figure 3.6 (b), and compare with figure 1.1). The topographical profiles show that AFM can resolve intracapsomeric distances of ∼5 nm and ∼6 nm between adjacent monomers for pentons and hexons, respectively.

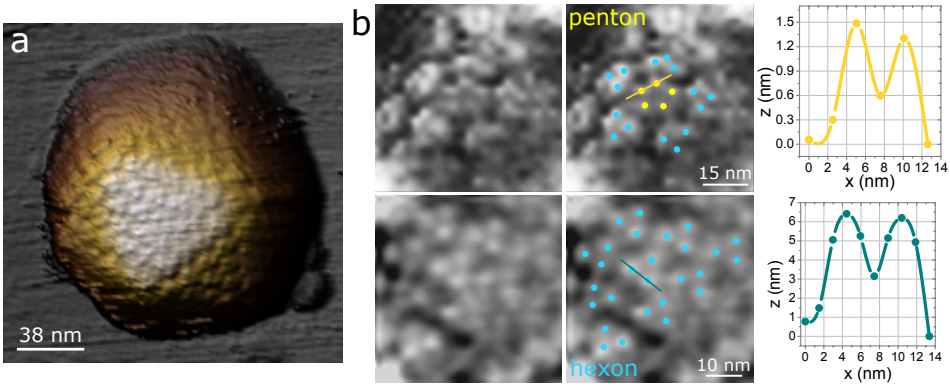

Figure 3.6: High resolution AFM image of human adenovirus. (a) 3D rendered topographical image of adenovirus in liquids presenting a view along the 3-fold symmetry axis (left). (b) The top and bottom rows show high pass filtered topographies of the vertex region and the central triangular facet of a virus, respectively, revealing the towers of the triangular hexons and the flower-like structure of the penton. On the right panels the lobes of the penton and hexons are highlighted with yellow and blue dots, respectively. The graphs depict the profiles of the two adjacent lobes of the penton and the hexon along the lines in the highlighted images.

3.3 Mechanical study of viruses

In the characterization of viruses, one of the main goals is to relate the viral structure and its dynamics with the functionality in a biological context. Bulk techniques like cryo Electron Microscopy or X-ray crystallography provide an average information about the structure of a large ensemble of virus particles. On the other hand, AFM is a single particle technique that provides local information on the physical properties of the sample. The possibility to work in aqueous mediums confers to AFM the potential to characterize biological samples in physiological conditions, not only as an imaging technique but also probing a wide range of physical properties that complement the information of the bulk techniques. Viral particle stiffness, surface charge density and dielectric constant are some of the physical properties that AFM can probe.[10,107,113,127]

3.3.1 Nanoindentation assays on particles

Some of the mechanical properties can be obtained from single indentations (section 2.1.5) with the AFM tip on the sample. To do so, the microscope performs controlled force *versus* distance curves (FZ), measuring the piezoelectric tube displacement in the Z direction and the deflection of the cantilever in the photodiode. From the forward and backward curves it is possible to obtain information that can be classified into *pushing* or *pulling* experiments,[128] respectively. In this thesis, we were interested on the information that can be derived from the pushing experiments, such as the stiffness and the fracture point (figure 3.7).[129]

To carry out AFM nanoindentation assays on viruses, we locate an individual intact particle on the surface (figure 3.7 (left)), and then the cantilever pushes at the very top of the particle. The FZ speed was about 100-150 nm/s Cantilever bending is recorded as a function of Z displacement.[129] During the first stage of indentation,

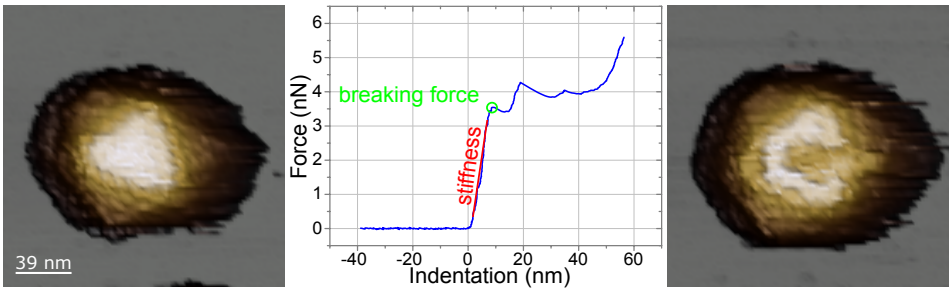

Figure 3.7: Force curve on an adenovirus particle. Force distance curve (FZ) executed in the center of the triangular facet of an intact particle (left). The stiffness and the fracture strength or breaking force can be obtained from the indentation curve (middle) computed from the FZ (section 2.1.5). The topographical image taken after the indentation shows that the particle was disrupted (right).

the virus particles undergo a linear deformation[130] that is reflected by an increase in the force indentation curve (figure 3.7 (middle)) and provides information on the stiffness of the virus. At a certain point, the force suddenly decreases due to capsid failure. This point determines the breaking force or fracture point. Finally, an image of the virus is taken to characterize its disruption (figure 3.7 (right)).

In general, non-enveloped viral particles present a linear elastic deformation,[10,62,107,131,132] that can be described with the *thin shell theory*.[130] The specimen must satisfy the condition that the thickness h and the deformation δ have to be lower than the radius of curvature R ($\delta \sim h$ and $h \ll R$).[130] Sometimes particles may present a transition to non-linear deformation described as a hertzian deformation (chapter 5).[133] Likewise, adenovirus particles were assumed to behave as thin shells where the force (F) increases proportionally to the particle deformation (δ, or the indentation of the tip on the virus): $F = k_v \cdot \delta$. The constant of proportionality k_v is the elastic constant of the particle which is a measure of the stiffness or rigidity. The elastic constant depends on the size and shape of the specimen, but the intrinsic parameter of the stiffness of the material is given by the Young's modulus (E). To compute the E would need of some assumptions, but

the spring constant can be derived directly from the indentation curve (section 2.1.5). In the thesis we compare properties measured on particles displaying a 3-fold orientation by extracting its spring constant as a direct measurement. Experimental data were analyzed from the indentation curve as described in section 2.1.5. The MATLAB program was used to compute the indentation from microscope raw data and obtain the values of the mechanical properties (appendix A.1).

3.3.2 First characterization of the mechanical properties of the mature and immature adenovirus particles

To probe the mechanical properties of adenovirus particles, we conducted the experiments in HBS buffer composed by 20 mM Hepes and 150 mM NaCl at pH 7.8. We used mica to characterize adenovirus, adding a divalent ion (Ni^{2+}) to the solution to attach the samples on the surface, as described in section 3.2.3.1. The FZ speed presented in this thesis in all experiments was about 100-150 nm/s.

Since adenovirus particles preferentially attached to the mica in a 3-fold orientation, all the nanoindentation assays were conducted on this symmetry. In an initial characterization of adenovirus mature (*wt*) and immature (*ts1*) particles, we recorded data of 26 *wt* and 28 *ts1* particles. We presented the stiffness data in histograms and fitted them to a gaussian distribution

$$f(k) = f_0 + \frac{A}{w\sqrt{\pi/2}} \cdot exp\left(-2\frac{(k-k_v)^2}{w^2}\right) \tag{3.1}$$

that provides the average value of the spring constant k_v of the particles and its dispersion, as well as the standard deviation $w/2$=SD (figure 3.8). A statistical analysis of data was carried out for the breaking force. Adenovirus *wt* particles presented both higher breaking force (3.3±0.2 nN) and stiffness (0.46±0.02 N/m) than *ts1* particles (2.3±0.2 nN and 0.38±0.04 N/m, see also table 3.2). The results

are presented as average±SEM, where SEM is the standard error of the mean SEM= SD/$\sqrt{n}$ and n the number of measurements.

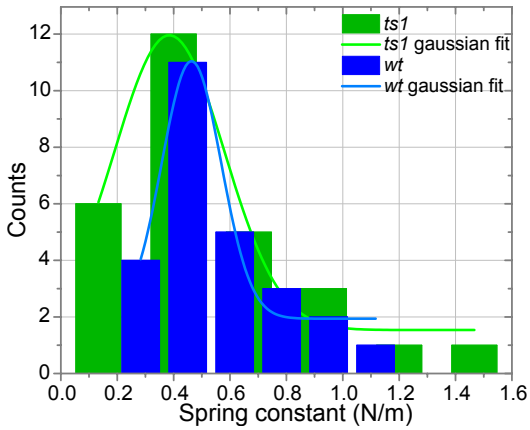

Figure 3.8: Spring constant distribution for mature (*wt*) and immature virus (*ts1*). Data are presented in histograms for *wt* (blue) and *ts1* (green). Mean value and their standard deviation (SD) can be obtained from fitting a gaussian distribution curve to the histogram. Mature particles are stiffer compared to immature.

Usually, mechanical strength and stiffness are considered a signature of virus stability,[66,134,135] *i. e.* the harder the particle, the more resilient to aggressive conditions. However, this may not necessarily be the case, because stiffness does not guarantee that a virus can survive in hostile chemical or thermal environments. This is the kind of behavior we find for adenovirus; immature *ts1*, which withstands higher levels of thermal or chemical stress than *wt*,[26,57] is softer and breaks at lower forces than *wt* when indented with the AFM tip. Conversely, the metastable *wt* virions appear mechanically stronger (breaking at higher forces) and stiffer. Thus, in adenovirus, mechanical stability does not correlate with thermal or chemical stability.

The adenovirus mature capsid is brittle and stiff compared to the elastic immature particle. Maturation drastically changes the core organization and reduces interactions that kept the DNA tightly condensed (section 1.1.3).[26,57] A possible explanation for the unexpected mechanical behavior of *wt* and *ts1* adenovirus particles would be that this relaxation of the core upon maturation may increase the internal pressure in the virion. The adenovirus capsid is usually thought to be pressurized, by analogy with other dsDNA viruses.[136] However, the case of adenovirus is different from that of bacteriophage, because the

dsDNA genome is forming a complex with a large quantity of charge-neutralizing proteins. These results lead to further experiments and discussion presented in chapter 5 in this thesis.

3.4 Conclusions

AFM characterization of a new virus sample requires a broad study probing different conditions such as surface election, the medium where viruses are immersed or the imaging mode, among other parameters. For human adenovirus, we found that the interaction between particles and mica in the presence of divalent ions in the medium allows a very stable physisorption of viruses on the 3-fold symmetry orientation without modifying their structure. Also the imaging mode plays an important role at resolution and in experiments development, as we will see for mechanical fatigue experiments in chapter 4. The results of nanoindentations assays showed that the *wt* particle is stiffer than the immature *ts1*, leading to the hypothesis of a pressurization during the maturation that will be addressed in chapter 5.

Tables

Symmetry	Adsorbed symmetry (%)					Average height (nm)									
	HOPG	Glass	$CaCl_2$	$MgCl_2$	$NiCl_2$	HOPG		Glass		$CaCl_2$		$MgCl_2$		$NiCl_2$	
						Avg	SD	Avg	SD	Avg	SD	Avg	SD	Avg	SD
2-fold	30	37	--	--	3	90	2	90	2	--	--	--	--	87	--
3-fold	57	26	100	97	97	87	2	89	1	88	1	90	1	88	2
5-fold	13	37	--	3	--	92	2	95	1	--	--	95	--	--	--

Table 3.1: Topographical characterization of adenovirus particles adsorbed to different substrates. Percentage of adsorption on the three icosahedral symmetries for different substrates, and heights on the different orientations for each substrate. Data depicted in figure 3.3.

Particle	Spring constant (N/m)	SD (N/m)	SEM (N/m)	Force (nN)	SD (nN)	SEM (nN)	n
wt	0.46	0.10	0.02	3.3	1.2	0.2	26
ts1	0.38	0.19	0.04	2.3	0.8	0.1	28

Table 3.2: Mechanical properties of *wt* and *ts1* adenovirus particles. Parameters obtained from the gaussian fit of the spring constant data depicted in figure 3.8, and statistical average for the breaking force.

Chapter 4

Monitoring dynamics of human adenovirus disassembly induced by mechanical fatigue

4.1 Introduction

Viruses have to deliver their genome into host cells.[137] Many bacteriophages inject their nucleic acid genomes into bacteria leaving their capsids behind. But most eukaryotic viruses, such as adenovirus, are engulfed by the host cell and undergo a controlled disassembly (uncoating) until their replication compartment is reached.[138] Signals received upon entering the host cell trigger a cascade of conformational changes in the proteins forming the viral shell, resulting in weakening and further disruption of the virion to expose its genome to the cellular machinery.[138] Different physicochemical agents may induce similar conformational changes in proteins composing viral shells, which ultimately surpass the activation energy of disassembly.[139] For instance, in poliovirus the same disassembly mechanism is induced by either binding to an immunoglobulin-like receptor on the cell surface (*in*

vivo) or exposure to moderate heat (*in vitro*).[140] Investigations into virus structural stability usually rely on bulk physicochemical procedures accompanied by Electron Microscopy (EM).[141–143] This imaging technique convey static snapshots lacking real time information about the dynamics of disassembly.[57] AFM nanoindentations, beyond capsid rupture strength,[65,66,122,126,144–146] induce mechanical failure of viruses, but likewise provide only a final image of the disruption process.

As explained in chapter 1, adenovirus disassembles in the cell in a stepwise manner,[38] beginning at the plasma membrane where receptor binding induces loss of protruding fibers.[41] Virion dismantling continues in the early endosome, where mild acidification, among other factors, may cause the release of a few pentons and peripheral core components.[47,57,147] The partially disrupted particle escapes the endosome and travels to the nuclear pore, where final disassembly occurs and the genome enters the nucleus.[148] The mutant *ts1* does not undergo the proteolytic cleavages that lead to maturation (section 1.1.3),[149] and the uncleaved precursor proteins make the immature particles more stable than the mature ones (*wild-type*), impairing proper uncoating and aborting infection.[57,150]

In this chapter, mature and immature adenovirus particles are subjected to a disruption method comparable to mechanical fatigue macroscopic assays in materials science. Jumping Mode Plus (JM+, section 2.1.4.4) allows to acquire topography images while at the same time applying very low forces. As the imaging forces are well below the breaking force of viral particles, the virus suffers subtle deformations (tenths of nanometer for 100 pN) that may induce weakening of inter and intra-capsomeric interactions for a large number of cycles. The weakened interactions are defects that act as seeds for fracture propagation in the protein shell. This "infinitesimal" capsid disruption allows us to solve the dynamics of intermediate disassembly viral states.

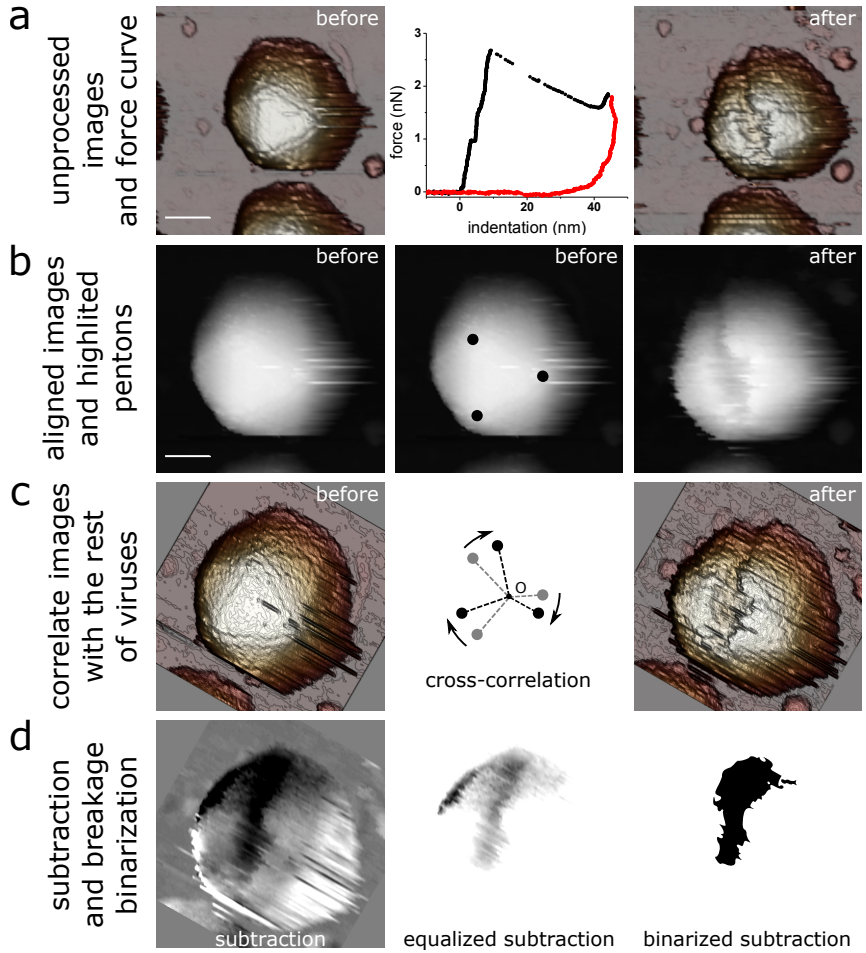

Figure 4.1: Adenovirus rupture patterns obtained by single nanoindentation assays. (a) 3D AFM topographical rendering of an adenovirus in 3-fold symmetry before and after the indentation (in the middle, forward and backward curves in black and red, respectively). (b) Aligned images in gray scale; pentons are highlighted with black circles in the middle image for cross-correlation of all viruses. (c) Rotation applied to have the same topographical orientation in all the images in the dataset. (d) Topographical subtraction of the aligned AFM images (left); the equalization of the subtraction highlights the breakage (middle); binarized map of the breakage region (right). The scale bar for (a) is 60 nm and for the rest (only depicted in (b)) is 48 nm.

4.2 Study of adenovirus disassembly patterns with AFM nanoindentations

The first approach to study viral disassembly is to perform classical nanoindentation assays with AFM. As explained in section 3.3.1, these assays consist of exerting a force exceeding the fracture strength at the top of the particle. Afterwards an image of the virus confirms its disruption (figure 4.1 (a)). To find patterns in virus disassembly, we compute breakage maps by comparing images of the initial intact virus topography state and the disrupted state.

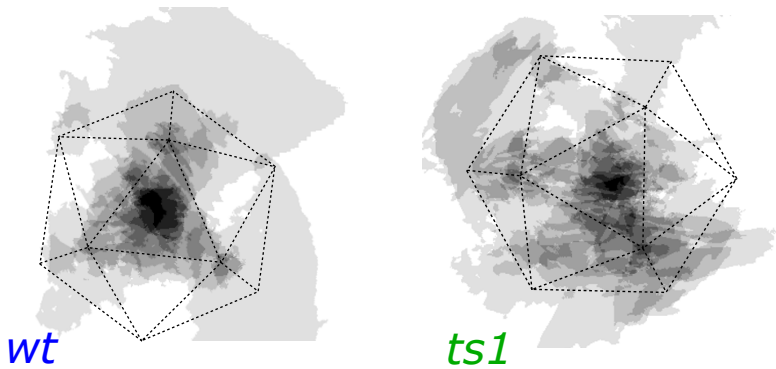

Figure 4.2: Breakage pattern maps corresponding to nanoindentations of 9 *wt* and 12 *ts1* adenovirus particles, respectively. Darker gray levels indicate higher frequency of breakage at these regions. The analyses show that viruses are mainly broken at the center of the facet, where the tip is meant to perform the indentation.

The first step to compute a breakage map corresponding to force-distance curves is the alignment between the AFM image before and after the force curve (figure 4.1 (b)). To carry out this alignment, the pentons on the upright facet of the intact virus image are highlighted with black circles to help the correlation process (middle, figure 4.1 (b)). Dr. San Martin aligned the complete image dataset using cross-correlation procedures in Xmipp2.[151] For this step all the images need to have the same dimensions (scale and points). Figure 4.1 (c) shows the resulting rotation of the cross-correlation of the pair of images in

the example. For each virus analyzed, a breakage map is computed by subtracting the final image after nanoindentation from the intact virion image (left, figure 4.1 (d)). The darker values show lost volume in the topography. To highlight the breakage region it is necessary to equalize the subtraction by skewing data and delimiting the area (middle, figure 4.1 (d)). The difference image is binarized to a gray level of 1 within the cracking area (right, figure 4.1 (d)).

To obtain the average breakage pattern due to the nanoindentations, all binarized breakage maps are overlaid (figure 4.2). The darker colors represent the highest frequency in breakage. The darkest area is at the center of the icosahedron facet, where the AFM tip indentates. These breakage patterns do not provide evident differences between *wt* and immature virus *ts1*. AFM nanoindentation assays fail to show differences in breakage pattern between mature and immature adenovirus that could explain the different uncoating behavior.

4.3 Mechanical fatigue approach

Material disruption induced by mechanical fatigue strongly depends on the number of load cycles and the stress of each one, as predicted by the Wöhler curve or *S-N* curve (section 4.4.2).[152] Jumping Mode Plus performs consecutive loading cycles of a few hundred pN (figure 4.3). This section explains that when we acquired successive images of the same particle at ∼100 pN, well below the capsid rupture force (section 3.3.2), these repeated loading series induced mechanical fatigue,[152] simultaneously triggering and enabling real time monitoring of adenovirus disassembly. Thus, mechanical fatigue acts as a stress agent, in a similar way to physicochemical procedures, inducing gradual capsid disruption.

In contrast to classical nanoindentation studies,[66] mechanical fatigue experiments require not only intact particles, but also stable attachment to the surface during several hours of repeated scanning on a single particle in liquid. Only adenovirus particles adsorbed on

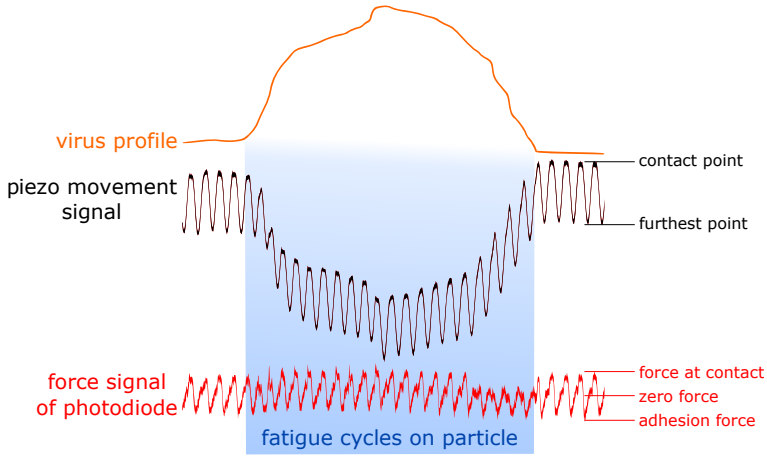

Figure 4.3: Jumping Mode Plus imaging force cycles. Cartoon depicting the JM+ imaging force cycles (red), as well as the z-piezo actuation (black) along a single scan-line.

3-fold symmetry orientations were stable enough, presumably because this geometry maximizes the virus-surface contact area. Once the consecutive imaging started, about 60% of viruses detached before disassembly ended. Nevertheless, a dataset comprising 7 *wt* and 6 *ts1* viruses was studied, revealing a consistent and reproducible behavior pattern as we explain presently.

To perform these experiments, images of 128x128 points^2 and 300x 300 nm^2 were recorded scanning from left to right at a temperature of 18°C to avoid thermal drift and any influence in virus disruption. The sample was immersed in a ∼560 μL drop of 5 mM $NiCl_2$ in HBS buffer to avoid salt concentration increase due to evaporation. Monitoring virus disassembly in real time was accomplished by repeatedly imaging each particle. To study the disassembly dynamics, all images corresponding to the same particle were aligned. As a control that disruption was caused solely by mechanical stress and not by changes in environmental conditions during the prolonged imaging time, we observed that at the end of the experiment capsids in the neighborhood of the disassembled one were still intact (figure 4.4).

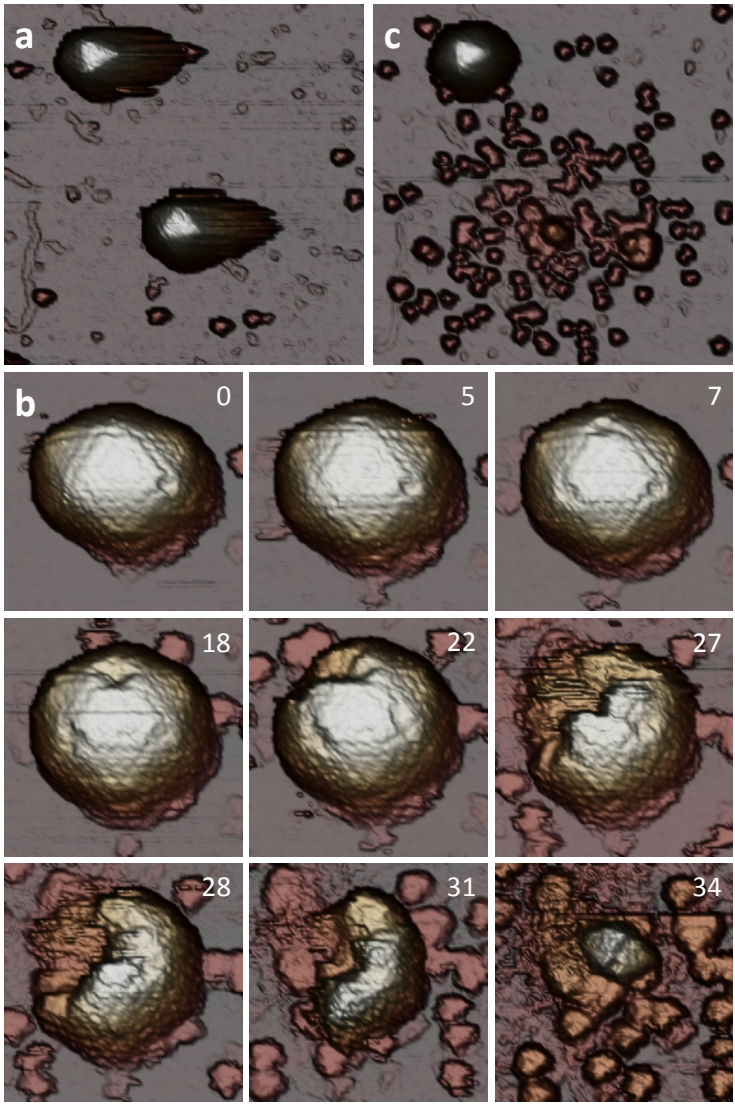

Figure 4.4: Virus disruption is due to mechanical fatigue, and not to the prolonged experimental time. (a) Two *wt* adenovirus particles attached to the surface before the disassembly experiment. (b) A set of different stages throughout the disassembly of the viral particle at the bottom are shown. The typical crumbling pattern for *wt* virus is observed. Frame numbers are indicated in each image. (c) The same area as in (a) imaged after the end of the disassembly experiment. The neighboring particle at the top remains intact after 126 minutes of experiment.

4.3.1 Topographical evolution study

We analyzed changes in the topography of adenovirus mature (*wt*) and immature (*ts1*) particles while being disassembled by mechanical fatigue. Since we study an evolution, data are analyzed in terms of elapsed time from the first acquired image for each individual particle.

4.3.1.1 *Wild-type* particle

Figure 4.5 (a) exemplifies the results obtained for a mature particle. The virus was scanned 61 times during 174 minutes, and a movie was generated from the consecutive images (*Movie_1_SciRep* – movie caption at the end of the chapter). Frame 0 in figure 4.5 (a) presents the intact particle of ∼86 nm height (figure 4.6 (d)), in agreement with the nominal diameter of 88 nm from facet to facet. Frames 4 to 9 reveal that pentons are sequentially lost from each vertex of the triangular facet. The upper right penton vacancy seeds a growing fracture (frame 24) that evolves into crumbling of the particle from right to left (frames 28 to 42), finishing in a blob which lacks the whole shell and most of the core (frame 61).

4.3.1.2 *ts1* particle

The *ts1* adenovirus particle in figure 4.5 (b) observed in ∼40 images taken along 118 minutes fell apart in a different manner than *wt*. Here pentons sequentially pop off at frames 1, 4 and 6 (*Movie_3_SciRep*). One of the two penton vacancies at the upper vertices of the triangular facet starts to grow at frame 12, presumably because peripentonal hexons are lost. Then the two simultaneous voids grow (frames 24 and 26) and coalesce (frame 27) in a crack. Finally the top of the capsid is totally removed and the viral core is exposed to the environment (frame 38).

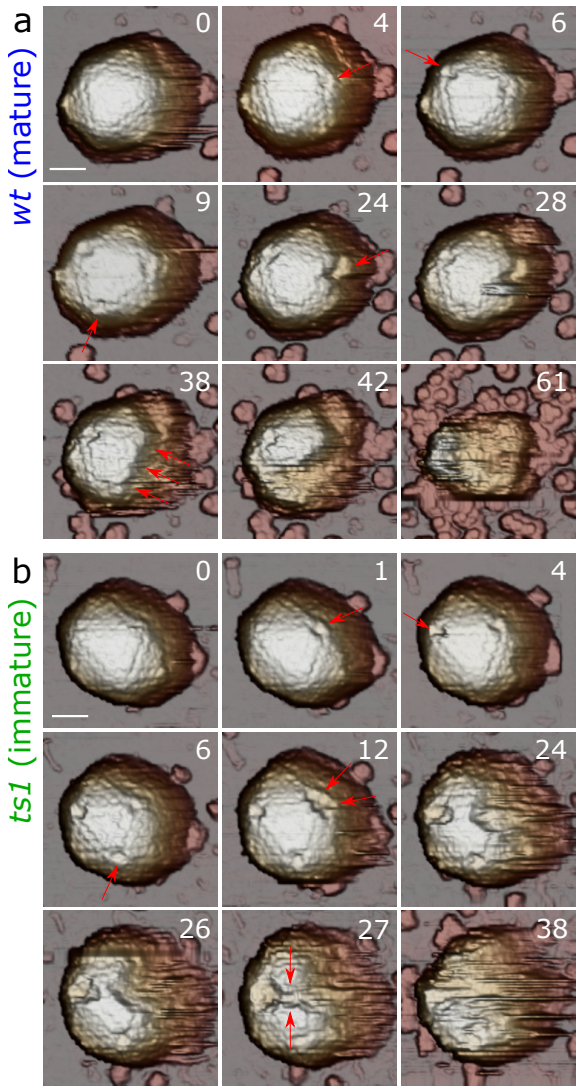

Figure 4.5: Disruption by mechanical fatigue of a *wt* and a *ts1* adenovirus particle. Selected individual frames along the disassembly process of a *wt* particle (a) and a *ts1* particle (b). *Movie_1_SciRep* and *Movie_2_SciRep* show complete image dataset. The numbers refer to the position of the frame on the corresponding movie. Penton vacancies are highlighted with arrows. In (a), frame 38, the arrows indicate the crumbling direction. In (b), arrows in frame 27 indicate coalescence of voids. Scale bars correspond to 46 and 40 nm for *wt* and *ts1*, respectively.

4.3.1.3 Height evolution analysis

The height of the virus respect the substrate is a quantitative description of overall virus integrity. To do so, kymographs (graphical representation of spatial position over time, figure 4.6 (b)) were generated by depicting the evolution of the topographical profile indicated by the dashed lines in frames 0 in figure 4.6 (a) (same particles of figure 4.5). Kymographs enable topographical profiles comparison along time (figure 4.6 (c), with critical profiles highlighted with colors).

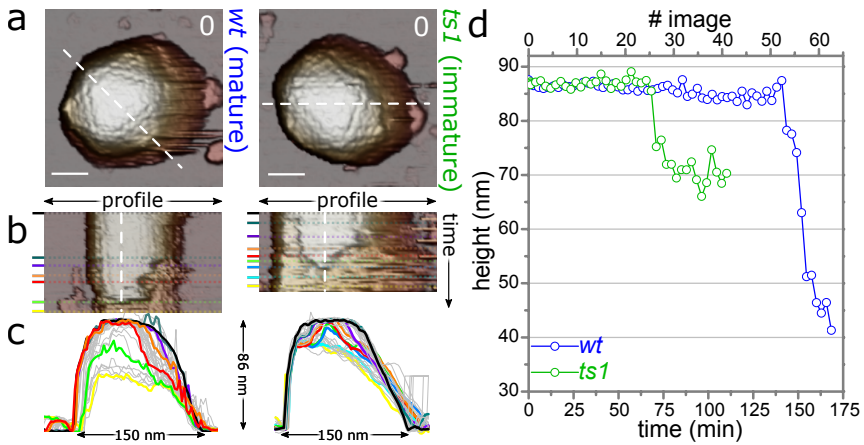

Figure 4.6: Height evolution study. (a) The white dashed lines in frames #0 of *wt* and *ts1* from figure 4.5, indicate the profile along all frames used to generate the kymographs in (b). (c) Profiles obtained from (b) show the shape evolution of the viral particles. Colored curves denote profiles corresponding to same colored profiles in (b). The remaining profiles are depicted in grey. (d) Evolution of the maximum height of the *wt* and *ts1* particles along time, obtained at the dashed vertical white profiles in (b). Scale bars in (a) correspond to 46 and 40 nm for *wt* and *ts1*, respectively.

The height of the *wild-type* particle decreases from 86 nm (frame 0, black profile) to 35 nm (frame 61, yellow profile). In fact, profiles purple (frame 28), orange (frame 38) and red (frame 42) reveal that the height remains unchanged at the locations where the shell appears intact, while at the broken parts the AFM tip reaches deeper and

deeper, releasing the core components as soon as the protein cage is broken. This observation is further supported by the evolution of particle height along time (figure 4.6 (d), blue) provided by the vertical white single point profile (profile of one pixel width) on the kymograph: up to frame 51, the height remains almost constant; but it decreases sharply by ∼45 nm in only 6 images, indicating that the virion contents are quickly released concurrently with the crumbling of the virus shell. Figure 4.7 (a) shows the typical topography of a mature particle after complete disassembly, demonstrating that the virus has been disrupted in two major pieces of about 30 nm in diameter. In addition, there are smaller objects (∼100) whose height (∼11 nm, figure 4.7 (c)) is compatible with those of individual hexons.[122,153]

The consecutive profiles close to the edge of the icosahedral facet (where the significant events happen, *e. g.* the capsid crack) of the *ts1* particle (figure 4.6 (a)), reveal that the void areas generated from the penton vacancy keep growing, but before long their depth stops increasing (dark blue and cyan profiles in figure 4.6 (c)). The plot showing height evolution along the white dashed single point profile line in the kymograph (figure 4.6 (d), green), indicates that it remains constant until frame 23, when it undergoes a sharp decrease of ∼16 nm. Afterwards the height remains constant at 70 nm, revealing a stable structure after the virus shell has been removed. The final topography of an immature particle after disassembly by material fatigue (figure 4.7 (b)) shows a mostly intact core of 70 nm in height plus numerous surrounding hexons (figure 4.7 (c))).

The average height for all *wt* virions, measured with an influence radius profile (profile of an average of several pixels in width - we used 3 or 4 points in radius) on the kymopgrah, remains constant until it quickly drops to highly disperse final values (figure 4.8 (a)). Capsomer assembly and disassembly follow kinetic models.[154] Since the average height measures capsid integrity, it allows to study the mechanical disassembly kinetics of the viral particle. The average height along time can be fitted to a Hill sigmoid function

$$h(t) = h_0 + (h_f - h_0)\frac{t^n}{\tau^n + t^n} \tag{4.1}$$

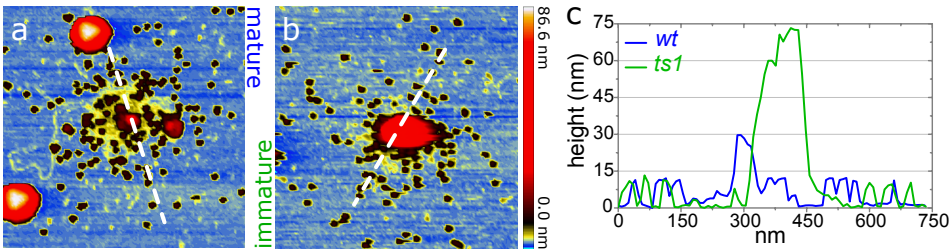

Figure 4.7: Final topography of adenovirus particles after material fatigue experiments. (a and b) Optimized color palette enhances substrate details in topographical images after fatigue assay for *wt* and *ts1* particle, respectively. (c) Profiles corresponding to the dashed lines in (a) and (b). AFM images are 1μm x 1μm.

where h_0, h_f, τ and n are the initial and final heights, inflection point, and cooperative factor, respectively. The *wt* mean cooperative factor for average height decrease (figure 4.8 (a)) is n$\sim$77 (table 4.1 at the end of the chapter). Conversely, the average heights of *ts1* particles (figure 4.8 (b)) present a gentler decrease, reflected by a lower cooperative factor n$\sim$13 (table 4.1). The single point height profiles of *ts1* particles (inset chart in figure 4.8 (b)) undergo an abrupt decrease of about 16 nm, reaching a stable value at $\sim$70 nm (cartoon in figure 4.8 (b)). This value corresponds to the addition of the height of the condensed core and the capsid wall resting on the substrate.

4.3.2 Penton loss study

Material fatigue assays provide novel quantitative information on single virus particle disruption, such as the dynamics of penton release. Since particles are oriented on the 3-fold symmetry, we consider the fate of the three pentons visible for each particle, although tilting occasionally enables imaging of lateral pentons. We compared profiles from a dilated image of a pentonless adenovirus EM reconstruction with an AFM image to ensure that the vacancies observed in the topographical image corresponded to missing pentons. Figure 4.9 shows that both approximations are in good agreement.

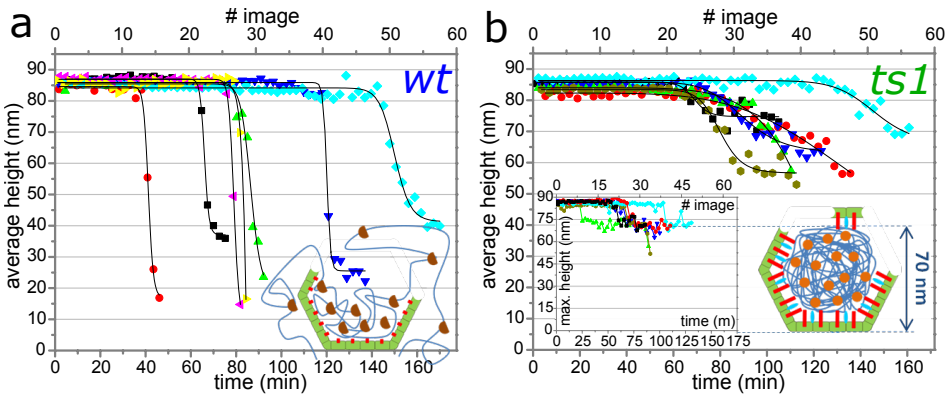

Figure 4.8: Height evolution along time of adenovirus particles subjected to material fatigue disassembly. Evolution of the average height of 7 *wt* (a) and 6 *ts1* (b) particles along time. Solid curves are the sigmoidal fits of the data. The inset chart in (b) depicts the maximum height evolution along time for *ts1*. Inset cartoons show models of particle dismantling.

4.3.2.1 Penton release

Table 4.2 presents the scan number where penton vacancies appeared during the experiment. To proceed with the study, all pentons are considered independent. In figure 4.10, the normalized penton population is plotted along the number of images. At the beginning, there are no penton vacancies. At different times of AFM scans, pentons are released so the penton population in viral particles decreases until the very last observed penton vacancy. The monotonic decrease of the data follow an exponential decay: $N(t) = N_0 \cdot e^{-\lambda \cdot t}$, where N_0 is the initial penton population, and λ is the penton release constant, *i. e.* the probability of penton release in one image. The mean lifetime $(1/\lambda)$ of a penton is $\sim$9 and $\sim$17 images for *wt* and *ts1* particles, respectively. The initial penton release rate $(N_0 \cdot \lambda)$ is $\sim$4 pentons per frame for *wt* and $\sim$2 pentons per frame for *ts1*, and decreases as $N(t) \cdot \lambda$. The probability to release a penton in one scan for *wt* is 1.85 times higher than for *ts1* ($\lambda_{wt} \simeq 11\%$ and $\lambda_{ts1} \simeq 6\%$).

The time lag between penton loss and final dismantling, defined by

the frame when blurring of the icosahedral contour occurs (demolished, table 4.2), can be also computed. On average, *wt* particles kept their gross pentonless organization during $62 \pm 7\%$ of the total experiment, while pentonless *ts1* virions endure for $43 \pm 9\%$ of this time (table 4.3).

4.3.2.2 Estimation of penton release energy

Jumping Mode Plus AFM applies forces which deform the viral capsid at each point. These deformations involve a supply in elastic and plastic energy deformation. To compute the energy supplied to the

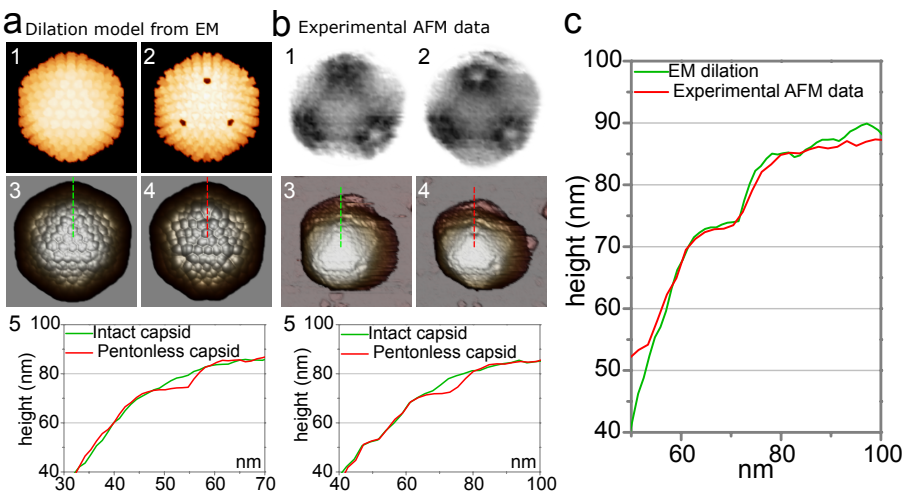

Figure 4.9: Penton release. (a) Adenovirus EM reconstructions before (a1) and after (a2) penton removal and dilation simulations performed on models (a3 and a4, respectively) by considering a 12 nm diameter tip. (a5) Comparison of profiles at the penton region (dashed lines). Figures (b3) and (b4) show the experimental AFM data, which are high-pass filtered in (b1) and (b2), respectively, to enhance penton vacancies. The profiles along the dashed lines are depicted in (b5). (c) Profiles demonstrate an excellent agreement between the model and the experimental data of the penton vacancies, which confirms that the vacancy in AFM images corresponds to a missing penton.

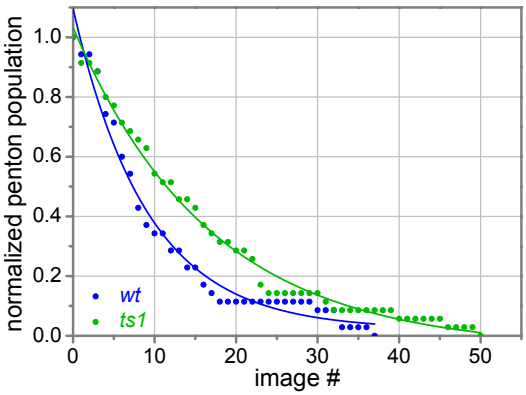

Figure 4.10: Penton release distribution. Penton population follows an exponential decay for both types of particles (*wt* in blue and *ts1* in green). Data normalized to the initial population (35 pentons for each type of particle, table 4.2).

particle for removing a penton, we assumed the maximum imaging force (100 pN) for all the points of the virus surface, and the whole capsid was considered to have the same elastic response. The total energy provided to the virus during the forward cycle of a force-curve performed at a pixel in JM+ is the enclosed area between the indentation curve and the x axis (figure 4.11 (a)). By using the spring constants of 0.38 N/m and 0.46 N/m for immature and mature virions, respectively (section 3.3.2), the supplied energy per pixel is about 3.2 k_BT for immature and 2.6 k_BT for mature. These values are likely overestimated, because part of the energy delivered by the forward curve can be given back due to the elastic response of the viral capsid, among other energy dissipation processes within the virus structure.

Still, for the sake of comparison between mature and immature particles, the energy provided to a virus particle while acquiring an image of 128x128 points can be estimated by taking into account all pixels, *i. e.* the force-distance curves, within the area delimited by the perimeter of the virus (figure 4.11 (b and c)). The total energy is computed by multiplying the energy provided in one image by the number of images preceding the penton release. The energy required to cause penton release of *wt* and *ts1* adenovirus is obtained by averaging the energies consecutively provided to create each penton vacancy of the triangular facet facing the tip. From this approximation, the average energy applied to generate one penton vacancy is $\sim 1.9 \cdot 10^{-16}$ calories for *ts1* and $\sim 1.0 \cdot 10^{-16}$ calories for *wt* (horizontal dashed

lines in figure 4.11 (d)), indicating that pentons in *ts1* are more stable than in *wt*. The corresponding values for a penton release in k_BT are $\sim 1.9 \cdot 10^5$ and $\sim 1.0 \cdot 10^5$ for *ts1* and *wt*, respectively. These values are larger than the ones computed for hexons indicated in the upcoming section 5.7, which shows that they are overestimated since hexon release energy should be higher.

To compare with values obtained from a bulk technique, the energy required to cause the first disassembly events in *wt* or *ts1* capsids was estimated from the enthalpy corresponding to the first thermal transition in differential scanning calorimetry curves obtained by Dr. Pérez-Berná.[57] The energy cost of the initial disassembly events (that most likely correspond to release of one or several pentons) is $6.0 \cdot 10^{-17}$ cal/virion for *ts1* and $3.4 \cdot 10^{-17}$ cal/virion for *wt*. The energy ratio *ts1*/*wt* from our single virion experiments is 1.9, in good agreement with the bulk calorimetric results (1.8). Both indicate that *ts1* pentons are more stable than *wt* ones.

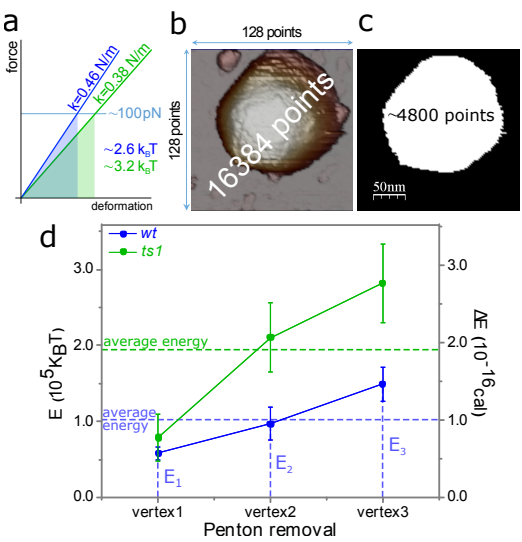

Figure 4.11: Estimation of penton release energy. (a) Scheme showing the estimation of supplied energy for the scanning force in one point for *wt* (blue) and *ts1* (green) viruses. (b) Number of points in an AFM image. (c) Number of points within the virus perimeter, *i. e.* number of force-distance curves. (d) Supplied energies for each penton release event averaged to all *ts1* and *wt* virions vacancy occurrences, indicated as E1, E2 and E3 for *wt*. Dashed lines represent the average of these three energy values.

The possible origin of the stabilization of pentons in the immature virus is twofold. First, structural studies have shown that the pres-

ence of precursor proteins results in extra interactions joining hexons (not pentons) to the core.[26,54,57] Second, processing by the viral protease induces core decompaction accompanied by an increase in capsid stiffness (section 3.3.2), suggesting that maturation could increase the internal pressure in the virion (chapter 5).[57,65,136] Both aspects may contribute to change the built-in mechanical stress at the vertices[155] in the mature adenovirus virion that would result in more unstable pentons.

4.3.3 Breakage pattern

The viral capsid breakage maps due to the force curves fail to discern differences in the behavior of capsid uncoating between *wt* and *ts1* (section 4.2). In section 4.3.1, viral particles show different topographical characteristics (*e. g.* penton loss, capsid crumbling or cracks) along the capsid disruption process. To explore the capsid rupture pattern that records these breaking characteristics for each particle, we calculated time cumulative disruption maps (TCDMs) depicting the sequence in which different shell areas were lost (figures 4.12 to 4.14).

For each virus, TCDMs are constructed by subtracting each movie frame from the initial one (figure 4.12). To highlight the lost shell area in each image, the difference maps are binarized by setting a gray level of 1 within the removed material zone and 0 elsewhere. All the disruption maps for one individual virion are added to obtain an image in which the grayscale levels indicate the sequence in which different areas of the shell were removed. Darker grey levels indicate regions in the shell that were removed earlier during the experiment. For instance, TCDMs show virus vertices as black areas because pentons are released first as described in section 4.3.1.

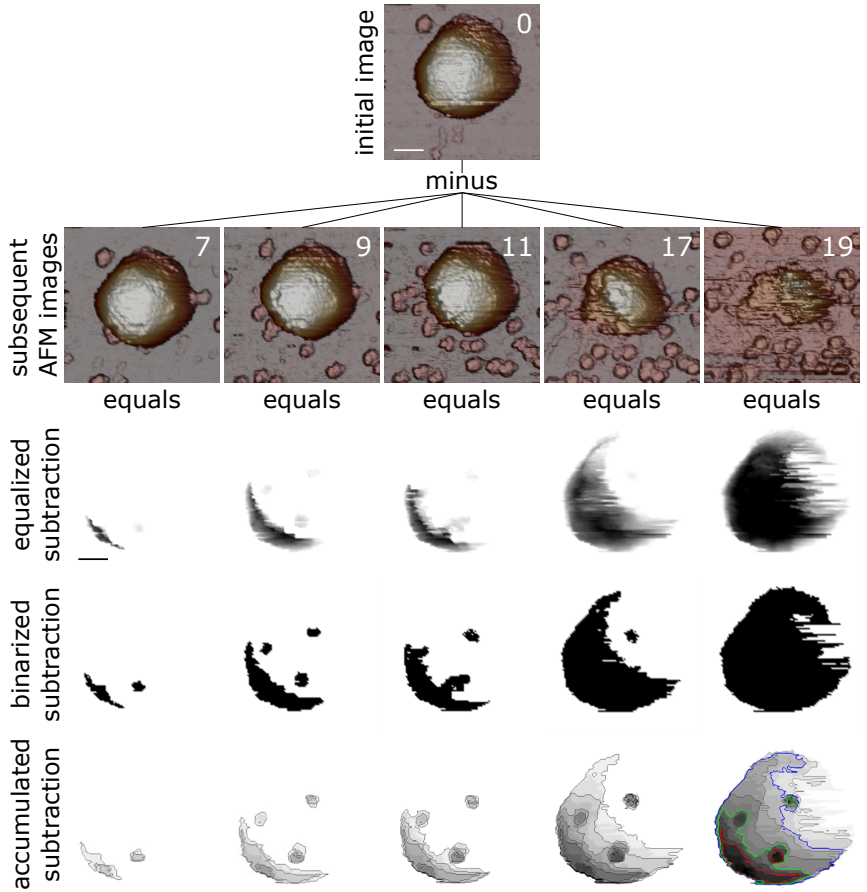

Figure 4.12: Procedure to obtain the time cumulative disruption maps (TCDMs). First, all AFM images for a single particle are aligned. Then, we compute the subtraction of each image from the first one (similar to figure 4.1 (d), left). Then the breakage is delimited by applying an accurate flooding that defines the breakage perimeter (equalized subtraction). The breakage region is binarized. The cumulative maps are computed by adding the binarized subtraction maps. The scale bars are 60 and 48 nm for the AFM topographies and subtraction images, respectively.

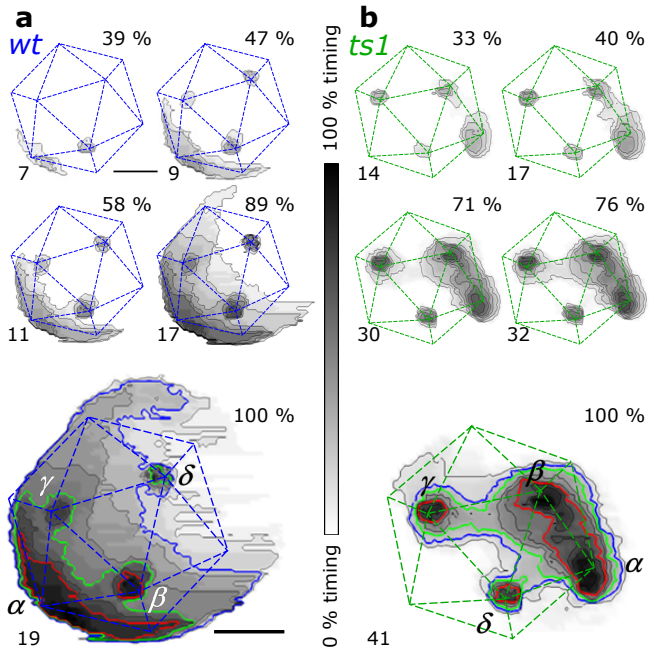

Figure 4.13: Examples of time cumulative disruption maps (TCDMs). Disruption maps for one *wt* (a) and one *ts1* (b) particles. The elapsed time in minutes corresponding to the whole grayscale is 50 min in (a) and 118 min in (b). The scale bar corresponds to 48 and 40 nm for (a) and (b), respectively. Red contour plots indicate areas removed early (32% and 43% of the elapsed time for (a) and (b), respectively). Green contour plots indicate areas removed at medium times (55% in (a), 74% of the elapsed time in (b)). Blue contour plots indicate areas removed late (84% and 83% of the elapsed time). The *ts1* particle of (b) is the one studied in figure 4.5 (b). See also *Movie_5_SciRep* for (a) and *Movie_3_SciRep* for (b).

4.3.3.1 *Wild-type* particle

In the mature virion in figure 4.13 (a), the penton vacancy created at the position denoted as α induces earlier material elimination than vacancies β, γ and δ (red contour line -CL- of figure 4.13 (a)), and grows in an irregular disassembly front that reaches vertices β and γ (green CL). This crumbling spreads upwards, eventually reaching vacancy

δ (blue CL, figure 4.13 (a) and *Movie_5_SciRep*). Figure 4.14 (a-c) depicts more examples with similar evolution in breakage patterns.

4.3.3.2 *ts1* particle

In the TCDM series for the immature particle in figure 4.13 (b), the initial CLs surrounding vertices α and β show simultaneous and independent growth spread, eventually merging into a continuous crack (red CL in figure 4.13 (b)). Each lost vertex acts as a seed developing cracks that eventually merge with those of the neighboring vertices (γ and δ, green and blue CLs in figure 4.13 (b), *Movie_3_SciRep*). Figure 4.14 (d-f) depicts more examples with similar evolution in breakage patterns.

4.3.4 Biological context

Mechanical fatigue induces stepwise dismantling of adenovirus capsids, replicating the *in vivo* disassembly process[38] and showing differences in the disassembly pathway for mature and immature virions that reflect their infectious phenotype. Disruption due to mechanical fatigue starts with pentons dissociating, as previously observed in response to thermal or chemical disruption[57] and during natural disassembly at the beginning of the infectious cycle. However, real time monitoring shows that pentons are sequentially removed, an aspect that could not be elucidated with the techniques previously used.[57] In principle, the structure of pentons and peripentonal proteins should be identical for all the vertices, and should be equally affected by mechanical fatigue. As a consequence, they should pop off after receiving the same loading cycles. The sequential removal of pentons may indicate either uncontrolled processes of energy dissipation in the virion or subtle differences on vertex structure.

After sequential release of pentons, the capsid is peeled away to reveal the core, and finally the particle collapses. In the cell, adenovirus

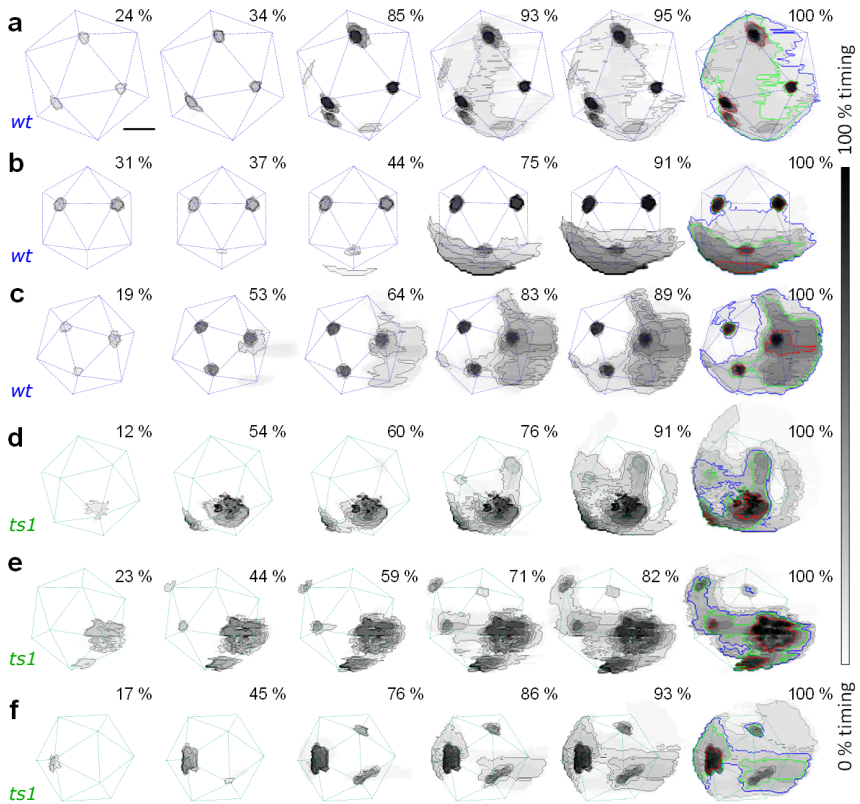

Figure 4.14: Other cases of time cumulative disruption maps (TCDMs). Examples of two-dimensional rupture maps for *wt* (a-c) and *ts1* (d-f) virions. The elapsed time in minutes corresponding to the whole grayscale for each image is 104 (a), 81 (b), 174(c), 104 (d), 90 (e), 92 (f), respectively. The scale bar corresponds to 45 nanometers in (a), 38 in (b), 46 in (c), 45 in (d), 49 in (e), and 50 in (f). Red contour plots indicate areas removed at 73% (a), 45% (b), 49% (c), 33% (d), 38% (e), 34% (f), of the total elapsed time, respectively. Green contour plots indicate areas removed at 90% (a), 75% (b), 75% (c), 73% (d), 65% (e), 79% (f), of the total elapsed time, respectively. Blue contour plots indicate areas removed at 96% (a), 94% (b), 92% (c), 80% (d), 73% (e), 93% (f), of the total elapsed time, respectively. The *wt* particle of (c) is the one studied in figure 4.5 (a) See also *Movie_2_SciRep*, *Movie_5_SciRep* and *Movie_4_SciRep* for (b), (c) and (f), respectively.

escapes the endosome at 15 min post infection (p.i.), and is found at the nuclear envelope at 45 min p.i., with complete disassembly occurring for the majority of particles at 60 min p.i. (figure 4.15).[38,50] Therefore, particles must remain reasonably intact in the cytosol after releasing pentons for at least 30-45 minutes. The results presented here indicate that *wt* particles keep their pentonless structure during $62 \pm 7\%$ of the disassembly elapsed time, which is similar to the *in vivo* period required for time traveling from endosome to the nuclear pore.

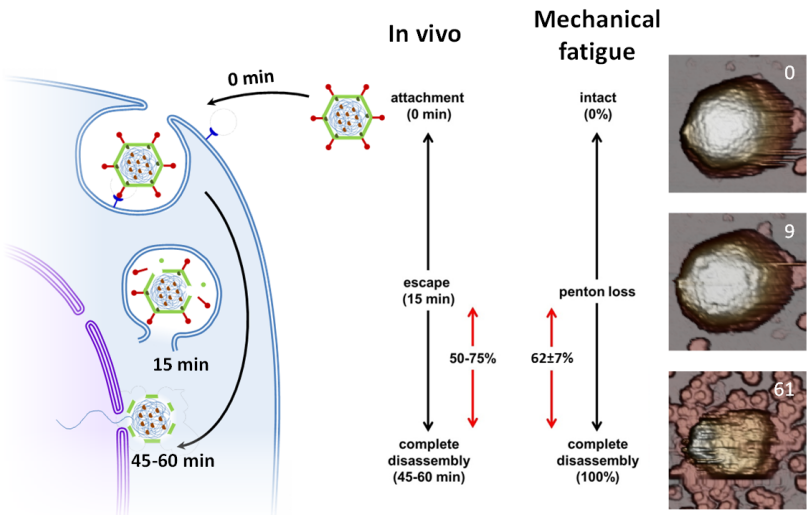

Figure 4.15: Mechanical disruption recapitulates the temporal pathway of adenovirus uncoating in the cell. Virions escape the endosome 15 min p.i. (post infection), having released some pentons. They reach the nuclear envelope 45 min p.i. and are completely dismantled by 60 min p.i. In mature virions, the partially disrupted structure persists for 50-75% of the disassembly elapsed time which can be compared to the $62 \pm 7\%$ due to mechanical fatigue disassembly.

TCDMs show that mature capsids unzip from a single fracture in the shell that starts at a penton vacancy and then spreads through the remaining shell in a highly cooperative way (figures 4.13 (a) and 4.14 (a-c)). Such crumbling is accompanied by simultaneous release of the material below the disappearing shell, reaching final heights well be-

low the core diameter (60 nm) for *wt* (figure 4.8 (a)).[26] Topographies after disassembly (figure 4.7 (a) and (c)) reveal three kinds of debris: first, large pieces of about 30 nm in height, corresponding to residual viral shell attached to the mica surface, along with core debris (red); second, tens of individual hexons dispersed around the disassembly area (black); third, partially compacted dsDNA (yellow) that homogeneously surrounds the central area of the core debris. These results imply that the DNA and proteins forming the core are not strongly held together, or attached to the capsid walls. This property would facilitate DNA diffusion outside of the viral cage prior to transport through the nuclear pore. This infection mechanism requires certain directionality in releasing the genome since DNA has to pass through the nuclear pore. In fact, TCDMs of mature virions show that crumbling starts from one of the created penton vacancies and advances across the capsid until its complete demolition without following any pattern otherwise related to the virus geometry. This effect may be caused by the DNA escaping from the initial crack, and helping to demolish the viral shell in a similar way as water enlarging an initially small crack of a dam wall.

Conversely, immature capsids endure shorter times after penton release ($43 \pm 9\%$ of the disruption time). Since *ts1* virions are less prone to release pentons, we infer that the energy provided by fatigue is used not only to remove vertex capsomers, but also to further weaken the rest of the viral shell. Penton vacancies in *ts1* seed the simultaneous formation of multiple cracks (figures 4.13 (b) and 4.14 (d-f)). These cracks spread and coalesce roughly following the icosahedron edges, while the DNA remains condensed in the core. Thus, the extra shell-core connections in *ts1* keep the hexons attached to the core and preclude the wall crumbling that occurs in mature virions. Topographies after disassembly show intact core (red) plus dispersed hexons (black), but not DNA debris (figure 4.7 (b) and (c)). The homogenous height decrease of 16 nm occurring in *ts1* particles corresponds to the capsid wall thickness, and all final *ts1* structures exhibit heights of about 70 nm (inset in figure 4.8 (b)), which most likely correspond to the remaining lower shell plus the intact core. These observations

suggest that the viral shell has been torn away, while the exposed core remains stable. Precursor proteins tightly condense DNA inside *ts1* particles and keep it attached to the capsid walls, preventing genome release when the virus cage is removed.[57]

4.4 Mechanical fatigue at different forces

Along the viral cycle, viruses face environments where they may undergo molecular impacts due to macromolecular crowding, which could be translated as random stress cycles.[156] Environments have heterogeneous macromolecular density, so the cycle load varies inducing variable fatigue cycles in virus particles. An approach to study the response of viral particles to these situations is to stress these protein cages under different load rates. This section shows how *wt* adenovirus particles behave under different values of stress below the breaking force of the capsid. To conduct the study of material fatigue of particles at different forces, data were analyzed as described in section 4.3.1.3.

4.4.1 Height evolution study

A MATLAB program was implemented to facilitate the height evolution study (appendix A.2). The output is the height of single and influence radius point at a selected spot of the capsid, and the number of cycles (pixels) in the virus area. Figure 4.16 (a) presents the average of four point influence radius of the maximum height evolution of 3-fold oriented *wt* adenovirus particles which disassemble by mechanical fatigue at 100 pN (same data as section 4.3.1, 7 particles), 300 pN (6 particles), 500 pN (6 particles) and 700 pN (6 particles).

The height of all viral particles changes following a similar behavior for all studied forces. The height remains almost constant until a sharp decay to very low values appears. This drop in height corresponds to

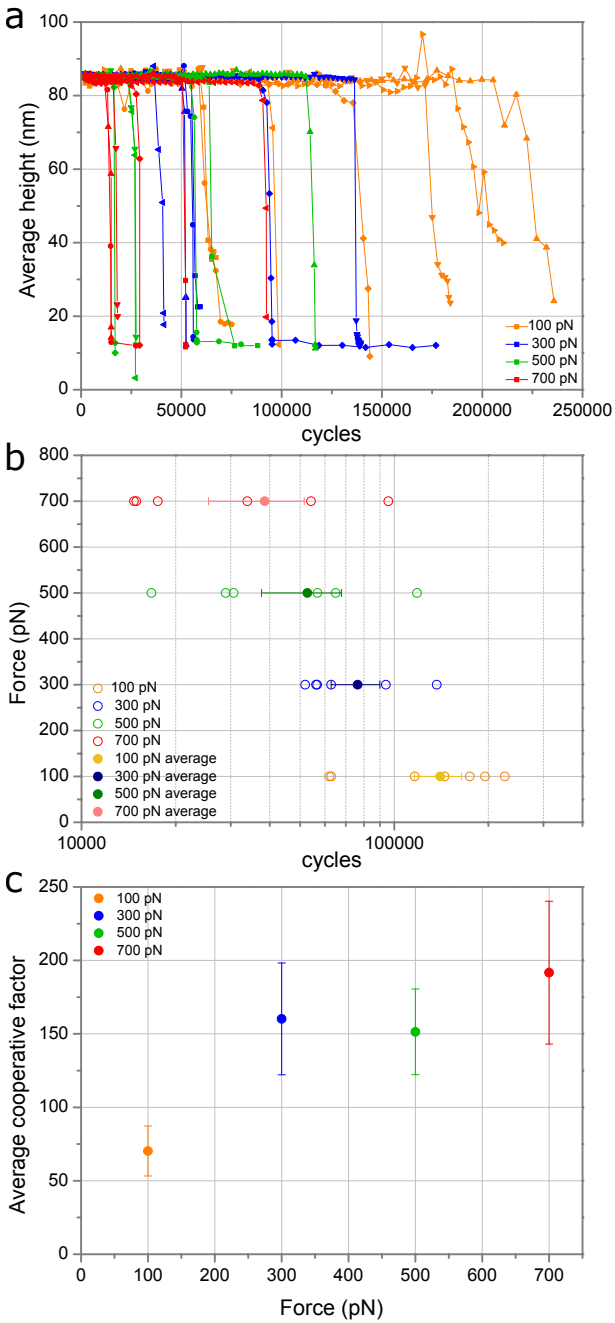

Figure 4.16: Effect of mechanical fatigue at different forces in *wt* adenovirus particles. (a) Average height evolution for each particle studied at different forces: 100 pN (orange), 300 pN (blue), 500 pN (green) and 700 pN (red). (b) Curve *S-N* for *wt* adenovirus (force *vs.* number of cycles). The x-axis represents the number of cycles on the viral particle until its disruption which is the inflection point of the sigmoid fit of the height evolution in (a) (logarithmic scale). Hollow points are the studied particles and the solid points are the average for each force. (c) Cooperative factor of the disassembly of viral walls at each force (equation 4.1).

the moment at which the top of the protein capsid is removed and, as described in section 4.3.1.3, the virus genome is quickly released since the AFM tip reaches deeper and deeper.

4.4.2 Stress-cycle diagram

In materials science, repeated application of cycling force leads to eventual disruption of the material because of fatigue. Mechanical fatigue studies have been largely carried out on macroscopic specimens of metals and polymers, among other materials. The failure of a specimen subjected to a cyclic load occurs by the growth along time of initial microscopic cracks until the total collapse of the sample that defines the fatigue lifetime or endurance. Experiments are conducted by a testing machine that applies a sinusoidal stress and counts the number of cycles to failure. Stress-cycle diagrams (Wöhler diagram or *S-N* curves) quantify the fatigue process and present the mean stress (S) of a constant cyclic stress amplitude versus number of cycles (N) to failure (figure 4.17).[157]

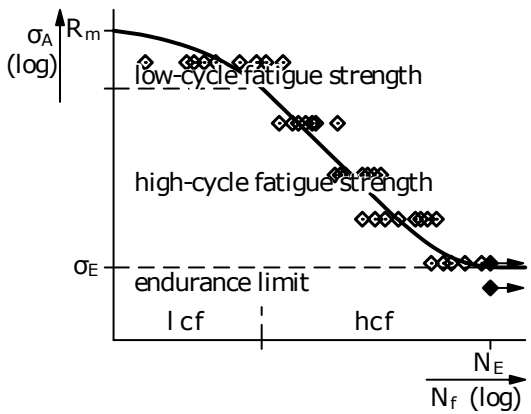

Figure 4.17: Example of an *S-N* diagram. Number of cycles to failure N_f is plotted versus the stress amplitude σ_A loaded cyclically with a fixed period. Adapted from *Mechanical Behaviour of Engineering Materials*.[157]

It is unclear how the concept of mechanical fatigue and its physical basis can be extrapolated to protein-based bionanomaterials such as viral capsids. Mechanical fatigue induced by Jumping Mode Plus AFM on viruses may be compared to the macroscopic fatigue assays, taking into account their nanometric scale, their material discretiza-

tion (capsomers) and the absence of covalent bonds between their building blocks.

Failure of the viral particles in these experiments is quite difficult to determine. For these fatigue studies, we consider that the height drop quantifies the disruption of the viral capsid. The parameter that gives the number of cycles until "viral capsid disruption" is the inflection point h_f of the Hill equation 4.1 (section 4.3.1.3). Figure 4.16 (b) shows the inflection point for all the *wt* particles studied at each force. The tendency of the data looks like the macroscopic *S-N* curves in material science (figure 4.17). The virus lifetime decreases as the applied force increases, which would be expected: the higher the forces the lower the endurance. This result is an approximation of a *S-N* curve of biological material at single particle level.

4.4.3 Force dependency of cooperativeness

Although it is a low sampling of data since in this kind of experiments viruses are not very stable (section 4.3) and even less at high forces, the average of the cooperative factor (Hill equation 4.1) shows a slight tendency to increase with the force (figure 4.16 (c)). The force that viruses withstand may act as a catalyst in the disassembly of the capsid, because it helps capsomers to overcome the energy barrier in the path from the bound to the unbound state. Thus the increase of applied force helps to demolish the protein cage faster, raising the probability to remove capsomers with missing neighbors once a first capsomer is lost (penton).

4.5 Future directions in mechanical fatigue for single molecule

Mechanical fatigue of viral particles with AFM has been described in some studies by performing force-distance curves but it has never

been quantified.[10,135] This chapter presents an approximation to fatigue quantification. The method presented is accurate enough to solve satisfactorily viral capsomer stability as the pentons (setcion 4.3.2) and capsid pathways disassembly (section 4.3.3) for viral particles with different cargos or under different conditions. This methodology is a good candidate to ascertain the open question of the role of pH in the weakening interaction of pentons in early endosomes in the firsts stages of the adenovirus infection pathway.[26,46,57]

Moreover, AFM mechanical fatigue assays take a long time to conclude a successful experiment. An alternative to study the fatigue endurance of a protein shell, that may lower the experimental miscarriage due to AFM scan and shorten the elapsed time of the experiment, would be to properly implement the force-clamp mode. This AFM option can apply controlled forces in two regimes: tension and compression.[128,158] Force-clamp assays could monitor capsid failure by applying different amplitudes of oscillation to the tip at a given mean force, which would be similar to the macroscopic material fatigue studies.[152] Experiments would be faster to conclude and may help to add more statistics to the results, at the expense of missing topographical dynamics.

4.6 Conclusions

Mechanical fatigue induced by AFM is a new experimental approach to cause single virus particle disruption while simultaneously monitoring the process. Fatigue disruption not only recapitulates the adenovirus disassembly pathway previously characterized by bulk or static imaging methods, but also enables a real time characterization of the intermediate dismantling stages of individual virions. Further, mechanical fatigue disassembly reflects the uncoating differences between mature and immature adenovirus particles, providing a new way to characterize the role of maturation as a determinant of viral infectivity. One remarkable observation of this chapter is that a source of stress so far

removed from the *in vivo* situation as mechanical fatigue results in the same disassembly pattern induced by cellular cues. It brings to mind the idea that the disassembly program of each virus is deeply embodied in its architecture to guarantee successful infection. A prediction following this consideration is that bacteriophage capsids subject to controlled mechanical fatigue would not fall apart, but rather release their contents while conserving most of their structural organization as they do in their natural environment. Disruption by mechanical fatigue may therefore shed new light on the disassembly pattern of viruses for which no *in vivo* information is available on that regard.

Tables

# particle	1	2	3	4	5	6	7	average
wt	68±4	38±4	38±5	150±16	48±8	70±4	127±61	**77**
ts1	22±9	5±1	7±1	10±1	17±3	17±4	--	**13**

Table 4.1: Cooperative factors. Average and statistical error of the mean (SEM) of the cooperative factors n of height decrease during disassembly.

Penton Vacancies									
Virion	Particle	Frame							
		Upright facet			Lateral			Demolished	Total
wt	1	10	14	18	8			27	30
	2	5	6	9	12			-	-
	3	4	7	9	4	4		20	22
	4	7	8	8	30	33		40	42
	5	1	3	14	1	33		46	51
	6	3	5	16	16			30	31
	7	4	6	12	17			32	33
	8	5	7	9	38			57	63
ts1	1	3	6	8	4	31		35	43
	2	5	9	16	4	10		34	38
	3	1	20	23	7			36	42
	4	1	22	23	15			-	52
	5	1	10	23	6	11		35	35
	6	4	13	16				30	36
	7	13	32	40	10	17	24	46	53
	8	18	46	50				-	-

Table 4.2: Penton vacancies. Frames in which appearance of penton vacancies was observed, used for penton population shown in figure 4.10. Data pertain to more particles than those included in figure 4.8 (a) and (c) because some viruses detached from the surface just after losing their pentons.

# particle	1	2	3	4	5	6	7	average	SEM
wt	33	55	80	70	47	62	84	**62**	7
ts1	77	53	36	34	47	13	-	**43**	9

Table 4.3: Pentonless percentage of virus lifetime. Pentonless time expressed in % of the total disassembly time for each virion, computed from the last lost penton in the upright facet and the demolished frame (where the viral contour is blurred) of table 4.2.

Movies

***Movie_1_SciRep*, *Movie_2_SciRep* and *Movie_5_SciRep*: Mechanical fatigue disruption of three different *wild type* (mature) virus particles.** First, a three-dimensional rendered topography of the virus is shown. Afterwards, the same sequence is shown stopping at clue points of the disassembly (7 frames per second). Lastly, a video of time cumulative disruption maps in which the breakage dynamics can be seen is shown (∼5 frames per second). The time cumulative disruption maps (TCDMs) of figures 4.14 (c), (b) and 4.13 (a) are obtained at the end of the movies, respectively. The movies are available in the supplementary information of Ortega-Esteban *et. al*, 2013: http://www.nature.com/articles/srep01434 as *srep01434-s2.mov*, *srep01434-s3.mov* and *srep01434-s6.mov*, respectively.[159]

***Movie_3_SciRep* and *Movie_4_SciRep*: Mechanical fatigue of two different *ts1* (immature) virus particles.** First, a three-dimensional rendered topography of the virus is shown. Afterwards, the same sequence is shown stopping at clue points of the disassembly (7 frames per second). Lastly, a video of time cumulative disruption maps in which the breakage dynamics can be seen is shown (∼5 frames per second). The time cumulative disruption maps (TCDMs) of figures 4.13 (b) and 4.14 (f) are obtained at the end of the movies, respectively. The movies are available in the supplementary information of Ortega-Esteban *et. al*, 2013: http://www.nature.com/articles/srep01434 as *srep01434-s4.mov* and *srep01434-s5.mov*, respectively.[159]

Chapter 5

Mechanics of viral chromatin reveals the pressurization of human adenovirus

5.1 Introduction

Condensation of nucleic acids in biological systems reaches its maximal efficiency in viral capsids.[160] Bacteriophage and some eukaryotic viruses pack their protein-free dsDNA genomes in a spool-like architecture within the shell. The confined genome builds up an outwards pressure, which facilitates genome ejection for DNA translocation into the host.[65,136,161] Other dsDNA viruses pack their genome with the help of cellular histones which bend DNA strands into nucleosomes, in a similar way to eukaryotic chromatin.[162] As described in CHAPTER 1, human adenovirus condenses its dsDNA genome using positively charged, histone-like proteins of viral origin, forming a 50 MDa DNA-protein core.[19] The adenovirus "mini-chromosome" is a beaded structure formed by the 35 kbp dsDNA genome associated with core proteins VII (∼500 copies), V (∼150 copies) and Mu (μ)

(∼300 copies), in ∼230 nucleosome-like units per viral particle.[30–33]

The presence of uncleaved precursor proteins makes immature (*ts1*) adenovirus particles more stable than the mature ones (*wild-type*), impairing proper uncoating and aborting infection.[57,150,159] Core proteins VII and μ are among those cleaved ones during maturation.[163] Concomitant with this cleavages, the viral core decompacts, and penton release and genome detachment from the capsid shell are facilitated as described in chapter 4.[26,57,159] The reason why vertex proteins detach more easily from mature than immature particles is unclear, since no additional structural elements corresponding to the uncleaved capsid precursors were observed in direct interaction with pentons in *ts1* cryo-EM reconstructions.[26,54]

In this chapter we use the nano-dissection capabilities of the Atomic Force Microscope (AFM) to gain direct access to single adenovirus mini-chromosomes in mature and immature particles, and directly probe their mechanical properties. The interplay of core and capsid mechanics reveals that core decompaction occurring during maturation pressurizes adenovirus that might facilitate particle metastabilization for proper uncoating and infection.

5.2 Mechanics of intact adenovirus capsids

We investigated the mechanics of three kinds of adenovirus particles representing different assembly states: *ts1* (genome containing, immature), *wt* (genome containing, mature) and *FC31-L3* (empty). Particles attached to freshly cleaved mica substrates were scanned as previously described in section 3.2.3. Since the experiments require successive manipulation events of the same particle (section 5.3), we focused on those showing a 3-fold symmetry orientation, which maximizes their area of contact with the substrate and thus their stability.

The three types of particles are topographically similar, as ex-

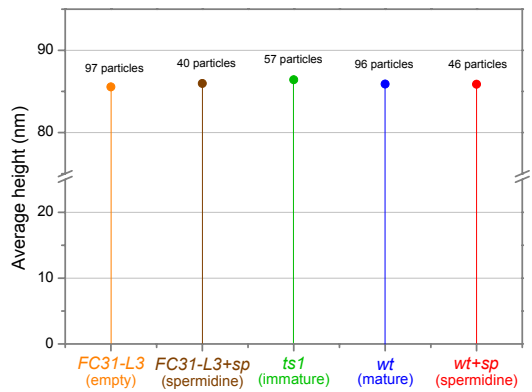

Figure 5.1: Particle heights. Average height of the particles studied in this chapter.

pected, presenting a height close to the nominal diameter (figure 5.1, and table 5.1 at the end of the chapter). The fact that empty particles show the same height as the full ones indicates that the adsorption forces are low enough to preserve their integrity. Once a virus particle was identified on the substrate, we conducted single indentation experiments to extract both its rigidity (spring constant) and breaking force as described in section 3.3.1. Nanoindentations performed on intact particles, without evident capsomer vacancies, provided the mechanical properties of capsids.

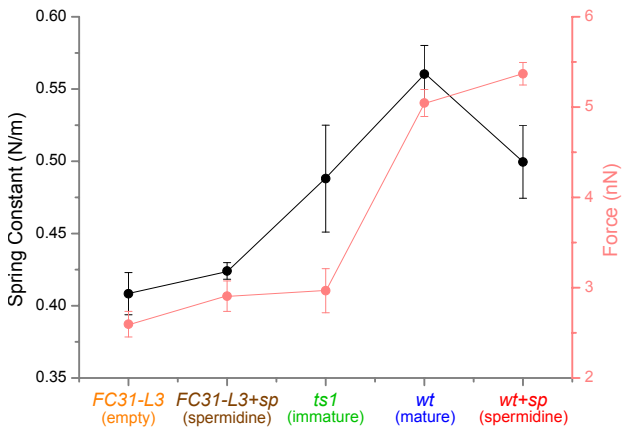

Figure 5.2: Mechanical properties of intact adenovirus particles. Black symbols and line represent the spring constant, and red symbols and line represent the breaking force, corresponding to the left and right axes, respectively.

Intact particles exhibit a linear behavior corresponding to a shell-

like deformation, until the elastic limit (breaking force) is reached.[62,107] We studied 77 *wt*, 20 *ts1*, and 61 *FC31-L3* particles. Analysis of the nanoindentations indicates that empty (*FC31-L3*) particles are the softest ($k_{FC31-L3}$ = 0.41±0.01 N/m, average±SEM), while *wt* particles are the stiffest (k_{wt} = 0.56±0.02 N/m) (figure 5.2 and table 5.2). Interestingly, *ts1* particles exhibit an intermediate value k_{ts1} = 0.49±0.04 N/m. Rupture forces reflect the same tendency, with 2.6±0.1 nN for *FC31-L3*, 2.9±0.2 nN for *ts1*, and 5.0±0.1 nN for *wt*. These results indicate that the presence of the genome and associated proteins increases the rigidity of the adenovirus particle, but the maximum stiffness is attained after proteolytic maturation.

We notice that the measurements presented here indicate a larger rigidity than the ones previously reported for both *wt* and *ts1* in section 3.3.2. This difference is due to the more stringent selection criteria used for the experiments in the present chapter, where we discarded particles suspect of being minimally disrupted before nanoindentation (see section 5.8).

5.3 Mechanics of adenovirus cores

To understand the effect of the core on adenovirus mechanics, we probe the mechanical properties of the core itself. We gently disrupt the capsid shell with nanoindentations to access the genome. An image was acquired immediately after each nanoindentation of every particle to monitor structural changes (figure 5.3). These images revealed that by keeping the maximum indentation of the AFM tip on the virus just below the breaking force, the protein cage lost some capsomers without collapsing. A few such deformations opened the particle and allowed direct access to the core. Subsequent nanoindentations performed on the opened particle exhibited non-linear deformations with a variety of discontinuities and steps, which might correspond to additional structural changes in the shell-core system. Figure 5.3 and sections 5.3.1, 5.3.2 and 5.3.3 describe representative examples of the

results obtained with this method for the studied particles.

5.3.1 Core of *wild-type* particle

The intact *wt* particle in figure 5.3 (a1) is indented for the first time (figure 5.3 (b), curve #1), resulting in minor damage (figure 5.3 (a2)) not large enough to allow entry of the tip into the core. However, indentation #3 (figure 5.3 (b), curve 3) generates a large crack, whose topographical profile (figure 5.3 (a4)) indicates that the AFM tip is accessing the core. Therefore, indentation #4 in figure 5.3 (b) performed at the crack observed in figure 5.3 (a4) is the first indentation directly reaching the core, presenting a non-linear deformation adjacent to the contact point. However, some of the successive indentations show linear regions which may indicate that the viral shell is the major subject of deformation (*e. g.* #6 and #7). This hypothesis was corroborated by performing the same experiment in empty capsids (section 5.3.3 and figure 5.3 (g) and (h)); thus, curves #6 and #7 are discarded for core analysis. Finally, curve #8 shows non-linearity as #4, and figure 5.3 (a9) demonstrates further particle deterioration where genome might be totally released. The last curve (#9) presents a linear behavior corresponding to the protein shell attached to the surface (similar to curves in section 5.3.3).

The core study of *wild-type* particle is not trivial. Given that DNA may be released along the study, we selected for the analysis the first curve that presented a clear non-linear behavior. In the example, we considered an early curve to ensure that the genome was not totally released. Moreover, a constraint of the model (section 5.3.4) used to obtain the core stiffness is to fit up to 10% of sample depth. As the curve #4 did not present any linearity corresponding to capsid in the deformation adjacent to the contact point, this indentation fulfilled the conditions for the analysis (table 5.3). Anyhow, an analysis for all curves that were considered indentations on core was also conducted showing similar results (table 5.4).

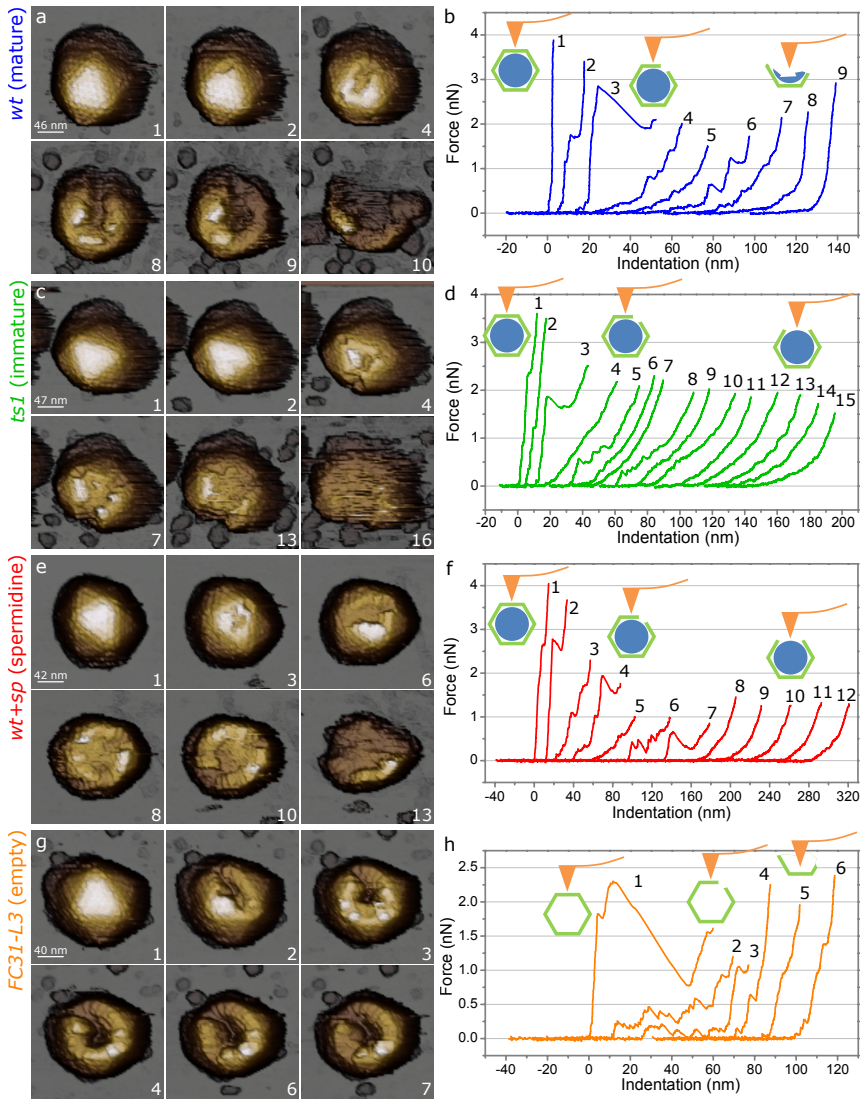

Figure 5.3: Gaining access to the core. (a) Topographical evolution of a *wt* particle with the indentation curves shown in (b). (c) Topographical evolution of a *ts1* particle with the indentation curves shown in (d). (e) Topographical evolution of a *wt* particle in the presence of 1 mM spermidine with the indentation curves shown in (f). (g) Topographical evolution of a *FC31-L3* particle with the indentation curves shown in (h). The numbers indicate the correspondence between each topography and its indentation. Indentation curves are horizontally shifted for the sake of clarity.

5.3.2 Core of *ts1* particle

Figure 5.3 (c) shows a similar experiment performed on a *ts1* particle. In this case indentation #3 creates a large crack and the successive curves present a non-linear dependence in contrast with the three initial curves (figure 5.3 (d)). Again, some of these curves present some linear deformation due to capsid influence (as section 5.3.3 shows for empty capsid), which are discarded for core analysis. Successive deformations also induce the progressive demolition of the particle. The last curves show non-linear behavior which means that the AFM tip is pushing on the viral core.

In this *ts1* example, curve #7 is considered the first indentation on core. Although curve #8 presents linear regions, the subsequent curves are totally non-linear because the core remains condensed despite the removal the top of the protein shell (as described in the fatigue experiments in chapter 4).

5.3.3 Probing the absence of core in *FC31-L3* particles

For a better understanding of the core behavior under nanoindentation on *wt* and *ts1* cores (sections 5.3.1 and 5.3.2), we performed the same experiments on empty capsids (figure 5.3 (g)). In the example, nanoindentations #1 to #3 remove capsomers of the facet of the icosahedral structure facing the AFM tip, which show linearities corresponding to deformation of the protein shell since there is no genome. The successive indentations, from curve #4 onward, are performed at the center of the crack. These indentations show deformation that correspond to the antipodal capsid region attached directly to the surface (inset sketch in figure 5.3 for last curves).

Thus, the linear or non-linear behaviors in the indentation curves are likely related to the contribution of each part of the viral particle constitution. Linear indentations indicate the viral shell is the major

responsible for deformation.[130] Some non-linear curves (curves #2-#6, figure 5.3 (b)) present a stepped shape linked to the uncontrolled deformation and/or breakage of unstable shell debris surrounding the crack. Finally, non-linear behavior reflects deformations of the viral core for filled particles.

5.3.4 Estimation of the Young's modulus for the adenovirus core

All the full particle specimens showed a linear response to the first few indentations until the protein cage was opened with a large disruption (curve #3 in figures 5.3 (b) and (d)). The response to most of the subsequent indentations was non-linear. Some monotonic indentations showed a hertzian-like nature[164] (curves in figure 5.3 (b8) and (d7)). These curves were obtained by indentations on cracks with a size similar to the diameter of the tip apex (∼30 nm). In this situation, the AFM tip directly probes the unshielded region of the core. Therefore, we can obtain mechanical information on the core by fitting these curves to a hertzian model.

To obtain the Young's modulus (E, the intrinsic stiffness of a material) of adenovirus cores we fitted the data to the model of thin layered samples presented by Dimitriadis *et al.*,[164] since indentation on viral cores are large and may have substrate influence. This model is based on the theory of Hertz contact mechanics between a sphere and a half-space,[165] where the indenting force (F) depends on the indentation (δ) like

$$F = \frac{4E}{3(1-\nu^2)} R^{1/2} \delta^{3/2} \tag{5.1}$$

where ν, R and E indicate the Poisson's ratio (transverse/axial deformation ratio), the indenter radius and the effective Young's modulus, respectively. The model has some terms that correct the substrate contribution to the deformation for thin layered samples as follows:

$$F = \frac{4E}{3(1-\nu^2)} R^{1/2} \delta^{3/2} [1 - \frac{2\alpha_0}{\pi}\chi + \frac{4\alpha_0^2}{\pi^2}\chi^2 -$$

$$-\frac{8}{\pi}^3\left(\alpha_0^3+\frac{4\pi^2}{15}\beta_0\right)\chi^3+\frac{16\alpha_0}{\pi}^4\left(\alpha_0^3+\frac{3\pi^2}{5}\beta_0\right)\chi^4] \tag{5.2}$$

where

$$\chi=\frac{\sqrt{R\delta}}{h}$$

and h indicates the height of the sample. Since the viral genome may be able to rearrange, we considered the case of not bonded substrate as the model admits. Therefore, the constants depending on the Poisson's ratio α_0 and β_0 are:

$$\alpha_0=-0.347\frac{3-2\nu}{1-\nu}$$

$$\beta_0=0.056\frac{5-2\nu}{1-\nu}$$

Since the indentation of the AFM tip in the core is better described by considering two spheres (tip and virus) instead of a sphere and a plane,[164] we considered a radius of R_{tip} ∼15 nm for the sphere of the tip (the nominal radius of the tip); and for the sphere of the core, we took the radius as half the height h of the viral core, measured at the nanoindentation point. Then, the effective radius R is $1/R = 1/R_{tip} + 1/(h/2)$. We assumed a Poisson's ratio of 0.2, similar to that previously reported for cellular chromosomes.[166] Morever, as we consider that the AFM tip does not deform (the Young's modulus is larger than the sample's, 280-290 GPa[167]), we can assume that the effective Young's modulus corresponds basically to the sample ($1/E = 1/E_{tip} + 1/E_{core} \approx 1/E_{core}$).

To estimate the value of E from the experimental force *vs.* distance curves, the Dimitriadis equation 5.2 was fitted to the data using a MATLAB program specifically written for this task (appendix A.3). Figure 5.4 presents a force curve on a *ts1* core and its fitting for either the Hertz contact mechanics model (red curve, equation 5.1)[165] or the corrected model (blue curve, equation 5.2).[164] A constraint of the corrected model is to fit up to 10% of the sample height from the contact point; we chose to fit a broader data range to let the fit converge after some iterations since contact point is not easy to

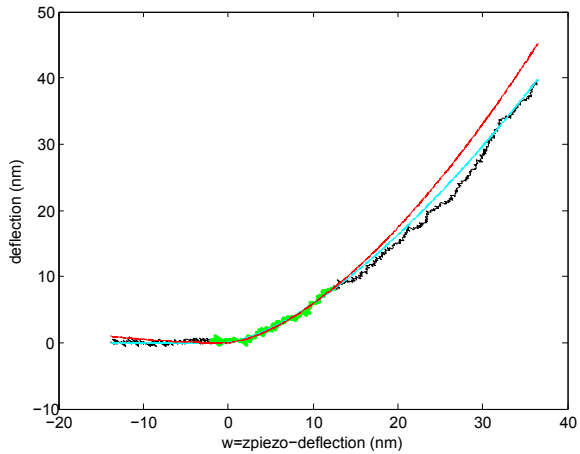

Figure 5.4: Fitting of the Hertz contact mechanics and Dimitriadis models onto the experimental force curve on a core. Example of fitting performed with the MATLAB program of a force distance curve on a *ts1* core. The x axis represents the indentation (subtraction of the piezo movement and the deflection of the cantilever) and the y axis represents the deflection of the cantilever as described in.[164] Experimental data for the fitting are presented in green, while the red and blue curves are the results of the fitting for the Hertz contact mechanics model[165] and the corrected model[164].

determine. The fits of both models are in good agreement with the experimental data, but the corrected model (blue) presents a lower growth rate compared to the classical model (red), resulting in a lower value of the elastic modulus (E). This is expected, since in this case the substrate contribution is excluded.

Figure 5.5 (a) shows curves for 8 *ts1* and 8 *wt* adenovirus particles that were considered to be the first directly performed on the core. Figure 5.5 (b) presents the results of the fitting of the corrected model for the Young's modulus to be E_{wt}=0.30±0.04 MPa (average±SEM) and E_{ts1}=1.2±0.1 MPa for the *wt* and *ts1* cores, respectively (table 5.3). To ensure that the fitting of the first indentation directly reaching the core is correct, we fitted all non-linear curves on cores showing that the average has the same tendency (table 5.4). However, since the genome may rearrange and be released, we conducted the rest of the

study taking into account only the first curve on the core. Also these Young's modulus values may not be quantitatively precise, but they are useful as relative mechanical parameters for the sake of comparison between the properties of the core in different stages of viral assembly.

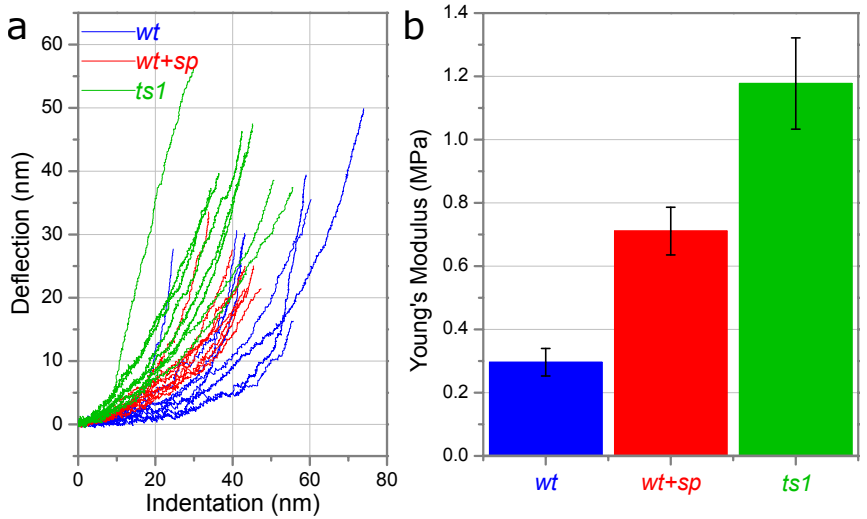

Figure 5.5: Estimation of the Young's modulus from first indentation on exposed cores. (a) FZ (force-distance) curves corresponding to indentations on the core of each type of particle. (b) Young's modulus values obtained from Dimitriadis' model, fitting the curves in (a).

5.4 Interplay between adenovirus shell and core mechanics

Virus studies at single particle level have elicited new biophysical discoveries on the interplay between structure and function.[10] In particular, it is generally accepted that genomes play an important role in modulating the mechanics of virus particles.[62,63,168–170] In herpesvirus and bacteriophages, cleavage of proteins and packaging of naked ds-DNA during maturation increases virion rigidity and stability.[66,171]

It is usually assumed that capsid and nucleic acid deformations behave as independent springs in parallel, so that the genome mechanical properties are estimated by directly subtracting the empty-shell spring-constant from that of the full-shell.

Our experiments provide a unique approach by studying both the combined and independent mechanics of a viral shell and its confined genome. Intact adenovirus full particles (*ts1* and *wt*) present higher spring constants and breaking forces than the empty ones (*FC31-L3*) (figure 5.2), revealing a mechanical reinforcement induced by the viral chromatin. The consideration of shell and core as two springs in parallel[65] would give a rigidity value for the *ts1* core k^c_{ts1}=k_{ts1}-$k_{FC31-L3}$=0.08 N/m. Likewise, the spring constant of the *wt* core could be obtained like k^c_{wt}=k_{wt}-$k_{FC31-L3}$=0.15 N/m. Thus, the mature viral chromatin would resemble a stiffer spring than the immature core when confined inside intact shells. However, the Young's modulus derived from our direct mechanical studies on cores accessed through cracks in open particles indicate the opposite situation, with $E_{wt} < E_{ts1}$. That is, although the presence of the genome induces particle stiffening as in other viruses, in adenovirus this stiffening becomes maximal in the mature particle, which however has a softer, less compact core than the immature one. The higher rigidity of the *wt* particle is not correlated with a higher rigidity of its core, but rather the opposite.

Understanding the physical nature of the virus core requires discerning how chromatin decondensation relates to mechanics.[172] We can consider the Young's modulus as a parameter for evaluating the compaction degree of the viral core. Thus in *ts1* (immature), the core is more rigid (more condensed) than in *wt* (mature), because $E_{ts1} > E_{wt}$. This is a direct observation of the decompaction transition undergone by the adenovirus mini-chromosome during maturation .[26,57] Another proof of the degree of condensation is the structural evolution of cores along the nanoindentations cycles. Successive topographical profiles show that the *wt* particles undergo a gradual loss of the core (figure 5.6 *wt*) after shell breakage, although the remaining shell wall survives for a while (figure 5.3 (a)). Assays on the empty capsid *FC31-*

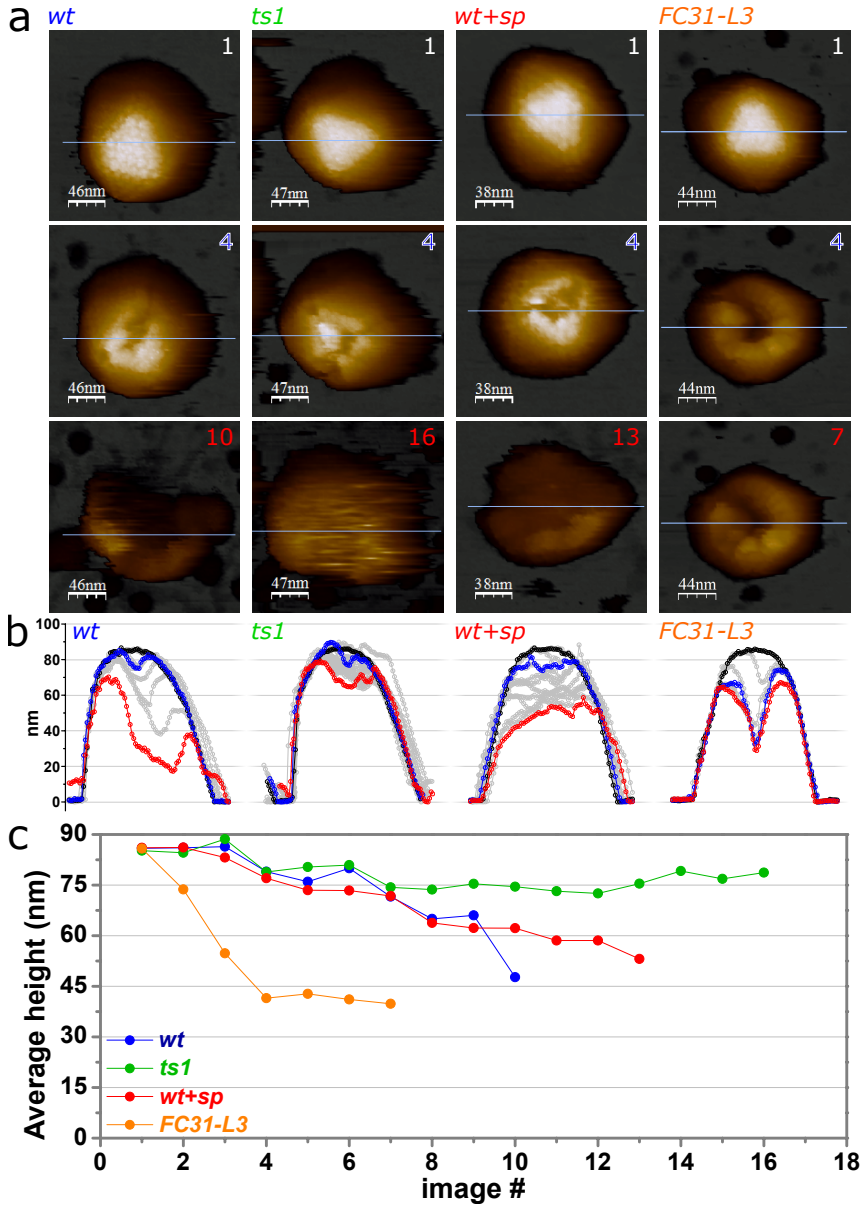

Figure 5.6: Topographical evolution of core release. (a) Topographical evolution of *wt* (left column), *ts1* (second column from the left), *wt* with spermidine (third column from the left) and *FC31-L3* (right column). (b) Height profiles obtained at the horizontal lines in (a). Black, blue and red colors correspond to the same code as the frame numbers indicated in (a). (c) Evolution of the average height at the center of the particles.

L3 support this gradual genome loss in *wt*, since the profiles show a drastic decay due to the absence genome when removing the top layer of the capsid (figure 5.6 *FC31-L3*). In contrast, in *ts1* particles (figure 5.3 (c)), successive indentations partially peel the viral shell away at the top, but the core (figure 5.6 *ts1*) does not experience the drastic loss of material shown by *wt*.[159]

Stiffening of virus particles associated with the presence of genetic material may have two different origins. On the one hand, structural changes in the shell provided by genome-capsid interaction can confer mechanical stiffening in a similar way that beams buttress the structure of a building, as previously demonstrated for the Minute Virus of Mice.[63] On the other hand, if the genome were confined at high pressure inside the capsid, it would generate an outwards force that could stiffen the shell. In viruses packing naked dsDNA, such as bacteriophage lambda or phi29, high pressures of ∼10s of atmospheres arise due to DNA bending and, mainly, to electrostatic repulsion between tightly packed dsDNA chains.[65,173] In adenovirus, the reversed mechanics of intact particles ($k_{wt} > k_{ts1}$) and exposed cores ($E_{wt} < E_{ts1}$), suggests the pressurization of virions during maturation.

5.5 Screening DNA-DNA electrostatic repulsion

To assess our pressurization hypothesis, we analyzed the mechanics of mature adenovirus in the presence of spermidine (sp) (figure 5.2, *wt+sp*). Spermidine is a trivalent polyamine commonly used to induce DNA condensates in solution[160] that also actuates inside DNA-full virus particles, eventually reducing their rigidity.[65,174] In these conditions, the spring constant of *wt* particles decreased from k_{wt}=0.56±0.02 N/m to k_{wt+sp} = 0.50±0.02 N/m for 1 mM of sp (table 5.2). Notably, the rigidity of *wt* particles in the presence of spermidine is very similar, within the error, to that of *ts1*. Probing the mechanics of *wt* adenovirus cores after opening the shell in the presence of

spermidine (figure 5.3) yielded a Young's modulus of 0.71±0.07 MPa for 8 particles (figure 5.5(b) and table 5.3), that is, above that of *wt* without spermidine but below that of *ts1*. This result indicates that spermidine induces stiffening and condensation in the mature core, which is, in turn, reflected in lower particle rigidity. As a control, we observed that the rigidity of empty *FC31-L3* shells did not change in the presence of spermidine (figure 5.2 and table 5.2).

Altogether, our data strongly suggest that core decompaction during maturation induces an internal pressure within the adenovirus particle. Moreover, the experiments in the presence of spermidine reveal that this internal pressure is at least in part due to the electrostatic repulsion between the negatively charged dsDNA strands. This is a somewhat unexpected result, because the adenovirus genome is heavily covered by positively charged proteins thought to screen most of the DNA charges to facilitate genome condensation.[31] Our results indicate that this screening is reduced upon maturation of core proteins VII and μ, possibly by changes in protein-DNA interactions occurring after cleavage by the viral protease.

Previous structural studies indicated that cores released from mildly disrupted, mature adenovirus particles contain polypeptides V, VII and μ and have a thick (15-30 nm) fibrous appearance.[33] Under more stringent conditions, μ is lost and essentially only polypeptide VII remains, forming a beaded structure with 9.5 nm beads interspersed on the dsDNA molecule at highly variable distances (10-130 nm).[32,33] Disrupted immature adenovirus particles, containing the precursor version of μ, released thicker fibers than the mature ones.[26] Architectural proteins involved in DNA condensation throughout nature have been categorized by their role as wrappers, benders, or bridgers.[175] A possible model to encompass all this information would have polypeptide VII acting as a wrapper in adenovirus genome condensation forming the nucleosome-like beads. The immature version of protein μ would act as a bridger keeping together two dsDNA chains to form the thick fiber, somehow compensating their mutual repulsion. This compensation would be lost by disruption of the bridging action of precursor μ upon its extensive cleavage by the viral protease[163] (figure 5.7).

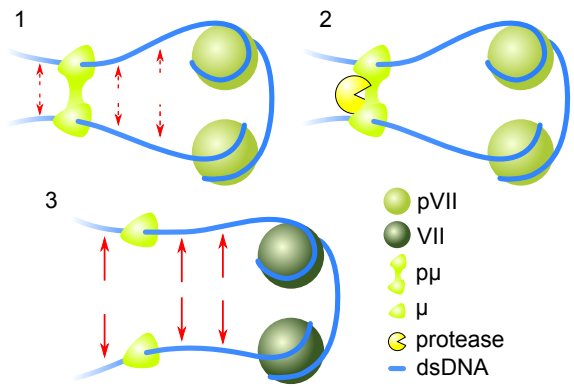

Figure 5.7: Cartoon of core decondensation model. Cartoon of the proposed model of core decondensation occurring during maturation. Dashed and full red arrows indicate different degrees of repulsion between adjacent regions of the dsDNA genome. See text for details.

5.6 Estimation of the adenovirus internal pressure

This section describes work by Dr. Reguera from Universitat de Barcelona aiming to estimate the pressure due to core maturation based on the data obtained in the AFM experiments. Three different models are used. Two of these models estimate the pressurization independently of its physical origin, while the last one takes into account the nature of the core.

5.6.1 Pressure estimation using Vella's formula

We can estimate the magnitude of the internal pressure in adenovirus, irrespective of its origin, using the continuous elasticity prediction for the elastic constant of a pressurized thin spherical shell indented by a point force:[176]

$$k_1 = \frac{\pi}{2} k_0 \frac{(\tau^2 - 1)^{\frac{1}{2}}}{arctanh\left[(1 - \tau^{-2})^{\frac{1}{2}}\right]} \tag{5.3}$$

Here $\tau = pR_1/k_0$ is a dimensionless parameter comparing the relative strength of pressure p against the elastic constant of the unpressurized shell k_0, and R_1 is the average radius of adenovirus (R_1=38 nm).

Taking k_0=k_{ts1}=0.49 N/m, and k_1=k_{wt}=0.56 N/m (table 5.2), and solving equation 5.3 for p, we obtain an estimate of 3±1 MPa (∼30 atmospheres) for the increase in internal pressure upon maturation.

5.6.2 Pressure estimation with Finite Elements analysis

Given the relatively large thickness of the adenovirus capsid wall (h=9.1 nm) and the finite radius of curvature of the AFM tip (R_{in}=15 nm), finite elements simulations were performed to corroborate the estimates of the pressure based on Vella's formula (equation 5.3). Finite elements (FE) simulations of the AFM indentation of adenovirus were performed using the program COMSOL Multiphysics 4.3 (Comsol, Stockholm, Sweden). The empty capsid of *wt* adenovirus was modeled as a thick spherical shell with an external radius R=40.2 nm and thickness h=9.1 nm (see inset of figure 5.8). The capsid wall was considered as made of a homogenous material with Young's modulus E and Poisson's ratio ν=0.3 (a typical value for protein-like materials).

This model capsid was placed on a hard flat substrate and indented by a hard spherical object with radius R_{in}=15 nm, mimicking the AFM tip. The system was simulated using a 2D axisymmetric model that was meshed with over 3300 triangular elements. The contacts between the shell and the tip as well as the supporting surface during indentation were implemented with a contact-penalty stiffness method according to the COMSOL manufacturer's manual. A parametric, non-linear solver was used to simulate the stepwise lowering of the tip onto the capsid. The spring constant was obtained from a linear fit of the force versus indentation, for small indentations between 3 and 4 nm.

Figure 5.8 shows the indentation curves obtained for the model of adenovirus capsid with a tip of R_{in}=15nm and a value of the Young's modulus E=0.28±0.02 GPa chosen to reproduce the experimental value of the *ts1* spring constant. The black line is the indentation

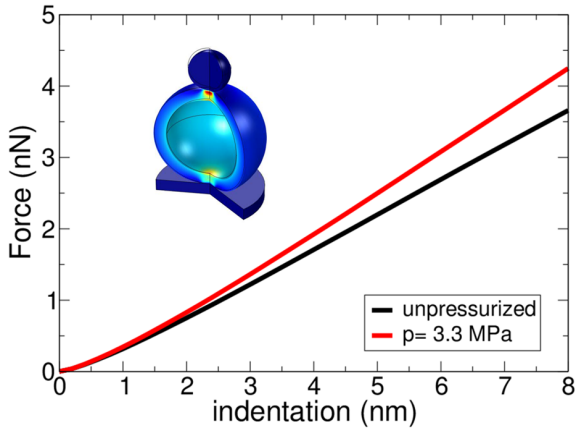

Figure 5.8: Force-indentation curves obtained from Finite Element simulations. The black line represents the values obtained for an unpressurized capsid, and the red line corresponds to the capsid with an internal pressure of 3.3 MPa. The inset figure shows the model used in the simulations, where adenovirus is represented as a spherical shell, indented on top of a hard substrate by a spherical tip.

curve for the unpressurized capsid, whereas the red line is the indentation curve when the virus has an internal pressure of 3.3 MPa, that yields a spring constant of k=0.56 N/m, identical to the experimental value measured for *wt*. Taking into account the experimental error bars (table 5.2), the estimate of the pressure in the FE simulations is 3.3±0.9 MPa (∼33 atmospheres), which is fully compatible with the value obtained from Vella's formula (equation 5.3).

5.6.3 Pressure estimation using polymer model

We also can rationalize the physical mechanism that builds up internal pressure in adenovirus as follows. The standard inverse spool models used so far to justify the origin of pressure in other dsDNA viruses[177,178] are not applicable in our case, because the adenovirus core is a mixture of dsDNA and proteins. Instead of an ordered spool, this viral chromatin can be better modeled as a linear unbranched polymer with a total length L=11.9 μm (corresponding to a not con-

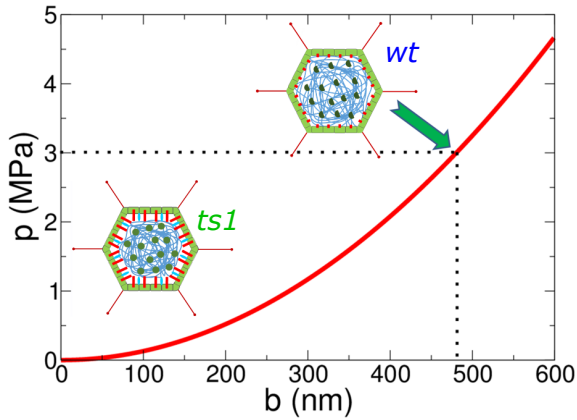

Figure 5.9: Entropic pressure of a confined globular polymer. Pressure generated by the confined adenovirus mini-chromosome, modeled as a compact polymer, as a function of its Kuhn length b. For wt, b=480±70 nm is required to reach 3±1 MPa of pressure. In the case of *ts1* or *wt* with spermidine, the mini-chromosome has a much shorter effective Kuhn length leading to a negligible pressure.

densed 35 kbp dsDNA molecule without proteins) and made by N segments of an effective Kuhn length b and a persistence length $b/2$. The Kuhn length defines also the effective radius of the viral chromatin R_g in terms of the usual scaling expression $R_g \sim bN^{\nu}$, where ν is a scaling exponent that characterizes its physical behavior. There are evidences, at least for human chromatin, suggesting that short lengths of chromatin behave as a compact or globular state polymer, characterized by a scaling exponent =1/3.[179,180] When this polymer is confined inside a sphere of radius R, its free energy is[181] $F \approx k_B T \left(\frac{R_g}{R}\right)^{\frac{1}{\nu}} = k_B T \frac{L}{b}\left(\frac{b}{R}\right)^{\frac{1}{\nu}}$, thus leading to an effective pressure

$$P = -\left.\frac{\partial F}{\partial V}\right|_T = \frac{k_B T}{4\pi R^3}\frac{1}{\nu}\frac{L}{b}\left(\frac{b}{R}\right)^{\frac{1}{\nu}} \tag{5.4}$$

As shown in figure 5.9, this entropic pressure generated by the confinement of the adenovirus chromatin can reach values of 3±1 MPa (∼30 atmospheres) for a Kuhn length b=480±70 nm. This value corresponds to an effective persistence length of 240±40 nm, similar to measurements reported for interphase chromatin in budding yeast.[182]

Furthermore, spermidine reduces the persistence length of dsDNA.[183] In the case of the *wt* particle with spermidine, a reduction of the persistence length to values below 100 nm (*i. e.* b =200 nm) would justify the almost complete elimination of the pressure.

5.7 Estimation of the adenovirus internal pressure from manipulation of hexons

Valuable information can be obtained from features in force curves on viral particles, or stress-strain curves in material science (*e. g.* stiffness and fracture from slope and the latest instability point, respectively). An important point is the yield strength that determines an irreversible change from the elastic to plastic regime where the deformation of the specimen becomes permanent. Some materials present a yield point followed by a regime where the strain grows without an increase in stress known as yield point elongation or yielding. Some force curves on adenovirus present a similar behavior where a step of a few nanometers extends without force variation. In this section we make a detailed study of this phenomenon which may help to compute an approximation of the pressurization of adenovirus.

We performed nanoindentation on viral particles below the breaking force to study the steps. The force curve in figure 5.10 (center) presents a hysteresis in the backward curve which means that an irreversible structural damage happened. The forward curve (green) shows a linear deformation until a step of 2-3 nm at a force of ∼2.5 nN appears, and then the force continues increasing linearly with the indentation. Then the backward curve (red) presents linear behavior matching the last region of the forward curve. The contact point (force 0 nN) of the backward curve shifted laterally. Afterwards, the topographical image reveals a vacant hexon (figure 5.10 right). Then, the steps in force curves can be related to missing hexons in the cap-

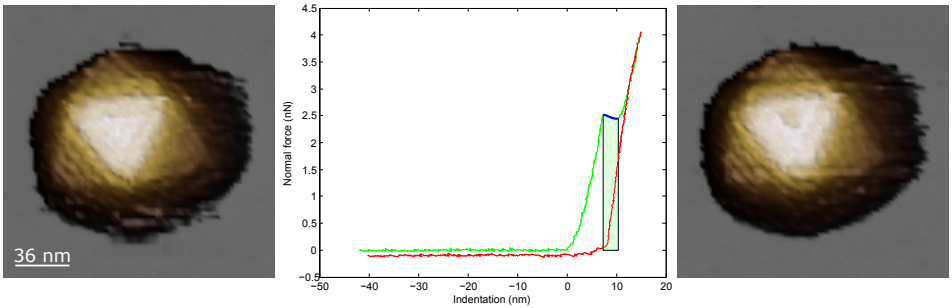

Figure 5.10: Generation of single hexon vacant with indentation assays. Topographical images before (left) and after (right) a nanoindentation (center) at the center of the facet demonstrate a hexon vacant. Forward and backward curves of the nanoindentation are depicted in green and red, respectively.

sid. Since the event occurs in the forward curve and the vacant hexon appears in the center of the triangular facet we could guess that the capsomer shifts inwards.

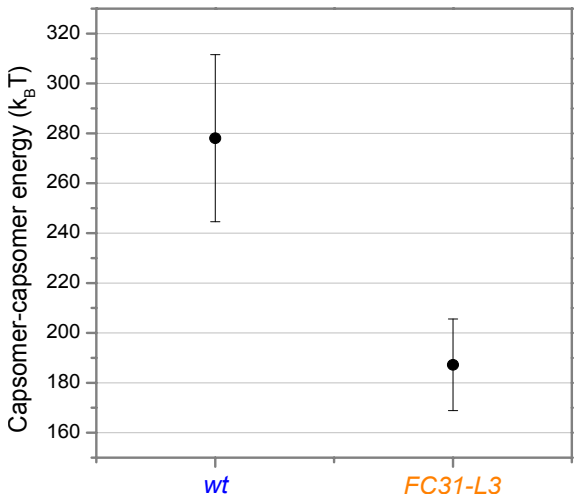

Figure 5.11: Capsomer-capsomer energy. The work required to move a hexon in the *wt* capsid is higher than in the empty capsid *FC31-L3* hexon. This higher cost could be related to the presence of the adenovirus core since the capsid structure is highly similar in both specimens.

In the force *vs.* indentation graph of figure 5.10, the area enclosed by the hysteresis cycle represents the work done by the AFM tip to displace the hexon; or ideally, the area under the yield point elongation (green shaded area below the step highlighted in blue of the forward curve). A MATLAB code was developed (appendix A.4) to compute

the spring constant of both linear regimes of the forward curve and the area under the step. We studied 15 *wt* and 9 empty (*FC31-L3*) capsids. Figure 5.11 shows that a higher work is required to shift a hexon in a *wt* particle than in an empty capsid (table 5.5).

The work required to move a hexon in an empty capsid is essentially the same as the energy needed to break the interactions between neighboring hexons. However in *wt*, the work required to move the hexon against the genome must also be considered. Taking into account that the structure of the capsid in both particles is identical, we can estimate the force that the genome is exerting against the capsid.

The work to remove a capsomer is $\sim 1.7 \cdot 10^3$ k_BT for *wt* and $\sim 1.1 \cdot 10^3$ k_BT for *FC31-L3*, converting it in Joules is $\sim 6.7 \cdot 10^{-18}$ J and $\sim 4.5 \cdot 10^{-18}$ J, respectively. The work is $W = Force \cdot displacement$ and for both particles the step is $\sim$ 2.5 nm, then the force that moves the capsomer is $\sim$ 2.8 nN and $\sim$ 1.8 nN for *wt* and empty capsid, respectively. The difference of the exerted force is $\sim$ 1.0 nN. Since the hexon diameter is 8.9 nm[153] (area$\sim$ 62.2 nm^2), we can compute that the pressure due to the presence of the viral chromatin is $\sim$160 atmospheres (table 5.6).

The pressure estimated from hexon displacements is much larger than the one estimated in section 5.6. In this calculation, we are assuming that only one hexon is pushed and the rest of capsomers remain immutable. But the AFM tip used for the experiments has a nominal radius of $\sim$15 nm, that at the indentation point where the step event happens (7.5$\pm$0.8 nm and 4.8$\pm$0.4 nm for *wt* and *FC31-L3*, respectively - average$\pm$SEM) reaches a contact area with a radius of $\sim$12 nm (contact radius using basic trigonometry: $R^2 = (R-d)^2 + a^2$ where R, d and a are the tip radius, the indentation and the contact radius, respectively; figure 5.12). This contact radius is larger than one capsomer (8.9nm in diameter), which means that more than one capsomer is involved in the deformation. Thus the estimation of the pressure with this method is not very accurate and would need of a refined model, or use a puncher with a size similar to the capsomer in the experiment.

Another reason for the difference in pressure estimation using hexon displacement data could be that the comparison in this section is between empty and *wt* particles, while section 5.6 compares *wt* and *ts1*. Future hexon displacements experiments should be carried out on *ts1* to complete this study.

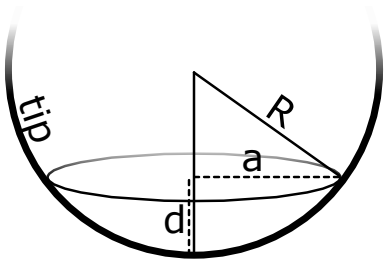

Figure 5.12: Scheme of simplified contact area in an indentation. Estimation of the contact area radius using basic trigonometry.

An additional piece of information provided by hexon displacement experiments is that the energy required to remove a hexon in an empty adenovirus particle is $\sim 1.1 \cdot 10^3$ k_BT. This value is lower than the one estimated from the mechanical fatigue assays for penton release in section 4.3.2.2 ($\sim 1.0 \cdot 10^5$ k_BT - *wt* penton), which is two orders of magnitude larger. Actually, the dissociation energy estimated by differential scanning calorimetry (DSC) is lower for pentons ($\sim 2.9 \cdot 10^3$ k_BT)[57] than for hexons, what make sense since pentons have five neighboring capsomers and hexons have six. Moreover, in an icosahedral structure, the capsomers that are under a higher stress are the ones situated in the vertices (pentons), lowering their dissociation energy barrier and making them more prone to be released.[155,184]

The method presented in this section provides better accuracy to compute the capsomer dissociation energy than the one presented in section 4.3.2.2, since it is a direct measurement of the work supplied to the viral capsid. In fact, the method presented in this section for single particle and bulk techniques (DSC) assess the same order of magnitude for capsomer dissociation energy.

5.8 Dependence of mechanical properties on the capsid integrity

The values of the mechanical properties presented in section 3.3.2 for the mature virus *wt* and the immature *ts1* are lower than the ones obtained in the work of this chapter (section 5.8), what seemed incongruous. During the progress of the new experiments, we noticed that in the preceding work there was a high population of *wt* particles with at least a missing vertex. In the new study, it was really important that viral particles were in perfect condition and kept all the pentons. Then, the purification was carefully carried out and the AFM sample storage at -20 °C did not last more than 3 weeks to ensure the sample preservation.[185]

It has been reported that the mechanical properties of pentonless particles are affected in comparison with intact virus.[66,186] In view of this observation, we hypothesized that mechanical properties of pentonless particles might be affected in comparison with intact virus. To assess this possibility, we heated at 40 °C for 5 minutes the new AFM sample of *wild-type* adenovirus diluted in the same buffer (HBS with $NiCl_2$ 5 mM) before the substrate incubation. Heating at 40 °C causes viral particles to lose at least a vertex.[57] It was necessary to add 10% glycerol to the buffer to avoid particle clusterization. Then we proceeded to wash the AFM sample with the same buffer solution without glycerol and acquire data. We discerned between *wt* particles that showed clearly at least a missing penton and intact viruses. The mechanical properties of heated intact *wt* particles showed a slight decrease which means that, although viruses looked untouched some not clearly disrupted particles leaked out in the statistics (figure 5.13 and table 5.7). Obvious pentonless particles showed a lowering in the mechanical parameters to levels of the values presented in the work of section 3.3.2.[57]

However, one can think that in this process of losing a vertex the viral genome might be released and this could be the cause of particle

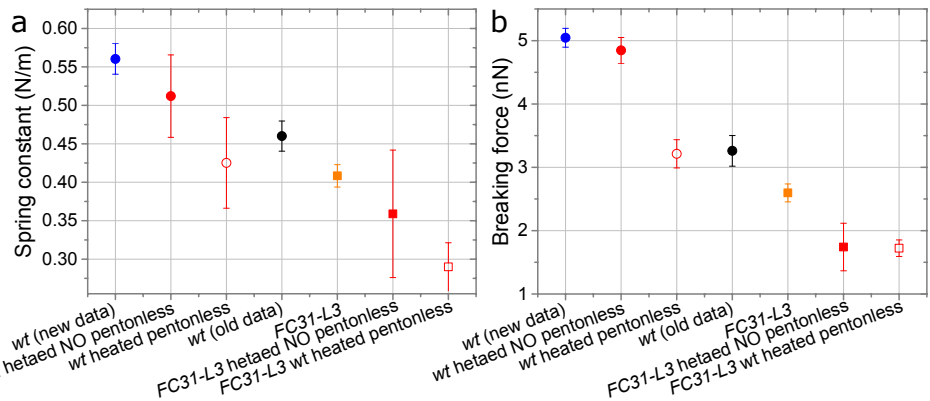

Figure 5.13: Stiffness variation of heated viruses. The rigidity of viral particles decreases due to penton loss. The *wt* and empty capsid decreases the same ratio when heated, what means that reduction is due to structural damage (pentonless) and not to genome release that may explain the difference in the average of data of *wt* virus in this section and section 3.3.2

softening. To assess this point, we repeated the same experiment for empty particles (*FC31-L3*) under the same conditions. We observed that *FC31-L3* was less thermo stable than full particles because there was a small population of intact particles. Moreover, figure 5.13 (a) shows that the stiffness presents a lower value than the non-heated particles but without reaching the pentonless value, and it also presents a larger dispersion (and table 5.7). It is also remarkable to mention that the breaking force presents a similar tendency to the stiffness (figure 5.13 (b)).

The ratio for stiffness (*wt* new purification)/(*wt* heated pentonless) is ∼1.3 and for (*FC31-L3*)/(*FC31-L3* heated pentonless) is ∼1.4, indicating that the decrease in stiffness is upon heating and releasing at least one penton is due to structural damage and not to genome release.

These observations suggest that one should not take the value of any property as an absolute value, but relative differences between different conditions is what counts. The ratio in stiffness for *wt*/*ts1*

values from table 3.2 is ∼1.2, and for the improved data is ∼1.1 (table 5.2 and section 5.8), which do not present a big change in the relative difference of the mechanical properties caused during maturation of adenovirus.

5.9 Conclusions

By opening mature and immature adenovirus cages we gained access to the viral chromatin and provided the first direct experimental analysis of the mechanics of a confined DNA-protein condensate. We found the mechanical signature of adenovirus core decompaction as a reduction of the Young's modulus during maturation. Contrariwise, mechanics of intact particles showed that mature particles are stiffer than the immature ones. Combination of these experimental observations with theoretical models substantiates that core decondensation during maturation pressurizes adenovirus. It is remarkable that the confined adenovirus genome, in spite of having part of its charges neutralized by proteins, still induces a significant internal pressure, that we estimate at ∼30 atmospheres considering that the confined viral chromatin behaves as a compact polymer with an effective persistence length of 240±40 nm. Uncleaved core proteins in the immature particle or spermidine in the mature virion act as DNA condensing agents, reducing its effective persistence length and concomitantly the pressure due to its confinement.

The pressure value estimated for adenovirus may be striking compared to viruses with portal reported in previous works, since the peculiarity of this virus is that some viral proteins condense the genome inside the capsid. Smith *et al.*[187] measured with optical tweezers the force that the DNA-packaging motor of bacteriophage ϕ29 applies up to 50 pN, estimating a pressure of 6MPa (∼60 atmospheres). Later, Hernando-Pérez *et al.*[65] verified with AFM that the pressurization of ϕ29 was ∼40 atmospheres, a work that inspired this chapter of this thesis. On the other hand, the presence of polyethylene glycol in so-

lution (PEG – a flexible and water-soluble polymer) creates very high osmotic pressures that in bulk experiments suppresses DNA ejection in bacteriophage λ estimating a internal pressure ∼20 atmospheres;[168] the same experiment for Herpes simplex virus type 1 (HSV-1) led to similar results (∼18 atmospheres), the first evidence of internal pressure in a eukaryotic virus.[161]

Tailed bacteriophage and herpesviruses use this internal pressure to start genome ejection through a portal system, leaving the intact shell behind.[161,188,189] Adenovirus capsids, on the other hand, can be partially disrupted without ejecting their genome, and do so only after complete disassembly.[57,159] Penton detachment during the first stages of adenovirus entry is crucial for initiating uncoating.[38,47,57] Structural studies have not revealed differences between the *wt* and *ts1* particles directly affecting penton capsomers.[26,54] However, it is clear that facilitating penton release under mild stressful conditions is one of the key effects of maturation.[57,159] We propose that pressurization induced by decompaction of the viral chromatin provides a biophysical destabilization of pentons in *wt* particles. Therefore, pressurization induced by maturation may facilitate the beginning of the stepwise disassembly in mature adenovirus, enabling its escape from the endosome for successful infection.

Tables

Particle	Average height (nm)	SEM (nm)	n
FC31-L3	85.5	0.1	97
FC31-L3+sp	85.97	0.08	40
ts1	86.4	0.2	57
wt	85.9	0.1	96
wt+sp	85.87	0.09	46

Table 5.1: Height of the viral particles. Average height and standard error of the mean of the particle heights. Neither the attachment surface, nor spermidine, nor viral core condition affect capsid main structure since the height is preserved within the error for all particles close to the nominal height (88 nm).

Particle	Spring constant (N/m)	n	SD (N/m)	SEM (N/m)	Force (nN)	n	SD (nN)	SEM (nN)
FC31-L3	0.41	61	0.11	0.01	2.6	51	1.0	0.1
FC31-L3+sp	0.424	32	0.032	0.006	2.9	32	0.9	0.2
ts1	0.49	20	0.16	0.04	3.0	20	1.1	0.2
wt	0.56	77	0.15	0.02	5.0	65	1.2	0.1
wt+sp	0.50	41	0.16	0.02	5.4	41	0.8	0.1

Table 5.2: Mechanical properties of viral particles. Table summing up the mechanical data, including rigidity and breaking force. The number of cases is higher in the stiffness than in the fracture strength analysis for *wt* and *FC31-L3* due to the inclusion of data from the hexon displacement study (section 5.7). Averages of the spring constant values and the breaking force obtained as described in section 3.3.2.

Particle	Hertz (MPa)	SEM (MPa)	Dimitriadis (MPa)	SEM (MPa)	n
ts1	1.3	0.1	1.2	0.1	8
wt	0.35	0.05	0.30	0.04	8
wt+sp	0.81	0.09	0.71	0.07	8

Table 5.3: Young's modulus estimated from the first FZ on cores. Table of the Young's modulus obtained from the first force curve (FZ) performed on viral cores for each type of particle studied. Average of 8 *wt*, 8 *ts1* and 8 *wt* with 1 mM spermidine particles for the classic theory of hertzian contact stress between two elastic spheres (Hertz) [165] and a model with corrections for thin samples (Dimitriadis) [164].

Particle	Hertz (MPa)	SEM (MPa)	Dimitriadis (MPa)	SEM (MPa)	n
ts1	1.8	0.3	1.6	0.3	47
wt	0.42	0.05	0.34	0.04	40
wt+sp	0.96	0.05	0.85	0.04	53

Table 5.4: Young's modulus estimated from all FZ on cores. Table of the Young's modulus obtained for all force curves (FZ) performed on viral cores for each type of particle studied. Average of 47 *wt*, 40 *ts1* and 53 *wt* with 1 mM spermidine particles for the classic theory of hertzian contact stress between two elastic spheres (Hertz) [165] and a model with corrections for thin samples (Dimitriadis) [164].

Particle	$Energy_{capsomer\text{-}capsomer}$ (k_BT)	SEM (k_BT)	n	Force (nN)	SEM (nN)	n	Step (nm)	SEM (nm)	n
FC31-L3	$1.9 \cdot 10^2$	$0.2 \cdot 10^2$	9	1.8	0.1	9	2.5	0.3	5
wt	$2.8 \cdot 10^2$	$0.3 \cdot 10^2$	15	3.1	0.2	15	2.4	0.3	13

Table 5.5: Data for hexon displacements. Results and standard error of mean obtained from the analysis of steps in force curves on *wt* and *FC31-L3* particles that resulted in hexon displacements. The table presents the energy to break interactions among one capsomer and a neighbor, the force at the event, and the length of the step. Some cases, where two displaced hexons were observed, have been used to compute the capsomer-capsomer energy taking into account the number of neighbors.

Particle	$Work_{hexon}$ (k_BT)	SEM (k_BT)	$Work_{hexon}$ (J)	SEM (J)	Step (nm)	SEM (nm)
FC31-L3	$1.1 \cdot 10^3$	$0.1 \cdot 10^3$	$4.5 \cdot 10^{-18}$	$0.4 \cdot 10^{-18}$	2.5	0.3
wt	$1.7 \cdot 10^3$	$0.2 \cdot 10^3$	$6.7 \cdot 10^{-18}$	$0.8 \cdot 10^{-18}$	2.4	0.3

Particle	$F_{average}$ (nN)	error (nN)	ΔF (nN)	$Area_{hexon}$ (nm^2)	P (atm)	error (atm)
FC31-L3	1.8	0.3	1.0	62.2	$1.6 \cdot 10^2$	$0.9 \cdot 10^2$
wt	2.8	0.3				

Table 5.6: Estimation of pressure from hexon displacement assays. From the capsomer-capsomer interaction energy (table 5.5) we can estimate the energy required to move one hexon for *wt* and *FC31-L3*, and the average force that carries out the work. The difference in force for a hexon in *wt* and in *FC31-L3* is the work against the genome. Taking into consideration the hexon as a disc, we can estimate the pressure exerted by the *wt* core.

Particle	Spring constant (N/m)	SEM (N/m)	n	Force (nN)	SEM (nN)	n
wt (new data) ●	0.56	0.02	77	5.0	0.1	65
wt heated NO pentonless ●	0.51	0.05	25	4.8	0.2	25
wt heated pentonless ○	0.42	0.06	18	3.2	0.2	18
wt (old data) ●	0.46	0.02	25	3.3	0.2	25
FC31-L3 ■	0.41	0.01	61	2.6	0.1	51
FC31-L3 heated NO pentonless ■	0.36	0.08	7	1.7	0.4	7
FC31-L3 heated pentonless □	0.29	0.03	32	1.7	0.1	32

Table 5.7: Data of the stiffness of heated viruses. Data depicted in figure 5.13 for stiffness diminution due to structural damage by heating that may explain the difference in the average of data of *wt* virus in sections 3.3.2 and 5.8.

Chapter 6

Fluorescence tracking of genome release during mechanical uncoating of single viruses

6.1 Introduction

In the previous chapter 5, we saw that the viral maturation may be essential for the confined virus genome to reach a metastable state that prepares virus for infection. Moreover, we proved in chapter 4 that pentons are the first capsomers to be released, and that the partially disrupted capsid lasts a while before total collapse, as described for the *in vivo* transport from endosomes to nuclear pore complex in the cell.[38,48,49,190,191] But the question about how genome is released remained unanswered in viral disassembly AFM experiments.

As reported in chapter 1, the adenovirus genome is a minichromosome composed of dsDNA and some condensing proteins.[30–33,192] The exact architecture of this DNA-protein core is unknown. In the adenovirus assembly, the maturation step is essential for the viruses to become infectious.[18,149] During this step, the viral protease (AVP)

that is packed in the capsid cleaves the condensing proteins along with other capsid proteins,[18,163] which leads to a change in the organization of the viral core as observed by electron microscopy.[26,57] The temperature sensitive adenovirus mutant *ts1* fails to package functional protease, contains uncleaved core proteins and is not infectious.[149]

In this chapter, we combine AFM and single molecule fluorescence microscopy to simultaneously induce and observe genome uncoating for *wild type* and *ts1* adenovirus. The combination of these techniques allows simultaneous manipulation and imaging of samples, which has been applied for the measurement of mechanical properties of single proteins and the tracking of specific components in complex assemblies.[193–195]

The results presented in this chapter were obtained thanks to a joint effort with Dr. Bodensiek, during my short-term research visit at the group of Dr. Schaap in *Georg-August-Universität Göttingen*, in collaboration with Prof. Dr. Greber from *University of Zurich*.

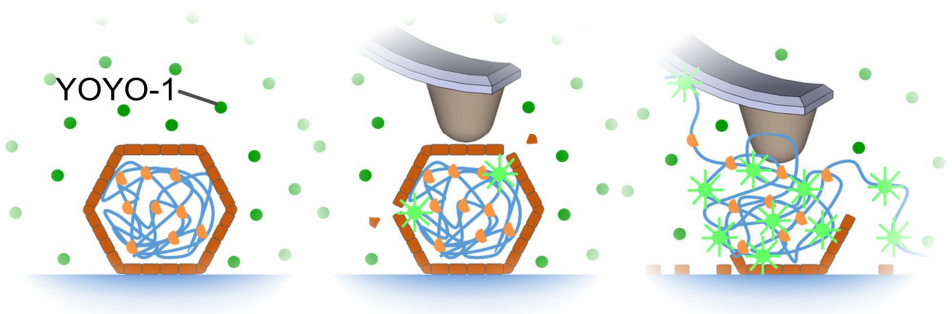

Figure 6.1: AFM-induced disassembly of adenovirus in the presence of YOYO-1. First the pentons are released, followed by complete disassembly. To track the genome release, the experiments are performed in the presence of YOYO-1 dye-molecules (dark green circles) that become fluorescent after binding to DNA (bright green stars).

6.2 Combining single molecule fluorescence with high resolution AFM

Atomic force microscopes enable disrupting,[131,196] manipulating[133,145,171] and disassemblinging[156,159] protein shells by the application of forces in a controlled way. AFM can only resolve fixed particles on surfaces, what means that flexible materials and particles is suspension cannot be imaged. Thus, induced genome release in adenovirus cannot be resolved by AFM,[159] since DNA is flexible and may float in the medium. Monitoring detailed effects of biomolecular mechanics needs of the combination of single molecule manipulation methods and detection techniques.[194]

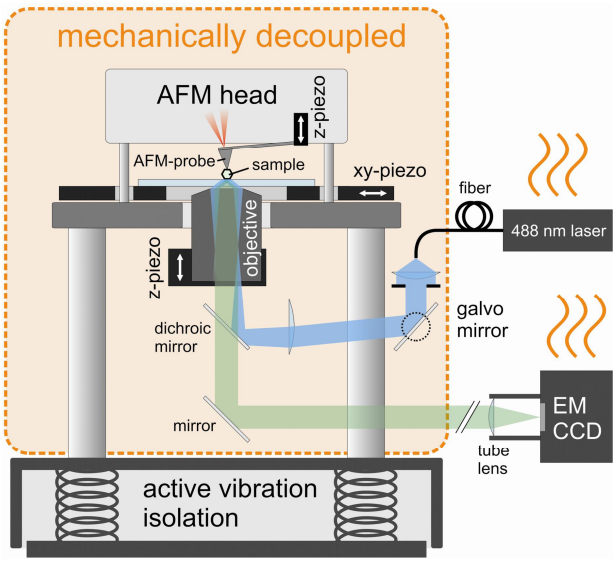

Figure 6.2: AFM-TIRF microscope scheme. The main parts of the coupled AFM and TIRF microscope are depicted in the scheme. The camera that records the fluorescence signal and the excitation laser to excite the dye, were mechanically and thermally isolated from the AFM to limit heat and vibration transmission. Courtesy of Dr. Schaap.

Genome exposure can be tracked with a DNA specific intercalating fluorescent dye (YOYO-1 – Life Technologies, CA, USA) that can only access the DNA after the capsid had been opened up (figure 6.1). YOYO-1 is a dye which shows an increase in fluorescence intensity of 3 orders of magnitude upon dsDNA binding.[197] To be able to col-

lect fluorescent signals from the released virus genomes during AFM manipulation, the group of Dr. Schaap integrated and designed a single molecule fluorescence microscope in a commercial AFM (*Asylum Research*, MFP-3D, CA, USA). To excite only the fluorescent dye molecules close to the surface we used a total internal reflection fluorescence (TIRF) layout. This is necessary to minimize the background signal from the AFM probe itself that remains largely out of the evanescent excitation field.[198]

An EM-CCD (electron multiplying charged coupled device – Luca S-659 cooled EM-CCD, *Andor technology*, UK) camera and the laser source (both at the right in figure 6.2) for the fluorescence microscope, are mechanically decoupled from the AFM to prevent the transmission of noise. We used an exposure time of 100 ms per TIRFM frame, which resulted in an acquisition frame rate of 7.5 Hz.

The AFM head rests on the custom-made inverted microscope (figure 6.2). A microscope coverslip that holds the sample is mounted onto the AFM xy-piezo stage, such that the AFM probe has access from above. Optical access is obtained from below through a TIRF objective (100x, NA 1.49, *Nikon Instruments*, Japan). Excitation of the fluorescent molecules is performed by a 488 nm laser (*Nichia*, Japan) coupled into a single-mode fiber. After collimation of the fiber output, the laser beam is coupled into the path of the optical microscope. As a first mirror we use a closed-loop adjustable galvo mirror. Because this mirror is placed in a plane that is conjugate to the focal plane, we can adjust the angle of the excitation beam. The parts of the combined microscope indicated by the orange box (figure 6.2) rest on an active vibration isolation within an acoustic enclosure.

For the adenovirus genome mechanical unpacking measurements with AFM, the viral particles were firmly immobilized via Ni^{2+} ions to a freshly cleaved mica substrate as described in section 3.2.3.1. To enable the use of a high numerical aperture (NA) microscope objective for fluorescent imaging, we glued a very thin ($\sim$ tens of μm) circular punched mica slice with an optical adhesive to a coverslip. The refractive index of the optical adhesive (1.54, *Norland products*,

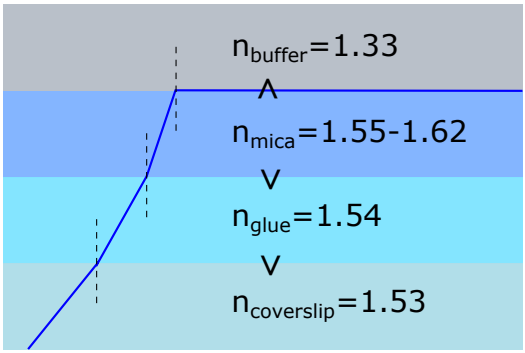

Figure 6.3: Glued mica on glass for TIRF. To allow the blue light excitation laser reach the sample, it was necessary to use an optical glue with an intermediate refractive index between mica and glass. Adapted from the thesis of Dr. Bodensiek.[199]

NJ, USA) was chosen between that of mica (1.55-1.62) and the microscope coverslip (1.53) to ensure total internal reflection at the mica buffer interface (figure 6.3).

Figure 6.4 shows that this solution provides single fluorescent molecule sensitivity in the presence of the AFM probe. For the actual genome unpacking experiments the light angle was set at 64° to eliminate the background signal from the AFM probe. Moreover, the work was developed using rectangular cantilevers RC800PSA (*Olympus*,Tokyo, Japan) with nominal spring constant of 0.39 N/m, which do not have gold-coated tips to avoid dye molecule quenching.[200,201]

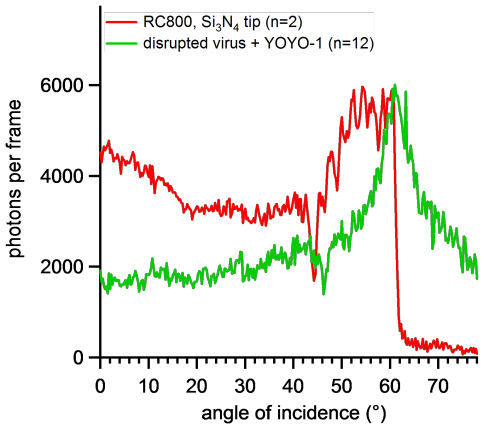

Figure 6.4: Fluorescence signal from AFM probe and sample at different illumination angles. Background signal from the AFM probe (in surface contact, red) compared to the intensity from single disrupted viruses (green). Sufficient signal-to-noise is only available in the TIRF regime, which starts at 61°, where the signal from the AFM probe drops to much lower values than the virus.

6.3 Slow genome unpacking by mechanical fatigue

First, we verified that we could monitor the exposure of the viral genome during gradual mechanical uncoating of the virus. To this end we mimicked the uncoating process of human adenoviruses with fatigue experiments explained in chapter 4. Since this microscope can not operate in Jumping Mode, we scanned the samples in amplitude modulation mode at an oscillation amplitude of less than 10 nm at ≈15 kHz (section 2.1.4.2). Intact viruses were located by scanning large areas, and then reducing the scan size to 400x400 nm^2 and 128x128 $pixels^2$. Single capsids were repeatedly and gently scanned assuring to work below the rupture strength, which ultimately resulted in a stepwise disruption of the shell.[159] Figure 6.5 and *Movie_1_ACSNano* (movie caption at the end of the chapter) show a mechanical fatigue disruption experiment performed on a mature adenovirus particle. YOYO-1 was present in the buffer at 300 nM to monitor the exposure of the genome.

The particle was imaged 21 times (where each scan line was performed forward and backward). After each AFM frame the scan was stopped, the excitation laser was switched on and 10 fluorescence images were recorded and averaged. For the next AFM frame, the laser was turned off to limit bleaching of the YOYO-1 dye molecules. The first AFM frame in figure 6.5 (a) shows the scan of the intact viral particle. The first fluorescence frame presents background noise confirming that the capsid is intact and the dsDNA is inaccessible to YOYO-1. In AFM frame 7, the viral particle has lost its first vertex (penton, indicated with a circle). In the corresponding fluorescence frame 7 a dim intensity spot appeared, which remained stable until frame 16. From AFM frame 17 new defects appeared until at frame 21 the particle was completely disrupted. The corresponding fluorescence frames show that the emission intensity (figure 6.5 (b)) increases with capsid disruption, which indicates that the DNA genome becomes increasingly accessible to YOYO-1 and remains co-localized with the

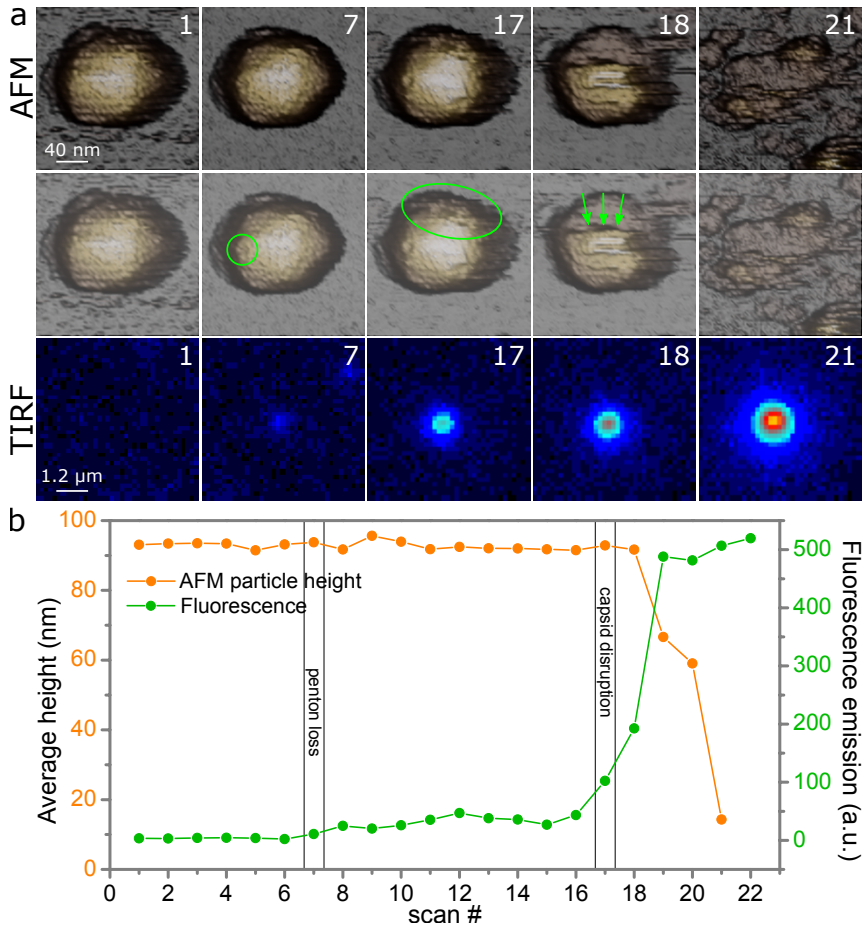

Figure 6.5: Slow unpacking of adenovirus genomes. (a) The first row shows the key AFM images of the fatigue experiment of a mature particle obtained in dynamic mode. The second row indicates the loss of the first penton in frame 7 with a circle. The ellipse in frame 17 shows the nucleation point for further disruption. The arrows indicate the direction of further disassembly in this experiment. After each scan, the fluorescence intensity was collected to monitor genome exposure. The time between consecutive images was 2 minutes. See also *Movie_1_ACSNano*. (b) Evolution of the average height (left axis, orange) and fluorescence emission (right axis, green) corresponding to the fatigue experiment.

capsid. The genome itself remains invisible in the AFM scans due to its softness and mobility. This experiment shows that the method is sensitive enough to detect the release of a single pentameric capsomer via an increase in fluorescence intensity.

6.4 Fast genome unpacking by nanoindentation assays

Because capsid disassembly during fatigue experiments may be a stochastic process,[159] the slow genome unpacking assay would result in a distribution of capsids at various stages of uncoating and thus in a high variability of the fluorescent signals obtained from different particles. To synchronize disassembly, we sought a method for fast removal of the capsid, so that we could investigate the physical state of the viral genome itself. A routine was implemented in the AFM controller software to generate a trigger for the EM-CCD camera to acquire the AFM and fluorescence data at the same time during the unpacking experiments.

Figure 6.6 (a) shows that the capsid can be completely disrupted within 0.5 s by performing a single force curve at a speed of ≈0.4 μm/s with a maximum force of around 15 nN, well above the rupture strength of the capsid as described in section 3.3.1. Prior to the force curve the capsid was intact, while afterward it was completely disassembled leaving the viral core exposed.

No fluorescent signal was present before the force curve: the intensity of fluorescence emission corresponds to the background noise. When the AFM tip touches the capsid (at 2.2 s) the force increases. The sudden downwards step (at 2.3 s) occurs when the AFM tip breaks the virus. The corresponding time trace of the experiment (figure 6.6 (b)) confirms that the intensity of the fluorescence signal increases at that moment, and remains high after the AFM probe has retracted (*Movie_2_ACSNano*). A bright spot appeared due to the viral genome

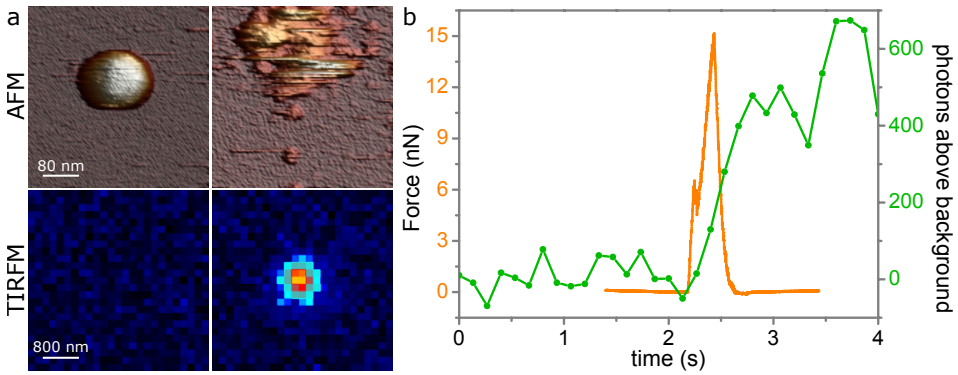

Figure 6.6: Fast unpacking of adenovirus genomes. (a) The first row shows the AFM topography of a virus particle before and after mechanical disruption. The second row shows the appearance of a fluorescent spot after disruption. (b) Temporal evolution of the force (left axis, orange) and fluorescence (right axis, green) during the nano-indentation experiment. See also *Movie_2_ACSNano*.

becoming accessible to the YOYO-1 dye (figure 6.6 (a)). With the fast unpacking assay we can synchronize the fluorescence intensity curves with sub-second accuracy which provides a method to investigate the changes in genome organization in more detail.

6.4.1 Maturation increases the accessibility of the adenovirus core for YOYO-1 molecules

To investigate if the structural differences between the viral cores of the mature and immature adenovirus have an effect on their diffusion after release, we repeated the fast genome unpacking assay on *wt* and *ts1* particles. If the viral core remains compact after unpacking, which we expect for the immature particle, it will be difficult for the dye to access binding sites. If, on the other hand, the nucleoprotein complex expands after unpacking, binding of the dye to the DNA will be enhanced.

We performed fast unpacking experiments on 16 mature and 17

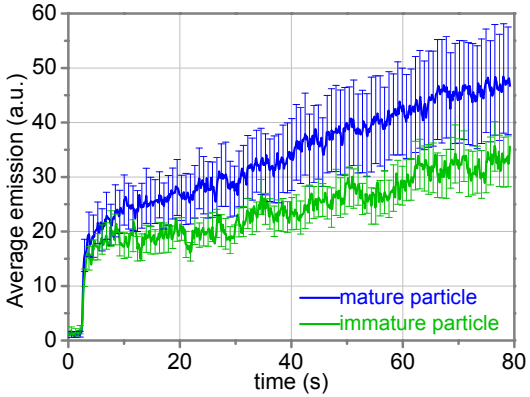

Figure 6.7: Average fluorescence emission of viruses after fast unpacking. The average fluorescence emission after breakage for mature (blue, n=16) and immature (green, n=17) adenovirus particles. The error bars show the standard error of the mean (SEM).

immature adenovirus particles and recorded the fluorescence intensity for 80 seconds after opening the capsids. Figure 6.7 shows the average fluorescence emission for both cases. Consistent with the behavior shown in figure 6.6 (b), the emission rises sharply after rupturing the capsids and continues to increase slowly afterward. This increase represents the average rate of binding and bleaching of the YOYO-1 molecules. Under our conditions, the binding rate of new YOYO-1 molecules is higher than their bleaching rate. The averaged signal for the mature virus genomes is higher than that of the immature ones. This agrees with a looser organization of the mature core which leads to a better accessibility of the dye to dsDNA.

6.4.2 The mature adenovirus core expands after release

To further evaluate the possible expansion of the mature genome after fast unpacking, we measured the size of the fluorescent spot. The diffraction limited resolution of our optical system restricts the size of the smallest spot that we can observe to a size of about 200 nm which is larger than the intact virus (95 nm). However, if the labeled sample is a collection of spatially spread point sources, this will lead to a dilation of the imaged spot from which we can estimate the expansion of the viral core. We quantified the width by fitting a 2D gaussian

function to the imaged fluorescent spots:

$$f(x,y) = z_0 + A \cdot exp\left[-\left(\frac{(x-x_0)^2}{width^2} + \frac{(y-y_0)^2}{width^2}\right)\right] \tag{6.1}$$

where z_0 is the noise floor, x_0, y_0 the center and A the amplitude of the spot. The *width* is the reported parameter.

Dr. Bodensiek and Dr. Schaap measured if the exact focus position and the collection of spatially spread point sources had a large effect on the measured spot size. They attached 100 nm diameter fluorescent beads (TetraspeckTM, *Life Technologies*, CA, USA) to the surface and changed the z-focus in steps of 50 or 100 nm. The spot size was obtained by using the *width* of the Gauss fit (equation 6.1). For glass (red, figure 6.8) the minimum width was 148 nm, larger than the theoretical spot size of a point source (71 nm) due to the convolution of multiple point sources that result from the use of a 100 nm diameter bead. For mica (green, figure 6.8) the width increased to 208 nm, due to the refractive index mismatch. When 200 nm diameter fluorescent beads (Fluoresbrite, *Polysciences Europe GmbH*, Germany) were used on mica, the fitted width further increased to 253 nm (blue, figure 6.8), which shows that the fitted width scales with the size of the object. In all cases a change of focus of ± 250 nm had little effect on the spot size.

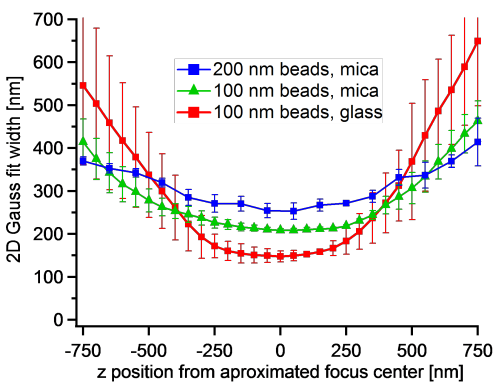

Figure 6.8: Fluorescent spot size at different focus positions. Measured spot size of attached 100 nm diameter fluorescent beads on glass (red, n=3) and mica (green, n=3), and 200 nm beads on mica (blue, n=3). When we compared the spot sizes from 100 nm and 200 nm diameter fluorescent beads we found an increase in width from 208 nm to 253 nm.

To compare the genome condensation state in both types of adenovirus particles, we determined the fluorescence spot size in each frame of all studied particles. To obtain the mean width, all fluorescence frames were averaged and the resulting image was fitted with a 2D Gauss function. Figure 6.9 (a) shows the average fits for all particles, revealing that the mature core shows a spot width of 295 nm, which is much larger than the 229 nm of the immature core. This expansion of 66 nm represents a lower limit, while further diffusion of the genome may be hindered by the surface-immobilized remainder of the capsid as shown in figure 6.6 (a).

To investigate the temporal evolution of the core expansion we plotted the fitted width of each frame as a function of time. Figure 6.9 (b) shows that the expansion occurs directly after opening the capsid with the AFM probe and remains fairly constant afterward. The apparent width of the mature particle genome was more variable at the beginning of the observation, and became smaller after ∼20 s, possibly suggesting photocleavage of mobile extended parts of the genome.[202]

6.5 Biological context

Tracking experiments of single viruses in cells have shown that the viral genome is already exposed to the cytosol before the capsid docks at the nuclear pore complex.[49] DNA is accessible to small organic probes, which implies that solutes from endosomes or the cytosol, such as ions can access the viral DNA. *In vivo*, the removal of the pentameric capsomers might be initiated at the cell surface and continues in the endosomes.[38] Our slow unpacking experiments with the combined TIRF-AFM instrument are fully consistent with these observations by proving that the removal of only one capsomer sufficed to expose the viral dsDNA to the YOYO-1 molecules in the buffer.

The fast unpacking experiments induce the particle disruption and allow tracking of the genome release on the sub-second timescale. *In*

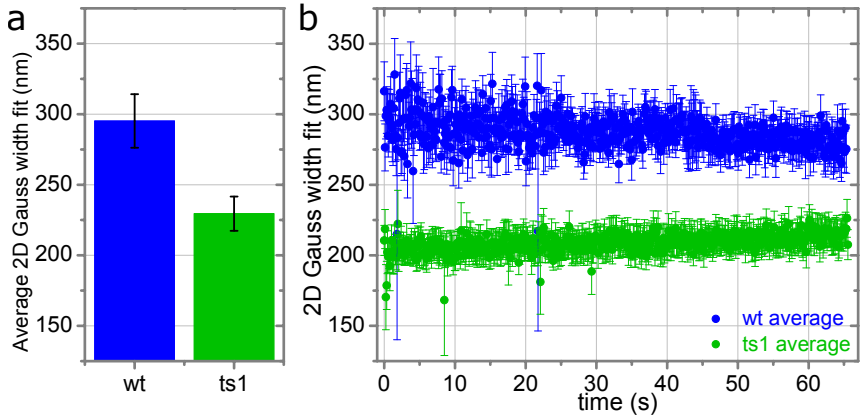

Figure 6.9: The spatial spread of the mature and immature adenovirus genomes. (a) Graph shows the average fits for all genomes. The error bars show the SEM. The immature adenovirus genome (green, n=16) has a width of 229 nm. This lies in the range of what was observed in control experiments with 100 and 200 nm diameter fluorescent beads that showed widths of 208 and 253 nm, respectively (figure 6.8). The width of the mature particle genome (blue, n=17) is expanded by 66 nm to 295 nm. (b) To verify if the observed dilation evolves over time each individual frame was fitted with a 2D Gauss function. Each data point shows the mean of the frames from the different viruses. The error bars show the SEM.

vivo, about 60 minutes pass between the uptake of the virus and DNA release into the nucleus.[49,148,203,204] The disruption of the capsid at the nuclear pore complex likely happens much faster, owing to several virus uncoating and transport steps that are upstream of the nuclear pore complex, the site of capsid disruption.[38,41,205,206] The main driver of capsid disassembly at the nuclear pore complex is the conventional kinesin motor,[50] which has a stepping rate of about 10 ms.[207] The temporal resolution of our fast unpacking experiments could be realistically increased by an order of magnitude by performing faster force curves and using higher video frame rates.

The unpacking experiments showed directly the differences in condensation between the mature and immature adenovirus cores. The mature core was more accessible to YOYO-1 molecules and showed

a larger spreading after fast unpacking. The spatial expansion of the mature genome occurs immediately after unpacking which indicates that it is kept under stress when packed. Indeed, AFM measurements have shown a ≈20 % increase in the stiffness of mature adenovirus over the immature particle,[57] which suggests an internal pressure that is exerted by the confined genome (chapter 5). Interestingly, our measurements show that although the mature core expands more, it still retains a somewhat compact organization and does not completely unfold. Although this might be influenced by the affinity of the genome for the remaining surface-bound capsid proteins, it is intriguing that also tracking of single adenoviruses in infected cells showed that many uncoated viral genomes remained in the cytosol and did not enter the nucleus.[49]

6.6 Conclusions

The transient and dynamic nature of viral uncoating presents a significant challenge for investigations at the molecular level. Genome release of human adenovirus has been measured in bulk by fluorescent detection of the genomes after thermal or chemical disruption of the capsids.[26,57,147] At the single particle level, DNA ejection has been visualized in bacteriophages and herpesviruses.[208,209] As we have seen in chapter 4, AFM has been successful in imaging the disassembly of adenovirus capsids, but the release of the soft and mobile nucleic acid molecules remained invisible in such experiments because AFM imaging demands an immobilized sample. On the other hand, single molecule fluorescence allows specific tracking of DNA dynamics and provides a tool to visualize genome release. In this chapter we presented a "action-reaction" method that enables triggering and detecting the virus genome release.

We found that the core of the *wild type* adenovirus expands more and has better accessibility to the fluorescent dye than the *ts1* core, which indicates a loosening of its architecture upon maturation. The

reported expansion of the mature adenovirus genome might provide the mature core with the essential flexibility to pass through the narrow nuclear pore complex, which would contribute to infectivity. This loss of structural organization may be important for viral transcription in the cell nucleus.

Movies

Movie_1_ACSNano: **Slow unpacking of wild-type adenovirus.** Three-dimensional rendered AFM images show the temporal evolution of the virus integrity correlated with fluorescence microscopy emission images. The shown virus capsid is the same as the one shown in figure 6.5. The small changes in the vertical dimensions of the capsid is a consequence of the alternating scan direction (up-down scan direction is always followed by a down-up scan). The movie is sped up; the whole experiment took 40 minutes for the 21 AFM frames. The movie is available in the supporting information of Ortega-Esteban & Bodensiek *et. al*, 2015: http://pubs.acs.org/doi/abs/10.1021/acsnano.5b03020 as *nn5b03020_si_002.avi*.[210]

Movie_2_ACSNano: **Fast unpacking of wild-type adenovirus.** Fluorescence emission while executing a nano-indentation on an intact virus capsid. On the left side, the whole field of view of the camera is presented. It can be observed that there are already some spots of light corresponding to broken viruses or dsDNA deposited on the substrate. On the right side, a zoom shows how the fluorescence emission increases while the viral particle is disrupted as presented in figure 6.6. 100 frames are shown that correspond to approximately 13 s of real time. The movie is available in the supporting information of Ortega-Esteban & Bodensiek *et. al*, 2015: http://pubs.acs.org/doi/abs/10.1021/acsnano.5b03020 as *nn5b03020_si_003.avi*.[210]

General conclusions

In this thesis we have used atomic force microscopy to characterize different assembly states of human adenovirus in physiological conditions: the infectious, mature *wild-type* and the non-infectious, immature *ts1* particles.

- **Characterization of human adenovirus with AFM**

  1. We found that adenovirus particles attach firmly to mica in the presence of divalent ions in the medium, settling down on the 3-fold symmetry orientation without modifying their structure.
  2. The use of Jumping Mode Plus allowed imaging adenovirus in liquids, resolving intracapsomeric structure by minimizing the damage to the sample.
  3. In adenovirus, mechanical parameters do not correlate with thermal or chemical stability. The adenovirus mature capsid is brittle and stiff compared to the elastic immature particle, presenting a spring constant of 0.46 N/m and 0.38 N/m, and breaking force 3.3 nN and 2.3 nN, respectively.

- **Monitoring dynamics of human adenovirus disassembly induced by mechanical fatigue**

1. Taking advantage of the imaging mode Jumping Mode Plus, we presented a method to quantify an approximation of mechanical fatigue for single virus particles. The method enables to apply very accurate and controlled forces while at the same time imaging the sample. We induced mechanical fatigue of a capsid by repeatedly applying 100 pN forces, well bellow the breaking force (nN). This method allows to monitor in real time the sequential disassembly of a virus particle at single molecule level.
2. Topographical height evolution was used to estimate capsid integrity. The final heights for mature particles reached lower values than for the immature, indicating that in the latter the genome remains condensed due to the presence of since precursor core proteins.
3. The method is accurate enough to reveal penton stability, which correlates with the chemical and thermal bulk techniques results. The probability to cause release of a penton in one scan is 1.85 times lower for *wt* than for the *ts1*, showing that the immature capsomers are more stable. Moreover, the results show that under a mild disruption force, pentons of a virus are released sequentially.
4. The disassembly pathways is different for the two analyzed viral variants. Mature capsids unzip from a single fracture in the shell that starts at a penton vacancy and spreads through the remaining shell in a highly cooperative way, while in the immature particle cracks spread from the missing vertices and coalesce roughly following the icosahedron edges. An observation from the present study is that a source of stress so far removed from the *in vivo* situation as mechanical fatigue results in the same disassembly pattern induced by cellular cues.
5. Particle lifetime decreases as the applied force increases. We presented the first approximation for a S-N curve of biological material at single particle level.

- **Mechanics of viral chromatin reveals the pressurization of human adenovirus**

    1. Using controlled capsid disassembly assays, we gained access to the viral chromatin and provided a direct experimental analysis of the mechanics of a confined DNA-protein condensate. We found the mechanical signature of adenovirus core decompaction as a reduction of the Young's modulus during maturation ($E_{ts1} = 1.6$ MPa $> E_{wt} = 0.34$ MPa).
    2. The mechanical properties of the viral particles depend greatly on condensation state of the genome. Empty capsids are softer (0.41 N/m) than immature *ts1* adenovirus (0.49 N/m) which in turn is softer than the *wt* particle (0.56 N/m).
    3. Mature virus recovers the mechanical properties of the immature particle in the presence of DNA-condensing polyamines, which proves the existence of electrostatic repulsion in the minichromosome.
    4. The capsid and core stiffness mechanical contrast leads to the idea that core loosening pressurizes adenovirus particles in maturation. Uncleaved core proteins in the immature particle or spermidine in the mature virion act as DNA condensing agents, reducing its effective persistence length.
    5. The confined adenovirus genome, in spite of having part of its charges neutralized by proteins, induces a significant internal pressure, that with some theoretical models we estimate at $\sim$30 atmospheres considering that the confined viral chromatin behaves as a compact polymer with an effective persistence length of 240$\pm$40 nm.
    6. From hexon displacement experiments in *wt* and empty particles, we can estimate hexon binding energy ($\sim 1.1 \cdot 10^3$ $k_B T$) and from that an overestimated pressure value ($\sim 1.6 \cdot 10^2$ atm).

7. We notice that the measurements presented a larger rigidity than the ones previously reported for both *wt* and *ts1*. This difference is related to the particle integrity.

- **Fluorescence tracking of genome release during mechanical uncoating of single viruses**

1. By combining AFM and fluorescence microscopy based on total internal reflection (TIRFM), we presented a method that enables triggering and detecting adenovirus genome release. By mechanically disrupting the virus capsid in the presence of a DNA binding fluorophore (YOYO-1) we can track its genome accessibility to the medium at single particle level.
2. The core of the *wild type* adenovirus expands more and has better accessibility to the fluorescent dye than the *ts1* core, which corroborates a loosening of its architecture upon maturation.
3. By inducing mechanical fatigue disassembly of the capsid, we observed that the genome in pentonless particles is mostly not accessible until total capsid disruption, suggesting that the genome is protected in cytosol of the cell despite the missing pentons.

We can conclude that the adenovirus core rearrangement during maturation has a large contribution in viral mechanics. This structural change switches adenovirus from a stable to a metastable and brittle state that enables and cooperates with other factors to facilitate the beginning of the stepwise disassembly in the cell, enabling its escape from the endosome. The uncondensed genome of the mature virus is, although partially exposed to small organic probes, protected until it reaches the nuclear pore where it is able to diffuse out from the disrupted capsid for successful infection.

Conclusiones generales

En esta tesis se ha utilizado microscopía de fuerzas atómicas para caracterizar diferentes estados de ensamblaje de adenovirus humano en condiciones fisiológicas: el virión maduro e infeccioso, y el mutante *ts1* que produce partículas inmaduras no infectivas.

- **Caracterización de adenovirus humano con AFM**

  1. Hemos observado que las partículas de adenovirus se adhieren firmemente a la mica en presencia de iones divalentes en el medio. Se adsorben en la orientación de simetría 3, sin modificación apreciable en su estructura.
  2. El modo Jumping Plus ha permitido la adquisición de imágenes en líquidos, minimizando el daño de la muestra y llegando a resolver estructuras intracapsoméricas.
  3. Las propiedades mecánicas de adenovirus humano no se correlacionan con la estabilidad térmica o química. La cápside madura de adenovirus es más frágil y rígida en comparación con la partícula inmadura, presentando unas constantes elásticas de 0.46 N/m y 0.38 N/m, y fuerzas de rotura de 3.3 nN y 2.3 nN, respectivamente.

- **Monitorización del desensamblaje del adenovirus humano mediante fatiga mecánica**

1. Aprovechando el modo de medida Jumping Plus, presentamos un método para cuantificar la fatiga mecánica de partículas virales individuales. El método permite aplicar fuerzas muy precisas y controladas, al mismo tiempo que se adquieren imágenes de la muestra. Aplicando fuerzas (100 pN) por debajo de la fuerza de rotura de la cápside (nN), se provoca fatiga mecánica de la partícula vírica. Este método permite monitorizar en tiempo real el desensamblaje secuencial de un virus a nivel individual.
2. La evolución de la altura permite cuantificar la integridad de la cápside. Se ha demostrado que las alturas finales para las partículas maduras alcanzan valores más bajos que para las inmaduras, indicando que en estas últimas el genoma permanece condensado debido a la presencia de precursores de las proteínas unidas al ADN.
3. El método es lo suficientemente preciso como para revelar la estabilidad de los pentones, que se correlaciona con los resultados de técnicas en masa (calorimetría). La probabilidad de pérdida de un pentón en la toma de una imagen es 1.85 veces mayor para la partícula madura que para la *ts1*, mostrando que dichos capsómeros son más estables en el virus inmaduro. Además, los resultados muestran que los pentones se liberan secuencialmente.
4. El desensamblaje de la cápside proteica para las dos variantes virales analizadas es diferente. La cápside del virus maduro se destruye de forma cooperativa a partir de la vacante de un pentón, mientras que en el virus inmaduro se producen grietas entre capsómeros que se alargan siguiendo las aristas del icosaedro a partir de vértices contiguos desocupados. Los patrones de desensamblaje reportados por fatiga mecánica del virus son similares a los causados por señales celulares *in vivo*.
5. La resistencia a la fatiga de las partículas víricas disminuye a medida que se aumenta la fuerza aplicada en los experimentos. Se ha obtenido por primera vez una aproxi-

mación de una curva S-N de un material biológico a nivel de partícula individual.

- **El análisis de las propiedades mecánicas de la cromatina viral revela la presurización del adenovirus humano**

  1. Mediante el desensamblaje controlado de la cápside vírica, se ha conseguido acceder a la cromatina viral y proporcionar un análisis experimental directo de las propiedades mecánicas del condensado de proteína y ADN. La descompactación del genoma del adenovirus durante la maduración se ha cuantificado con la medida de la rigidez mediante el módulo de Young ($E_{ts1} = 1.6$ MPa $> E_{wt} = 0.34$ MPa).
  2. Las propiedades mecánicas de las partículas dependen en gran medida del estado de condensación del genoma. Las cápsides vacías son más elásticas (0.41 N/m) que las partículas inmaduras *ts1* (0.49 N/m), las cuales a su vez son más elásticas que las partículas maduras (0.56 N/m).
  3. Los ensayos en presencia de agentes condensadores de ADN han mostrado que en el virus maduro recupera las propiedades mecánicas de la partícula inmadura. Esto indica que existe una repulsión electrostática entre hebras del genoma.
  4. El contraste entre la rigidez mecánica de la cápside y el minicromosoma sugieren que la distensión de la cromatina viral durante la maduración presuriza las partículas de adenovirus. Las proteínas precursoras unidas al genoma en la partícula inmadura, o la espermidina en el virus maduro, actúan como agentes condensadores de ADN, reduciendo su longitud de persistencia efectiva.
  5. El genoma del adenovirus confinado en la partícula, a pesar de tener parte de sus cargas neutralizadas por proteínas, produce una presión interna considerable, que con ayuda de modelos teóricos se estima en $\sim$30 atmósferas, considerando que la cromatina viral se comporta como un polímero compacto con una longitud de persistencia eficaz de $\sim$240 nm.

6. A partir de experimentos de desplazamiento de hexones en las partículas maduras y vacías, se ha estimado la energía de enlace del hexón ($\sim 1.1 \cdot 10^3$ $k_B T$) y a partir de ésta, un valor de presión sobreestimada ($\sim 1.6 \cdot 10^2$ atm).
7. Se observó que las medidas de rigidez obtenidas en esta parte del trabajo eran mayores que los resultados previos tanto para el virus silvestre como para *ts1*. Se ha demostrado que esta diferencia se relaciona con la integridad estructural de las partículas.

- **Seguimiento de la salida del genoma viral por combinación de disrupción mecánica de virus individuales y microscopía de fluorescencia**

1. La combinación de AFM y microscopía de fluorescencia basada en la reflexión interna total (TIRFM), nos permite provocar y observar simultáneamente la liberación del genoma del adenovirus. Induciendo mecánicamente el desensamblaje de la cápside del virus en presencia de un fluoróforo que se une al ADN (YOYO-1), se ha realizado un seguimiento de la accesibilidad genoma al medio a nivel de partícula individual.
2. El minicromosoma del adenovirus maduro se expande más y tiene mejor accesibilidad al fuoróforo que el del *ts1*, corroborando la distensión de su arquitectura en la maduración.
3. Induciendo el desensamblaje de un virus por fatiga mecánica, se ha observado que el genoma en partículas con pentones vacantes no es del todo accesible al medio hasta el desensamblaje total de la cápside, sugiriendo que el genoma está parcialmente protegido en el citosol de la célula a pesar de los pentones ausentes.

Podemos concluir que la reordenación del minicromosoma durante la maduración del adenovirus se refleja en las propiedades mecánicas de la partícula viral. Este cambio estructural del adenovirus de un

estado estable a uno metaestable y quebradizo, facilita el inicio del desensamblaje secuencial en la célula, permitiendo así su escape del endosoma. Aunque el minicromosoma menos condensado del virus maduro se encuentra parcialmente expuesto a pequeñas moléculas orgánicas, está protegido hasta que alcanza el poro nuclear donde es capaz de difundir fuera de la cápside desensamblada para una infección exitosa.

Appendix A

MATLAB programs

Some MATLAB programs have been implemented to carry out data analysis of this thesis. The programs and codes can be found here: https://www.dropbox.com/s/9lmhgmn7prse5mm/MATLAB_programs.rar?dl=0 in a compressed file, and can be used by any user upon request, bearing in mind that they are provided "as is", without further support.

A.1 Indentation analysis

The program presented here computes the indentation curve from the force curve on the substrate (which provides the sensitivity) and the force curve of the sample (sections 2.1.5 and 3.3.1). Figure A.1 shows a screenshot of the program with an example. The user can browse and load the raw data curves that will be displayed on the panels. The indentation is computed automatically when the sensitivity is previously calculated by a linear regression analysis between two points on the substrate curve, the cantilever stiffness is entered and the curve on the sample is loaded.

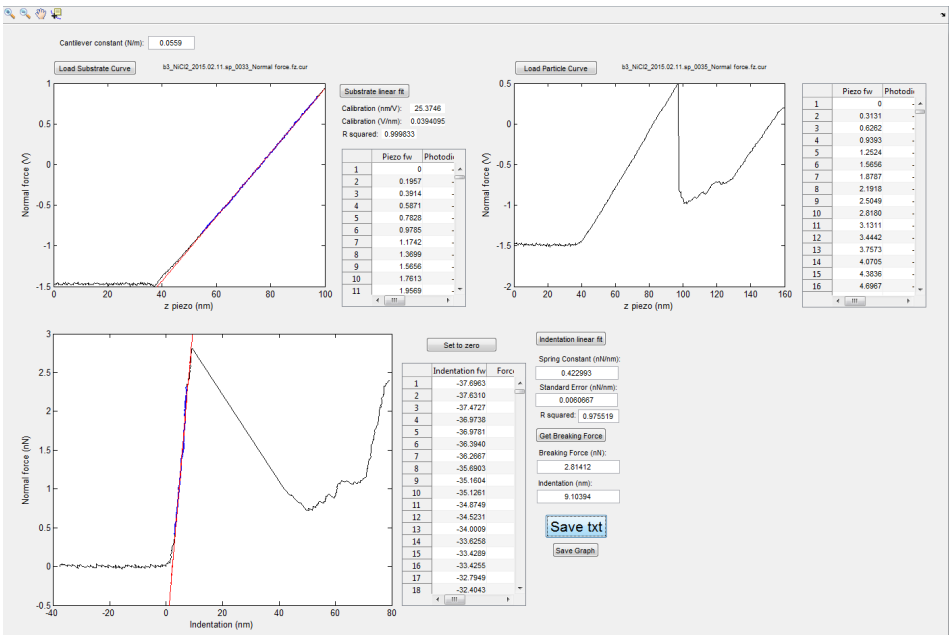

Figure A.1: Screenshot of the MATLAB program for indentation analysis.

```
Folder loaded files: D:\Alvaro\Medidas\2015\02_February2015\2015.02.11\spermidine\
Subtrate curve file: (b3_NiCl2_2015.02.11.sp_0033_Normal force.fz.cur)
Subtrate particle file: (b3_NiCl2_2015.02.11.sp_0035_Normal force.fz.cur)
Cantilever Spring Constant (N/m): 0.0559 and substrate calibration (V/nm):0.0394095; r-squared:0.999833
Spring constant of the particle (nN/nm):0.422993±0.0060667; r-squared:0.975519
Breaking force (nN):2.81412
Indentation at breaking force (nm):9.10394
z.s.f = z piezo on substrate (forward) (nm); p.s.f = photodiode on substrate (forward) (V)
z.s.b = z piezo on substrate (backward) (nm); p.s.b = photodiode on substrate (backward) (V)
z.p.f = z piezo on particle (forward) (nm); p.p.f = photodiode on particle (forward) (V)
z.p.b = z piezo on particle (backward) (nm); p.p.b = photodiode on particle (backward) (V)
i.p.f = indentation on particle (forward) (nm); f.p.f = force on particle (forward) (nN)
i.p.b = indentation on particle (backward) (nm); f.p.b = force on particle (backward) (nN)
d.f = fitted data (nN); fit = fitting (nN) (their x values is the indentation (forward))
 klever          V/nm      r_sqrsubs      kparticle      se_kpart      r_sqrpart          force      ind-force
     0.0559       0.0394         0.9998         0.4230        0.0061         0.9755         2.8141         9.1039
  z.s.f          p.s.f          z.s.b          p.s.b          z.p.f          p.p.f          z.p.b          p.p.b          i.p.f
     -0.0000       -1.4548        0.0000        -1.4340       -0.0000       -1.4850       -0.0000       -1.5189       -3
      0.1957       -1.4624        0.1957        -1.4252        0.3131       -1.4752        0.3131       -1.5021       -3
      0.3914       -1.4746        0.3914        -1.4111        0.6262       -1.4691        0.6262       -1.5045       -3
      0.5871       -1.4832        0.5871        -1.4322        0.9393       -1.4764        0.9393       -1.5277       -3
      0.7828       -1.4716        0.7828        -1.4392        1.2524       -1.4639        1.2524       -1.5179       -3
      0.9785       -1.4642        0.9785        -1.4459        1.5656       -1.4746        1.5656       -1.5179       -3
      1.1742       -1.4716        1.1742        -1.4401        1.8787       -1.4673        1.8787       -1.5125       -3
```

Figure A.2: Screenshot of the output text file of the MATLAB program for indentation analysis.

The user can set the zero force level of the indentation by selecting two points of the non-contact region of the curve. Then, a linear regression to obtain the stiffness can be computed by delimiting the region of the curve to fit by selecting two points on the graph. The

breaking force can be obtained by manually selecting the point on the graph according to the user's criterion. Finally, a text file can be saved with the input and the output data (figure A.2).

A.2 Height evolution analysis

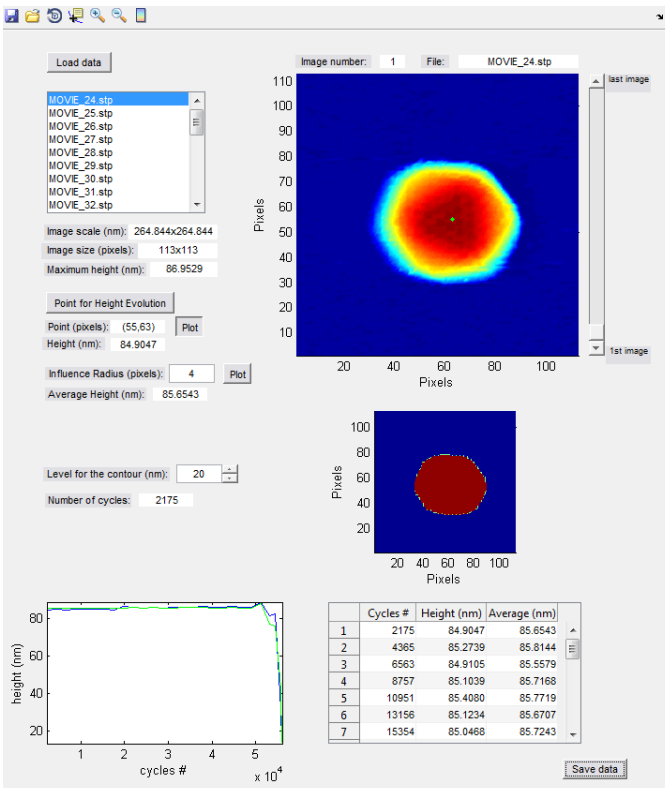

Figure A.3: Screenshot of the MATLAB program for height evolution analysis.

This program (figure A.3) helps to analyze the height evolution of a particle resulting in the same graph as explained in section 4.3.1.3. The frames have to be aligned and saved in a session with WSxM,[71] that creates a folder with *.stp* files. Load all the files together to analyze, by selecting from the latest to the first. The particle will

be plotted on the panel where the user can select a point to measure the height evolution that automatically will be plotted in the panel at the bottom. An influence radius can be selected to obtain an average height evolution of several points of the particle. For high samples such as adenovirus, the user can exclude heights lower than a value (using the *level for the contour (nm)*) to estimate how many times at each image the AFM tip pushes the particle (number of cycles). A text file can be saved with the input files and the output data (figure A.4).

```
Folder loaded files: D:\Alvaro\Medidas\2015\03_March2015\2015.03.24\2015..03.24.wt.01_3_files\
Computed point to measure the height evolution (x,y) (pixels): (55,63)
Influence radius to compute IRHE (pixels): 4
Height to measure the number of cycles at each image (nm): 20
A = Archive
# = Number of points
t = Time from the beginning (minutes)
CI = Cycles in one image
CC = Cumulative cycles
SHE = Single Height Evolution (nm)
IRHE = Influence Radius Height Evolution (nm)
     A          #        t          CI          CC          SHE          IRHE
MOVIE_24.stp    1        3.2784     2175        2175        84.9047      85.6543
MOVIE_25.stp    2        6.5568     2190        4365        85.2739      85.8144
MOVIE_26.stp    3        9.8352     2198        6563        84.9105      85.5579
MOVIE_27.stp    4       13.1136     2194        8757        85.1039      85.7168
MOVIE_28.stp    5       16.3920     2194       10951        85.4080      85.7719
MOVIE_29.stp    6       19.6704     2205       13156        85.1234      85.6707
MOVIE_30.stp    7       22.9488     2198       15354        85.0468      85.7243
```

Figure A.4: Screenshot of the output text file of the MATLAB program for height evolution analysis.

A.3 Non-linear indentation analysis

This program (figure A.5) was implemented to compute the particle stiffness from non-linear force curves and small spherical samples, based on the work by Dimitriadis *et al.*[164] (section 5.3.4). The program computes the deflection vs. indentation (w) and sets the null force to zero similarly to the code of appendix A.1. User must select a point in the non-contact region (*initial point* button) close to the contact point might be (since in this kind of curves it is not easy to discern), and set a percentage of points of the curve so that the contact point region is enclosed by the data for the fitting. Enter the parameters necessary for fitting: Poisson's ratio, type of attachment selection, tip radius, height of the sample, spring constant of the cantilever, and initial, lower and upper limit values for the deflection, indentation w and the Young's Modulus.

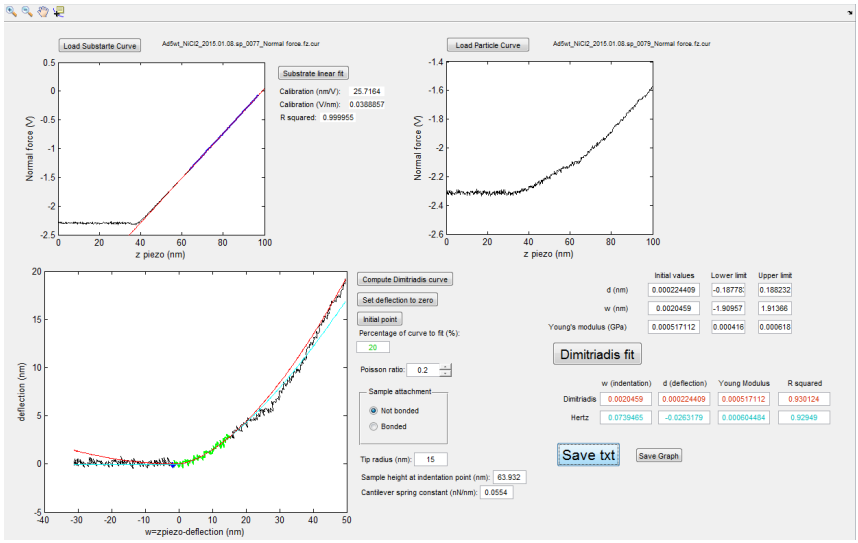

Figure A.5: Screenshot of the MATLAB program for non-linear indentation analysis.

The program fits the curve of Hertz and Dimitriadis models (blue and red in figure A.5, respectively). Results are shown in the same code color as in the graph panel. Also new initial, lower and upper limit values are computed from the parameters of the fitting, in case the user wants to iteratively improve the fit. A text file can be saved with the input and output data (figure A.6).

```
Results for the fitting described in Dimitriadis et al., Biophysical Journal (2002) and Hertz model for two spheres (computed values: contact point
Folder loaded Files: D:\Alvaro\Medidas\2015\01_January2015\2015.01.08\spermidine\
Subtrate curve file: (Ad5wt_NiCl2_2015.01.08.sp_0077_Normal force.fz.cur)
Subtrate particle file: (Ad5wt_NiCl2_2015.01.08.sp_0079_Normal force.fz.cur)
Cantilever Spring Constant (N/m): 0.0554 and substrate calibration (V/nm):0.0388857; r-squared:0.999955
Poisson ratio for fitting 0.2; considering a sample not bonded to substrate, with parameteres alpha0: -1.1278, and beta0: 0.322
Tip radius (nm): 15; height of sample at force curve (nm): 63.932; effective radius (nm): 10.2093
The initial value for the indentation (nm): 0.0020459, with lower limit (nm): -1.90957 and upper limit (nm): 1.91366
The initial value for the deflection (nm): 0.000224409, with lower limit (nm): -0.187783 and upper limit (nm): 0.188232
The initial value for the Youngs modulus (GPa): 0.000517112, with lower limit (GPa): 0.000416093 and upper limit (GPa): 0.000618131
The results for the parameters computed:
Hertz. Value of indentation at contact point (nm): 0.073946±0.59729
Hertz. Value of deflection at contact point (nm): -0.026318±0.063219
Hertz. Value of Youngs Modulus (GPa): 0.00060448±3.5376e-05
Hertz. r-squared: 0.92949
Dimitriadis. Value of indentation at contact point (nm): 0.0020459±0.6372
Dimitriadis. Value of deflection at contact point (nm): 0.00022441±0.062669
Dimitriadis. Value of Youngs Modulus (GPa): 0.00051711±3.3673e-05
Dimitriadis. r-squared: 0.93012
z.s.f = z piezo on substrate (forward) (nm); p.s.f = photodiode on substrate (forward) (V)
z.p.f = z piezo on particle (forward) (nm); p.p.f = photodiode on particle (forward) (V)
i.p.f = indentation on particle (forward) (nm); d.p.f = deflection on particle (forward) (nm); i.p.f.z = indentation on particle (forward) (nm); d.p
d.f.i = fitted data indentation(nm); d.f.d = fitted data deflection(nm)
H.fit = fitting Hertz model (nm); D.fit = fitting Dimitriadis model (nm)
 klever          v/nm          r_sqrsubs          Poisson             alpha0             beta0          tip_radius          sam_height          eff_radius
              0.0554             0.0389             1.0000             0.2000            -1.1278             0.3220            15.0000            63.9320            10.2093
  H_ind              SE             H_def              SE             D_ind              SE             D_def              SE
         0.0739             0.5973            -0.0263             0.0632             0.0020             0.6372             0.0002             0.0627
 H_Young              SE          D_Young              SE
    6.0448e-04    3.5376e-05    5.1711e-04    3.3673e-05
    z.s.f          p.s.f          z.p.f          p.p.f          i.p.f          d.p.f          i.p.f.z          d.p.f.z          d.f.i          d.f.d          H.fit          D.f
         -0.0000        -2.2849        -0.0000        -2.3224        59.7234       -59.7234       -31.1115        -0.1412           NaN           NaN        -0.0263
          0.1957        -2.3138         0.1957        -2.3145        59.7151       -59.5194       -31.1198         0.0629           NaN           NaN        -0.0263
          0.3914        -2.2827         0.3914        -2.3041        59.6439       -59.2525       -31.1909         0.3297           NaN           NaN        -0.0263
          0.5871        -2.2809         0.5871        -2.3206        60.2634       -59.6763       -30.5715        -0.0941           NaN           NaN        -0.0263
          0.7828        -2.2955         0.7828        -2.2980        59.8783       -59.0956       -30.9565         0.4867           NaN           NaN        -0.0263
          0.9785        -2.2958         0.9785        -2.3184        60.5999       -59.6214       -30.2350        -0.0391           NaN           NaN        -0.0263
          1.1742        -2.2809         1.1742        -2.3236        60.9290       -59.7548       -29.9059        -0.1726           NaN           NaN        -0.0263
```

Figure A.6: Screenshot of the output text file of the MATLAB program for non-linear indentation analysis.

A.4 Work-indentation analysis

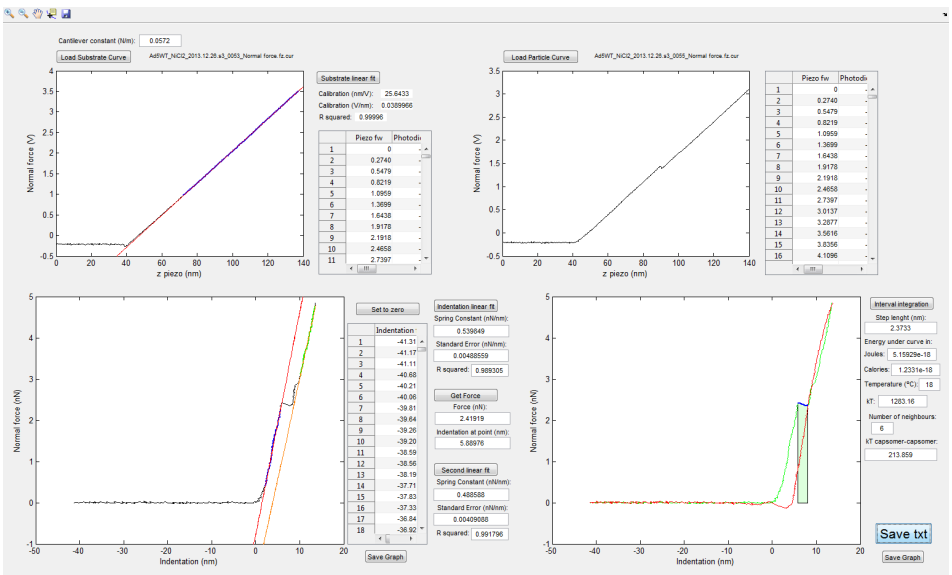

Figure A.7: Screenshot of the MATLAB program for work-indentation analysis.

This program was developed to compute the supplied energy required to remove a hexon from indentation curves on the viral particles (section 5.7). The program (figure A.7) is the same as the one presented in appendix A.1. An extra panel allows selecting two points to determine the region of the curve for the integration to compute the supplied work (only on the forward curve). The user can enter some parameters such as temperature and number of capsomers neighboring the broken one, to compute the capsomer-capsomer interaction energy. A text file can be saved with the input and output data (figure A.8).

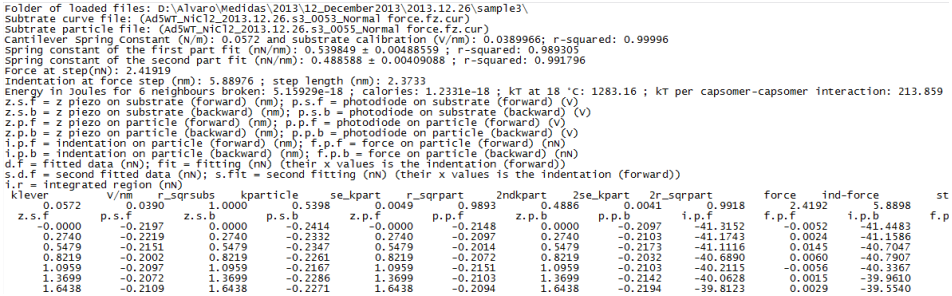

```
Folder of loaded files: D:\Alvaro\Medidas\2013\12_December2013\2013.12.26\sample3\
Subtrate curve file: (Ad5WT_NiCl2_2013.12.26.s3_0053_Normal force.fz.cur)
Subtrate particle file: (Ad5WT_NiCl2_2013.12.26.s3_0055_Normal force.fz.cur)
Cantilever Spring Constant (N/m): 0.0572 and substrate calibration (V/nm): 0.0389966; r-squared: 0.99996
Spring constant of the first part fit (nN/nm): 0.539849 ± 0.00488559 ; r-squared: 0.989305
Spring constant of the second part fit (nN/nm): 0.488588 ± 0.00409088 ; r-squared: 0.991796
Force at step(nN): 2.41919
Indentation at force step (nm): 5.88976 ; step length (nm): 2.3733
Energy in Joules for 6 neighbours broken: 5.15929e-18 ; calories: 1.2331e-18 ; kT at 18 'C: 1283.16 ; kT per capsomer-capsomer interaction: 213.859
z.s.f = z piezo on substrate (forward) (nm); p.s.f = photodiode on substrate (forward) (V)
z.s.b = z piezo on substrate (backward) (nm); p.s.b = photodiode on substrate (backward) (V)
z.p.f = z piezo on particle (forward) (nm); p.p.f = photodiode on particle (forward) (V)
z.p.b = z piezo on particle (backward) (nm); p.p.b = photodiode on particle (backward) (V)
i.p.f = indentation on particle (forward) (nm); f.p.f = force on particle (forward) (nN)
i.p.b = indentation on particle (backward) (nm); f.p.b = force on particle (backward) (nN)
d.f = fitted data (nN); fit = fitting (nN) (their x values is the indentation (forward))
s.d.f = second fitted data (nN); s.fit = second fitting (nN) (their x values is the indentation (forward))
i.r = integrated region (nN)
 klever          V/nm     r_sqrsubs     kparticle     se_kpart     r_sqrpart     2ndkpart     2se_kpart   2r_sqrpart        force     ind-force          st
      0.0572      0.0390        1.0000        0.5398       0.0049        0.9893       0.4886       0.0041       0.9918       2.4192        5.8898
  z.s.f        p.s.f        z.s.b        p.s.b        z.p.f        p.p.f        z.p.b        p.p.b        i.p.f        f.p.f        i.p.b        f.p
     -0.0000      -0.2197       0.0000       -0.2414      -0.0000      -0.2148       0.0000       -0.2097     -41.3152       -0.0052     -41.4483
      0.2740      -0.2219       0.2740       -0.2332       0.2740      -0.2097       0.2740       -0.2103     -41.1743        0.0024     -41.1586
      0.5479      -0.2151       0.5479       -0.2347       0.5479      -0.2014       0.5479       -0.2173     -41.1116        0.0145     -40.7047
      0.8219      -0.2002       0.8219       -0.2261       0.8219      -0.2072       0.8219       -0.2032     -40.6890        0.0060     -40.7907
      1.0959      -0.2097       1.0959       -0.2167       1.0959      -0.2151       1.0959       -0.2103     -40.2115       -0.0056     -40.3367
      1.3699      -0.2072       1.3699       -0.2286       1.3699      -0.2103       1.3699       -0.2142     -40.0628        0.0015     -39.9610
      1.6438      -0.2109       1.6438       -0.2271       1.6438      -0.2094       1.6438       -0.2194     -39.8123        0.0029     -39.5540
```

Figure A.8: Screenshot of the output text file of the MATLAB program for work-indentation analysis.

Bibliography

[1] K. Pearson (1892) Chap. The classification of the sciences., pp. 441–475.

[2] R. Glaser, in *Biophysics* (Springer Berlin Heidelberg, 2012) pp. 1–4.

[3] Y. G. Kuznetsov, S. B. Larson, J. Day, A. Greenwood, and A. McPherson, Virology **284**, 223 (2001).

[4] M. Legendre, J. Bartoli, L. Shmakova, S. Jeudy, K. Labadie, A. Adrait, M. Lescot, O. Poirot, L. Bertaux, C. Bruley, Y. Couté, E. Rivkina, C. Abergel, and J.-M. Claverie, Proc Natl Acad Sci U S A **111**, 4274 (2014).

[5] A. Lustig and A. J. Levine, Journal of virology **66**, 4629 (1992).

[6] M. Breitbart and F. Rohwer, Trends in Microbiology **13**, 278 (2005).

[7] C. A. Suttle, Nature **437**, 356 (2005).

[8] T. Douglas and M. Young, Science **312**, 873 (2006).

[9] M. G. Mateu, in *Structure and Physics of Viruses*, Subcellular Biochemistry, Vol. 68, edited by M. G. Mateu (Springer Netherlands, 2013) pp. 3–51.

[10] W. Roos, R. Bruinsma, and G. Wuite, Nature Physics **6**, 733 (2010).

[11] U. F. Greber, Biophys J **106**, 2317 (2014).

[12] W. P. Rowe, R. J. Huebner, L. K. Gilmore, R. H. Parrott, and T. G. Ward, Proc Soc Exp Biol Med **84**, 570 (1953).

[13] tagkey2012125, in *Virus Taxonomy*, edited by A. M. King, M. J. Adams, E. B. Carstens, and E. J. Lefkowitz (Elsevier, San Diego, 2012) pp. 125 – 141.

[14] A. M. Leen and C. M. Rooney, British Journal of Haematology **128**, 135 (2005).

[15] M. A. F. V. Gonçalves and A. A. F. de Vries, Rev Med Virol **16**, 167 (2006).

[16] R. Valentine and H. Pereira, Journal of Molecular Biology **13**, 13 (1965).

[17] J. R. Castón and J. L. Carrascosa, in *Structure and Physics of Viruses*, Subcellular Biochemistry, Vol. 68, edited by M. G. Mateu (Springer Netherlands, 2013) pp. 53–75.

[18] W. F. Mangel and C. San Martín, Viruses **6**, 4536 (2014).

[19] C. San Martín, Viruses **4**, 847 (2012).

[20] H. Liu, L. Jin, S. B. S. Koh, I. Atanasov, S. Schein, L. Wu, and Z. H. Zhou, Science **329**, 1038 (2010).

[21] V. S. Reddy, S. K. Natchiar, P. L. Stewart, and G. R. Nemerow, Science **329**, 1071 (2010).

[22] R. M. Burnett, M. G. Grütter, and J. L. White, Journal of Molecular Biology **185**, 105 (1985).

[23] C. Zubieta, G. Schoehn, J. Chroboczek, and S. Cusack, Mol Cell **17**, 121 (2005).

[24] M. J. van Raaij, A. Mitraki, G. Lavigne, and S. Cusack, Nature **401**, 935 (1999).

[25] L. Prage, U. Pettersson, S. Höglund, K. Lonberg-Holm, and L. Philipson, Virology **42**, 341 (1970).

[26] A. J. Pérez-Berná, R. Marabini, S. H. W. Scheres, R. Menéndez-Conejero, I. P. Dmitriev, D. T. Curiel, W. F. Mangel, S. J. Flint, and C. San Martín, J Mol Biol **392**, 547 (2009).

[27] R. Martinez, P. Schellenberger, D. Vasishtan, C. Aknin, S. Austin, D. Dacheux, F. Rayne, A. Siebert, Z. Ruzsics, K. Gruenewald, and H. Wodrich, J Virol **89**, 2121 (2015).

[28] A. N. Giberson, A. R. Davidson, and R. J. Parks, Nucleic Acids Res **40**, 2369 (2012).

[29] J. van Oostrum and R. M. Burnett, J Virol **56**, 439 (1985).

[30] M. Benevento, S. Di Palma, J. Snijder, C. L. Moyer, V. S. Reddy, G. R. Nemerow, and A. J. R. Heck, J Biol Chem **289**, 11421 (2014).

[31] A. J. Pérez-Berná, S. Marion, F. J. Chichón, J. J. Fernández, D. C. Winkler, J. L. Carrascosa, A. C. Steven, A. Šiber, and C. San Martín, Nucleic Acids Res **43**, 4274 (2015).

[32] M. A. Mirza and J. Weber, Biochim Biophys Acta **696**, 76 (1982).

[33] M. E. Vayda, A. E. Rogers, and S. J. Flint, Nucleic Acids Res **11**, 441 (1983).

[34] G. Saper, S. Kler, R. Asor, A. Oppenheim, U. Raviv, and D. Harries, Nucleic Acids Res **41**, 1569 (2013).

[35] J. B. Christensen, S. A. Byrd, A. K. Walker, J. R. Strahler, P. C. Andrews, and M. J. Imperiale, J Virol **82**, 9086 (2008).

[36] G. N. Condezo, R. Marabini, S. Ayora, J. M. Carazo, R. Alba, M. Chillón, and C. San Martín, J Virol **89**, 9653 (2015).

[37] A. J. Pérez-Berná, W. F. Mangel, W. J. McGrath, V. Graziano, J. Flint, and C. San Martín, J Virol **88**, 1513 (2014).

[38] U. F. Greber, M. Willetts, P. Webster, and A. Helenius, Cell **75**, 477 (1993).

[39] S. J. Flint, L. W. Enquist, V. R. Racaniello, and A. M. Skalka, eds., *Principles of Virology, Third Edition BUNDLE* (American Society of Microbiology, 2009).

[40] C. J. Burckhardt, M. Suomalainen, P. Schoenenberger, K. Boucke, S. Hemmi, and U. F. Greber, Cell Host Microbe **10**, 105 (2011).

[41] M. Y. Nakano, K. Boucke, M. Suomalainen, R. P. Stidwill, and U. F. Greber, J Virol **74**, 7085 (2000).

[42] C. Y. Chiu, P. Mathias, G. R. Nemerow, and P. L. Stewart, J Virol **73**, 6759 (1999).

[43] S. Lindert, M. Silvestry, T.-M. Mullen, G. R. Nemerow, and P. L. Stewart, J Virol **83**, 11491 (2009).

[44] S. Luisoni, M. Suomalainen, K. Boucke, L. B. Tanner, M. R. Wenk, X. L. Guan, M. Grzybek, Ü. Coskun, and U. F. Greber, Cell Host Microbe **18**, 75 (2015).

[45] M. Gastaldelli, N. Imelli, K. Boucke, B. Amstutz, O. Meier, and U. F. Greber, Traffic **9**, 2265 (2008).

[46] M. Suomalainen, S. Luisoni, K. Boucke, S. Bianchi, D. A. Engel, and U. F. Greber, J Virol **87**, 12367 (2013).

[47] C. M. Wiethoff, H. Wodrich, L. Gerace, and G. R. Nemerow, J Virol **79**, 1992 (2005).

[48] K. H. Bremner, J. Scherer, J. Yi, M. Vershinin, S. P. Gross, and R. B. Vallee, Cell Host Microbe **6**, 523 (2009).

[49] I.-H. Wang, M. Suomalainen, V. Andriasyan, S. Kilcher, J. Mercer, A. Neef, N. W. Luedtke, and U. F. Greber, Cell Host Microbe **14**, 468 (2013).

[50] S. Strunze, M. F. Engelke, I.-H. Wang, D. Puntener, K. Boucke, S. Schleich, M. Way, P. Schoenenberger, C. J. Burckhardt, and U. F. Greber, Cell Host Microbe **10**, 210 (2011).

[51] J. M. Weber, Curr Top Microbiol Immunol **199 (Pt 1)**, 227 (1995).

[52] D. Veesler and J. E. Johnson, Annu Rev Biophys **41**, 473 (2012).

[53] J. E. Johnson, Curr Opin Struct Biol **20**, 210 (2010).

[54] M. Silvestry, S. Lindert, J. G. Smith, O. Maier, C. M. Wiethoff, G. R. Nemerow, and P. L. Stewart, J Virol **83**, 7375 (2009).

[55] U. F. Greber, P. Webster, J. Weber, and A. Helenius, EMBO J **15**, 1766 (1996).

[56] M. Cotten and J. M. Weber, Virology **213**, 494 (1995).

[57] A. J. Pérez-Berná, A. Ortega-Esteban, R. Menéndez-Conejero, D. C. Winkler, M. Menéndez, A. C. Steven, S. J. Flint, P. J. de Pablo, and C. San Martín, J Biol Chem **287**, 31582 (2012).

[58] M. Castellanos, R. Pérez, C. Carrasco, M. Hernando-Pérez, J. Gómez-Herrero, P. J. de Pablo, and M. G. Mateu, Proc Natl Acad Sci U S A **109**, 12028 (2012).

[59] B. Saha, C. M. Wong, and R. J. Parks, Viruses **6**, 3563 (2014).

[60] M. Feiss, R. Fisher, M. Crayton, and C. Egner, Virology **77**, 281 (1977).

[61] A. M. Baró, R. Miranda, J. Alamán, N. García, G. Binnig, H. Rohrer, C. Gerber, and J. L. Carrascosa, Nature **315**, 253 (1985).

[62] C. Carrasco, A. Carreira, I. A. T. Schaap, P. A. Serena, J. Gómez-Herrero, M. G. Mateu, and P. J. de Pablo, Proc Natl Acad Sci U S A **103**, 13706 (2006).

[63] C. Carrasco, M. Castellanos, P. J. de Pablo, and M. G. Mateu, Proc Natl Acad Sci U S A **105**, 4150 (2008).

[64] I. Ivanovska, G. Wuite, B. Jönsson, and A. Evilevitch, Proc Natl Acad Sci U S A **104**, 9603 (2007).

[65] M. Hernando-Pérez, R. Miranda, M. Aznar, J. L. Carrascosa, I. A. T. Schaap, D. Reguera, and P. J. de Pablo, Small **8**, 2366 (2012).

[66] W. H. Roos, K. Radtke, E. Kniesmeijer, H. Geertsema, B. Sodeik, and G. J. L. Wuite, Proc Natl Acad Sci U S A **106**, 9673 (2009).

[67] G. Binnig, H. Rohrer, C. Gerber, and E. Weibel, Phys. Rev. Lett. **49**, 57 (1982).

[68] G. Binnig, H. Rohrer, C. Gerber, and E. Weibel, Applied Physics Letters **40**, 178 (1982).

[69] G. Binnig, C. F. Quate, and C. Gerber, Phys. Rev. Lett. **56**, 930 (1986).

[70] G. Meyer and N. M. Amer, Applied physics letters **53**, 1045 (1988).

[71] I. Horcas, R. Fernández, J. M. Gómez-Rodríguez, J. Colchero, J. Gómez-Herrero, and A. M. Baro, Rev Sci Instrum **78**, 013705 (2007).

[72] P. de Pablo, in *Structure and Physics of Viruses*, Subcellular Biochemistry, Vol. 68, edited by M. G. Mateu (Springer Netherlands, 2013) pp. 247–271.

[73] N. Burnham, X. Chen, C. Hodges, G. Matei, E. Thoreson, C. Roberts, M. Davies, and S. Tendler, Nanotechnology **14**, 1 (2003).

[74] J. E. Sader, J. W. M. Chon, and P. Mulvaney, Review of Scientific Instruments **70**, 3967 (1999).

[75] O. Marti, B. Drake, and P. Hansma, Applied Physics Letters **51**, 484 (1987).

[76] B. Drake, C. B. Prater, A. L. Weisenhorn, S. A. Gould, T. R. Albrecht, C. F. Quate, D. S. Cannell, H. G. Hansma, and P. K. Hansma, Science **243**, 1586 (1989).

[77] J. N. Israelachvili, *Intermolecular and surface forces: revised third edition* (Academic press, 2011).

[78] A. L. Weisenhorn, P. Maivald, H.-J. Butt, and P. K. Hansma, Phys. Rev. B **45**, 11226 (1992).

[79] R. García and R. Pérez, Surface Science Reports **47**, 197 (2002).

[80] F. Ohnesorge and G. Binnig, Science **260**, 1451 (1993).

[81] H. J. Butt, Biophys J **60**, 1438 (1991).

[82] H.-J. Butt, M. Jaschke, and W. Ducker, Bioelectrochemistry and Bioenergetics **38**, 191 (1995).

[83] E. T. Herruzo, H. Asakawa, T. Fukuma, and R. Garcia, Nanoscale **5**, 2678 (2013).

[84] V. A. Parsegian and D. Gingell, Biophys J **12**, 1192 (1972).

[85] M. E. Fuentes Pérez, *Caracterización de ácidos nucleicos, proteínas e interacciones proteína:proteína y DNA:proteína mediante microscopía de fuerzas atómicas*, Ph.D. thesis, UAM. Departamento de Física de la Materia Condensada; CSIC. Centro Nacional de Biotecnología (2014).

[86] L. Martínez, M. Tello, M. Díaz, E. Román, R. Garcia, and Y. Huttel, Rev Sci Instrum **82**, 023710 (2011).

[87] J. S. Villarrubia, Journal of Research of the National Institute of Standards and Technology **102**, 425 (1997).

[88] H.-J. Butt and M. Jaschke, Nanotechnology **6**, 1 (1995).

[89] J. Sotres, A. Lostao, C. Gómez-Moreno, and A. M. Baró, Ultramicroscopy **107**, 1207 (2007).

[90] F. Moreno-Herrero, J. Colchero, J. Gómez-Herrero, and A. M. Baró, Phys. Rev. E **69**, 031915 (2004).

[91] A. M. Baró and R. G. Reifenberger, *Atomic Force Microscopy in Liquid: Biological Applications* (John Wiley & Sons, 2012).

[92] J. M. Neumeister and W. A. Ducker, Review of Scientific Instruments **65**, 2527 (1994).

[93] R. W. Carpick and M. Salmeron, Chem Rev **97**, 1163 (1997).

[94] D. Choi, W. Hwang, and E. Yoon, Journal of microscopy **228**, 190 (2007).

[95] D. J. Müller, F. A. Schabert, G. Büldt, and A. Engel, Biophys J **68**, 1681 (1995).

[96] D. J. Müller, A. Engel, J. L. Carrascosa, and M. Vélez, EMBO J **16**, 2547 (1997).

[97] T. Walz, P. Tittmann, K. H. Fuchs, D. J. Müller, B. L. Smith, P. Agre, H. Gross, and A. Engel, Journal of Molecular Biology **264**, 907 (1996).

[98] Y. Martin, C. C. Williams, and H. K. Wickramasinghe, Journal of Applied Physics **61**, 4723 (1987).

[99] J. Chen, R. K. Workman, D. Sarid, and R. Hoper, Nanotechnology **5**, 199 (1994).

[100] R. García and A. San Paulo, Phys. Rev. B **60**, 4961 (1999).

[101] P. J. de Pablo, J. Colchero, J. Gómez-Herrero, and A. M. Baró, Applied Physics Letters **73**, 3300 (1998).

[102] A. Rosa-Zeiser, E. Weilandt, S. Hild, and O. Marti, Measurement Science and Technology **8**, 1333 (1997).

[103] P. J. de Pablo, J. Colchero, J. Gomez-Herrero, A. M. Baro, D. M. Schaefer, S. Howell, B. Walsh, and R. Reifenberger, The Journal of Adhesion **71**, 339 (1999).

[104] K. O. van der Werf, C. A. J. Putman, B. G. de Grooth, and J. Greve, Applied Physics Letters **65**, 1195 (1994).

[105] A. Ortega-Esteban, I. Horcas, M. Hernando-Pérez, P. Ares, A. J. Pérez-Berná, C. San Martín, J. L. Carrascosa, P. J. de Pablo, and J. Gómez-Herrero, Ultramicroscopy **114**, 56 (2012).

[106] J. Rösler, M. Bäker, and H. Harders, in *Mechanical Behaviour of Engineering Materials* (Springer Berlin Heidelberg, 2007) pp. 31–62.

[107] I. L. Ivanovska, P. J. de Pablo, B. Ibarra, G. Sgalari, F. C. MacKintosh, J. L. Carrascosa, C. F. Schmidt, and G. J. L. Wuite, Proc Natl Acad Sci U S A **101**, 7600 (2004).

[108] D. Badia-Martinez, H. Oksanen, D. Stuart, and N. Abrescia, in *Structure and Physics of Viruses*, Subcellular Biochemistry, Vol. 68, edited by M. G. Mateu (Springer Netherlands, 2013) pp. 203–246.

[109] J. D. Watson and F. H. Crick, Nature **171**, 737 (1953).

[110] Y. G. Kuznetsov and A. McPherson, Microbiol Mol Biol Rev **75**, 268 (2011).

[111] N. Verdaguer, D. Garriga, and I. Fita, in *Structure and Physics of Viruses*, Subcellular Biochemistry, Vol. 68, edited by M. G. Mateu (Springer Netherlands, 2013) pp. 117–144.

[112] A. Foster and W. Hofer, in *Scanning Probe Microscopy*, NanoScience and Technology (Springer New York, 2006) pp. 11–36.

[113] M. Hernando-Pérez, A. X. Cartagena, A. L. Božič, P. J. Carrillo, C. San Martín, M. G. Mateu, A. Raman, R. Podgornik, and P. de Pablo, Nanoscale (2015), 10.1039/C5NR04274G.

[114] K. El Kirat, I. Burton, V. Dupres, and Y. F. Dufrene, J Microsc **218**, 199 (2005).

[115] D. C. Cullen and C. R. Lowe, Journal of colloid and interface science **166**, 102 (1994).

[116] Gun'ko, Vedamuthu, Henderson, and Blitz, J Colloid Interface Sci **228**, 157 (2000).

[117] D. J. Müller, M. Amrein, and A. Engel, J Struct Biol **119**, 172 (1997).

[118] S. Bailey, Reviews in Mineralogy and Geochemistry **13**, 13 (1984).

[119] G. Raffaini and F. Ganazzoli, Langmuir **26**, 5679 (2010).

[120] S. Wei and T. A. Knotts, The Journal of Chemical Physics **139**, 095102 (2013).

[121] Y. Mu, Phys. Rev. E **84**, 031906 (2011).

[122] J. Snijder, V. S. Reddy, E. R. May, W. H. Roos, G. R. Nemerow, and G. J. L. Wuite, J Virol **87**, 2756 (2013).

[123] D. M. Shayakhmetov and A. Lieber, J Virol **74**, 10274 (2000).

[124] F. Kienberger, R. Zhu, C. Rankl, H. J. Gruber, D. Blaas, and P. Hinterdorfer, in *Single Molecule Tools, Part B:Super-Resolution, Particle Tracking, Multiparameter, and Force Based Methods*, Methods in Enzymology, Vol. 475, edited by N. G. Walter (Academic Press, 2010) pp. 515 – 539.

[125] J. Sotres and A. M. Baró, Biophys J **98**, 1995 (2010).

[126] C. Carrasco, A. Luque, M. Hernando-Pérez, R. Miranda, J. L. Carrascosa, P. A. Serena, M. de Ridder, A. Raman, J. Gómez-Herrero, I. A. T. Schaap, D. Reguera, and P. J. de Pablo, Biophys J **100**, 1100 (2011).

[127] L. Fumagalli, D. Esteban-Ferrer, A. Cuervo, J. L. Carrascosa, and G. Gomila, Nat Mater **11**, 808 (2012).

[128] D. J. Müller and Y. F. Dufrêne, Nat Nanotechnol **3**, 261 (2008).

[129] P. J. de Pablo, I. A. T. Schaap, F. C. MacKintosh, and C. F. Schmidt, Phys Rev Lett **91**, 098101 (2003).

[130] L. D. Landau and E. Lifshitz, *Theory of Elasticity, vol. 7*, Vol. 3 (Elsevier New York, 1986) p. 109.

[131] I. A. T. Schaap, C. Carrasco, P. J. de Pablo, F. C. MacKintosh, and C. F. Schmidt, Biophys J **91**, 1521 (2006).

[132] P. de Pablo and M. Mateu, in *Structure and Physics of Viruses*, Subcellular Biochemistry, Vol. 68, edited by M. G. Mateu (Springer Netherlands, 2013) pp. 519–551.

[133] A. Llauró, E. Coppari, F. Imperatori, A. R. Bizzarri, J. R. Castón, L. Santi, S. Cannistraro, and P. J. de Pablo, Biophys J **109**, 390 (2015).

[134] M. Baclayon, G. K. Shoemaker, C. Uetrecht, S. E. Crawford, M. K. Estes, B. V. V. Prasad, A. J. R. Heck, G. J. L. Wuite, and W. H. Roos, Nano Lett **11**, 4865 (2011).

[135] W. H. Roos, I. Gertsman, E. R. May, C. L. Brooks, 3rd, J. E. Johnson, and G. J. L. Wuite, Proc Natl Acad Sci U S A **109**, 2342 (2012).

[136] W. M. Gelbart and C. M. Knobler, Science **323**, 1682 (2009).

[137] J. Carter and V. A. Saunders, *Virology: principles and applications* (John Wiley & Sons, 2007).

[138] A. Zlotnick, Virology **315**, 269 (2003).

[139] R. Zandi, P. van der Schoot, D. Reguera, W. Kegel, and H. Reiss, Biophys J **90**, 1939 (2006).

[140] M. Chow, R. Basavappa, and J. M. Hogle, *Structural biology of viruses*, edited by W. Chiu, R. M. Burnett, and R. L. Garcea (Oxford University Press, Oxford, UK, 1997).

[141] M. Cyrklaff, A. Linaroudis, M. Boicu, P. Chlanda, W. Baumeister, G. Griffiths, and J. Krijnse-Locker, PLoS One **2**, e420 (2007).

[142] X. Qiu, PLoS One **7**, e39793 (2012).

[143] C. Xiao, Y. G. Kuznetsov, S. Sun, S. L. Hafenstein, V. A. Kostyuchenko, P. R. Chipman, M. Suzan-Monti, D. Raoult, A. McPherson, and M. G. Rossmann, PLoS Biol **7**, e92 (2009).

[144] M. Castellanos, R. Pérez, P. J. P. Carrillo, P. J. de Pablo, and M. G. Mateu, Biophys J **102**, 2615 (2012).

[145] I. L. Ivanovska, R. Miranda, J. L. Carrascosa, G. J. L. Wuite, and C. F. Schmidt, Proc Natl Acad Sci U S A **108**, 12611 (2011).

[146] W. S. Klug, R. F. Bruinsma, J.-P. Michel, C. M. Knobler, I. L. Ivanovska, C. F. Schmidt, and G. J. L. Wuite, Phys. Rev. Lett. **97**, 228101 (2006).

[147] D. Puntener, M. F. Engelke, Z. Ruzsics, S. Strunze, C. Wilhelm, and U. F. Greber, J Virol **85**, 481 (2011).

[148] U. F. Greber, M. Suomalainen, R. P. Stidwill, K. Boucke, M. W. Ebersold, and A. Helenius, EMBO J **16**, 5998 (1997).

[149] J. Weber, J Virol **17**, 462 (1976).

[150] J. M. Weber, *Adenoviruses: basic biology to gene therapy*, edited by P. Seth (RG Landes Company Austin, 1999).

[151] S. H. W. Scheres, R. Núñez-Ramírez, C. O. S. Sorzano, J. M. Carazo, and R. Marabini, Nat Protoc **3**, 977 (2008).

[152] W. Schütz, Engineering Fracture Mechanics **54**, 263 (1996).

[153] J. J. Rux and R. M. Burnett, Mol Ther **1**, 18 (2000).

[154] S. Singh and A. Zlotnick, J Biol Chem **278**, 18249 (2003).

[155] R. Zandi and D. Reguera, Phys Rev E Stat Nonlin Soft Matter Phys **72**, 021917 (2005).

[156] M. Hernando-Pérez, S. Lambert, E. Nakatani-Webster, C. E. Catalano, and P. J. de Pablo, Nat Commun **5**, 4520 (2014).

[157] J. Rösler, M. Bäker, and H. Harders, in *Mechanical Behaviour of Engineering Materials* (Springer Berlin Heidelberg, 2007) pp. 333–382.

[158] L. Redondo-Morata, M. I. Giannotti, and F. Sanz, Langmuir **28**, 6403 (2012).

[159] A. Ortega-Esteban, A. J. Pérez-Berná, R. Menéndez-Conejero, S. J. Flint, C. San Martín, and P. J. de Pablo, Sci Rep **3**, 1434 (2013).

[160] V. A. Bloomfield, D. M. Crothers, I. Tinoco, and J. E. Hearst, *Nucleic acids: structures, properties, and functions*, Vol. 128 (University Science Books, 2000).

[161] D. W. Bauer, J. B. Huffman, F. L. Homa, and A. Evilevitch, J Am Chem Soc **135**, 11216 (2013).

[162] J. E. Germond, B. Hirt, P. Oudet, M. Gross-Bellark, and P. Chambon, Proc Natl Acad Sci U S A **72**, 1843 (1975).

[163] P. C. Blainey, V. Graziano, A. J. Pérez-Berná, W. J. McGrath, S. J. Flint, C. San Martín, X. S. Xie, and W. F. Mangel, J Biol Chem **288**, 2092 (2013).

[164] E. K. Dimitriadis, F. Horkay, J. Maresca, B. Kachar, and R. S. Chadwick, Biophys J **82**, 2798 (2002).

[165] I. N. Sneddon, International Journal of Engineering Science **3**, 47 (1965).

[166] B. Houchmandzadeh, J. F. Marko, D. Chatenay, and A. Libchaber, J Cell Biol **139**, 1 (1997).

[167] A. Khan, J. Philip, and P. Hess, Journal of Applied Physics **95**, 1667 (2004).

[168] A. Evilevitch, L. Lavelle, C. M. Knobler, E. Raspaud, and W. M. Gelbart, Proc Natl Acad Sci U S A **100**, 9292 (2003).

[169] U. Sae-Ueng, D. Li, X. Zuo, J. B. Huffman, F. L. Homa, D. Rau, and A. Evilevitch, Nat Chem Biol **10**, 861 (2014).

[170] J. Snijder, C. Uetrecht, R. J. Rose, R. Sanchez-Eugenia, G. A. Marti, J. Agirre, D. M. A. Guérin, G. J. L. Wuite, A. J. R. Heck, and W. H. Roos, Nat Chem **5**, 502 (2013).

[171] M. Hernando-Pérez, E. Pascual, M. Aznar, A. Ionel, J. R. Castón, A. Luque, J. L. Carrascosa, D. Reguera, and P. J. de Pablo, Nanoscale **6**, 2702 (2014).

[172] A. Mazumder, T. Roopa, A. Basu, L. Mahadevan, and G. V. Shivashankar, Biophys J **95**, 3028 (2008).

[173] X. Qiu, D. C. Rau, V. A. Parsegian, L. T. Fang, C. M. Knobler, and W. M. Gelbart, Phys Rev Lett **106**, 028102 (2011).

[174] A. Leforestier and F. Livolant, Proc Natl Acad Sci U S A **106**, 9157 (2009).

[175] M. S. Luijsterburg, M. F. White, R. van Driel, and R. T. Dame, Crit Rev Biochem Mol Biol **43**, 393 (2008).

[176] D. Vella, A. Ajdari, A. Vaziri, and A. Boudaoud, J R Soc Interface **9**, 448 (2012).

[177] J. Kindt, S. Tzlil, A. Ben-Shaul, and W. M. Gelbart, Proc Natl Acad Sci U S A **98**, 13671 (2001).

[178] P. K. Purohit, J. Kondev, and R. Phillips, Proc Natl Acad Sci U S A **100**, 3173 (2003).

[179] J. Mateos-Langerak, M. Bohn, W. de Leeuw, O. Giromus, E. M. M. Manders, P. J. Verschure, M. H. G. Indemans, H. J. Gierman, D. W. Heermann, R. van Driel, and S. Goetze, Proc Natl Acad Sci U S A **106**, 3812 (2009).

[180] M. Tark-Dame, R. van Driel, and D. W. Heermann, J Cell Sci **124**, 839 (2011).

[181] M. Goulian and S. T. Milner, Journal de Physique II **6**, 543 (1996).

[182] K. Bystricky, P. Heun, L. Gehlen, J. Langowski, and S. M. Gasser, Proc Natl Acad Sci U S A **101**, 16495 (2004).

[183] C. G. Baumann, V. A. Bloomfield, S. B. Smith, C. Bustamante, M. D. Wang, and S. M. Block, Biophys J **78**, 1965 (2000).

[184] M. Aznar, A. Luque, and D. Reguera, Phys Biol **9**, 036003 (2012).

[185] M. A. Croyle, X. Cheng, and J. M. Wilson, Gene Ther **8**, 1281 (2001).

[186] W. S. Klug, W. H. Roos, and G. J. L. Wuite, Phys. Rev. Lett. **109**, 168104 (2012).

[187] D. E. Smith, S. J. Tans, S. B. Smith, S. Grimes, D. L. Anderson, and C. Bustamante, Nature **413**, 748 (2001).

[188] P. Grayson, M. M. Inamdar, P. K. Purohit, R. Phillips, A. Evilevitch, W. M. Gelbart, and C. M. Knobler, Biophys J **88**, 230A (2005).

[189] W. W. Newcomb, F. P. Booy, and J. C. Brown, J Mol Biol **370**, 633 (2007).

[190] M. F. Engelke, C. J. Burckhardt, M. K. Morf, and U. F. Greber, Viruses **3**, 233 (2011).

[191] M. Suomalainen, M. Y. Nakano, S. Keller, K. Boucke, R. P. Stidwill, and U. F. Greber, J Cell Biol **144**, 657 (1999).

[192] D. T. Brown, M. Westphal, B. T. Burlingham, U. Winterhoff, and W. Doerfler, J Virol **16**, 366 (1975).

[193] A. Sarkar, R. B. Robertson, and J. M. Fernandez, Proc Natl Acad Sci U S A **101**, 12882 (2004).

[194] J. C. Cordova, D. K. Das, H. W. Manning, and M. J. Lang, Curr Opin Struct Biol **28**, 142 (2014).

[195] M. S. Z. Kellermayer, A. Karsai, A. Kengyel, A. Nagy, P. Bianco, T. Huber, A. Kulcsár, C. Niedetzky, R. Proksch, and L. Grama, Biophys J **91**, 2665 (2006).

[196] A. Llauró, P. Guerra, N. Irigoyen, J. F. Rodríguez, N. Verdaguer, and P. J. de Pablo, Biophys J **106**, 687 (2014).

[197] H. S. Rye, S. Yue, D. E. Wemmer, M. A. Quesada, R. P. Haugland, R. A. Mathies, and A. N. Glazer, Nucleic Acids Res **20**, 2803 (1992).

[198] A. Gaiduk, R. Kühnemuth, M. Antonik, and C. A. M. Seidel, Chemphyschem **6**, 976 (2005).

[199] K. Bodensiek, *Combining force and fluorescence microscopy for the manipulation and detection of single cells, viruses, and proteins*, Ph.D. thesis, Göttingen Graduate School for Neurosciences, Biophysics and Molecular Biosciences. Georg-August-Universität Göttingen (2014).

[200] N. A. Issa and R. Guckenberger, Opt. Express **15**, 12131 (2007).

[201] N. Mauser and A. Hartschuh, Chem. Soc. Rev. **43**, 1248 (2014).

[202] B. Akerman and E. Tuite, Nucleic Acids Res **24**, 1080 (1996).

[203] L. C. Trotman, N. Mosberger, M. Fornerod, R. P. Stidwill, and U. F. Greber, Nat Cell Biol **3**, 1092 (2001).

[204] M. Lyon, Y. Chardonnet, and S. Dales, Virology **87**, 81 (1978).

[205] V. Lütschg, K. Boucke, S. Hemmi, and U. F. Greber, Nat Commun **2**, 391 (2011).

[206] N. Wolfrum and U. F. Greber, Cell Microbiol **15**, 53 (2013).

[207] K. Svoboda, C. F. Schmidt, B. J. Schnapp, and S. M. Block, Nature **365**, 721 (1993).

[208] W. W. Newcomb, S. K. Cockrell, F. L. Homa, and J. C. Brown, J Mol Biol **392**, 885 (2009).

[209] P. Grayson, L. Han, T. Winther, and R. Phillips, Proceedings of the National Academy of Sciences **104**, 14652 (2007).

[210] A. Ortega-Esteban, K. Bodensiek, C. San Martín, M. Suomalainen, U. F. Greber, P. J. de Pablo, and I. A. T. Schaap, ACS Nano (2015), 10.1021/acsnano.5b03020.